AD NUMBER

AD281597

NEW LIMITATION CHANGE

TO

Approved for public release, distribution unlimited

FROM

No Foreign

AUTHORITY

DTRA ltr., 6 May 99

TECHNICAL PROGRESS REPORT

DEFENSE ATOMIC SUPPORT AGENCY
WASHINGTON 25, D. C.

Technical Report

2-30-61-1

RESEARCH STUDY OF THE PRODUCTION OF RETINAL BURNS FINAL REPORT

H. W. Rose
Project Leader

October 1961

Work Carried Out Under Contract DA-49-146-XZ-046

Section 5 Was Written by H. N. Ritland
and Section 6 by George Werth

LOCKHEED MISSILES & SPACE COMPANY
A Group Division of Lockheed Aircraft Corporation
Sunnyvale, California

FOREWORD

This work was performed by Space Physics, Lockheed Missiles and Space Company, under contract DA-49-146-XZ-046 of the Defense Atomic Support Agency.

ABSTRACT

The spectral transmission of the chorioidal and the pigment epithelium is determined in rabbit and human eyes. The threshold for chorioretinal lesions is determined with a laser. The attenuation of radiation in four model atmospheres is discussed. Formulae and computation methods are developed for the computation of the risk of chorioretinal lesions from atomic fireballs, depending on yield, atmosphere range, and absorption in eye tissues.

ACKNOWLEDGMENTS

The spectral transmission measurements reported in Section 2 were performed by Allan I. Carlson and Scott J. Larson.

T. A. Perls, A. Owyang, J. J. Hartog, P. J. Hart, and E. C. Y. Inn participated in the experiments reported in Section 3 and performed the total and spectral emission measurements of the sources.

CONTENTS

ILLUSTRATIONS

ILLUSTRATIONS (Cont.)

Section 1
INTRODUCTION

The experiments described in this report and the methods of computation presented in Section 5 are concerned with the risk of producing chorioretinal burns by means of atomic fireballs. The intelligent design of protective devices and the formulation of protection procedures require a knowledge of the threshold distances for this risk. Fireball yield, fireball altitude and observer altitude, atmospheric conditions, slant range, air transmission, pupillary size, and absorptive characteristics of the eye will determine these threshold distances.

For the computation of threshold distances, the temperature time history of the tissues can be used as a criterion. A check on these results can be obtained from a knowledge of the threshold doses to the retina if these threshold doses can be determined for very short-time pulses from well-collimated beams.

Section 2
SPECTRAL ABSORPTION

Spectral absorption measurements in the wavelength range of 3,400 to 19,300 Angstroms were performed with a double-beam Perkin-Elmer spectrophotometer and automatic recording. In one beam of the spectrophotometer, two microscopic cover glasses with wetted inside surfaces were inserted; in the other beam, tissue specimens were inserted between two identical microscopic cover glasses. For the earlier part of the spectrophotometric measurements of rabbit tissue, a 60-sq-mm cross section of the beam was utilized. During this phase of the work, the separate preparation of the pigment epithelium of retina was attempted in various ways. However, during the earlier work, no satisfactory preparations of the pigment epithelium were obtained. The spectrophotometric curves (of the chorioid only) were obtained for seven eyes in the early phase. Satisfactory preparations of the pigment epithelium were later obtained by removing pigment epithelium by means of brushing, controlled as to time and pressure by microscopic examination. For rabbit No. 6, eye No. 2, spectrophotometric measurements were obtained for the pigment epithelium and the chorioid through the large 60-sq-mm field. For rabbit No. 7, eye No. 1, spectrophotometric data were obtained in the retinal pigment epithelium only, through the large 60-sq-mm beam. This measurement was repeated on the same eye after drying for 24 and 48 hrs. The next four rabbit eyes yielded absorption data on pigment epithelium and chorioid through a 60-sq-mm beam. All measurements previously described were taken in each case on a single 60-sq-mm area of the tissue, with the long axis of the rectangle centered on the rabbit fundus in the nasal-temporal direction and located immediately below the optic nerve and the myelinated fibers.

All further measurements were performed by punching out, with a 5 by 10mm rectangular die, three areas of about 50 sq mm from the tissues while they

were still in contact with the sclera. The tissues were then separated and placed between microscopic cover glasses as in the previous technique. In mounting the cover glasses on a support, the pressure was adjusted in such a manner that the tissue specimen filled the same area as the 50-sq-mm die. In this way, the thickness of the tissue specimen between the cover glasses was identical to the thickness in the intact eye. The tissue-coverglass sandwich was mounted on a brass support which was inserted in the spectrophotometer. This brass support had a beam-limiting slit of 20 sq mm which was about 7.2 mm high and about 2.8 mm wide. An identical beam-limiting slit was interposed in the second beam which contained only the cover glasses and no tissue specimen. The tissues for this latter series of measurements were always taken from a temporal, a central, and a nasal area of the fundus. The long side of the rectangle was always vertical. In rabbits, the central specimen was placed centrally under the area of myelinated fibers; in humans, the central specimen included the area of the fovea centralis. The rabbit eyes were taken from animals pigmented either pure black, black and white, or wild colored. The rabbits were sacrificed immediately prior to preparation of the tissues.

The human eye tissues were obtained through the eye banks of the Palo Alto-Stanford University Medical Center, The University of California Medical School in San Francisco, and the Presbyterian Hospital of San Francisco. The human tissues were, as a rule, obtained by enucleation about 6 hrs after exitus. They were kept under refrigeration at about +2° to 4°C in a small vessel with an atmosphere humidified by saturated sponges. The cornea was in most cases preserved by one drop of neomycin. The tissues were measured 5 to 48 hrs after enucleation.

Figures 2-1 through 2-20 are curves giving spectrophotometric transmission of rabbit tissues. Each curve is identified by rabbit number and eye. Spectrophotometric data for both rabbit and human tissues are presented in tabular form in Appendix A. Tables A-1 through A-6 give this data for rabbit tissues and Tables A-7 through A-16, for human tissues. For rabbit tissues,

identification is given by animal number and eye, for human tissues, by running numbers, H-1, H-2, etc. for each eye.

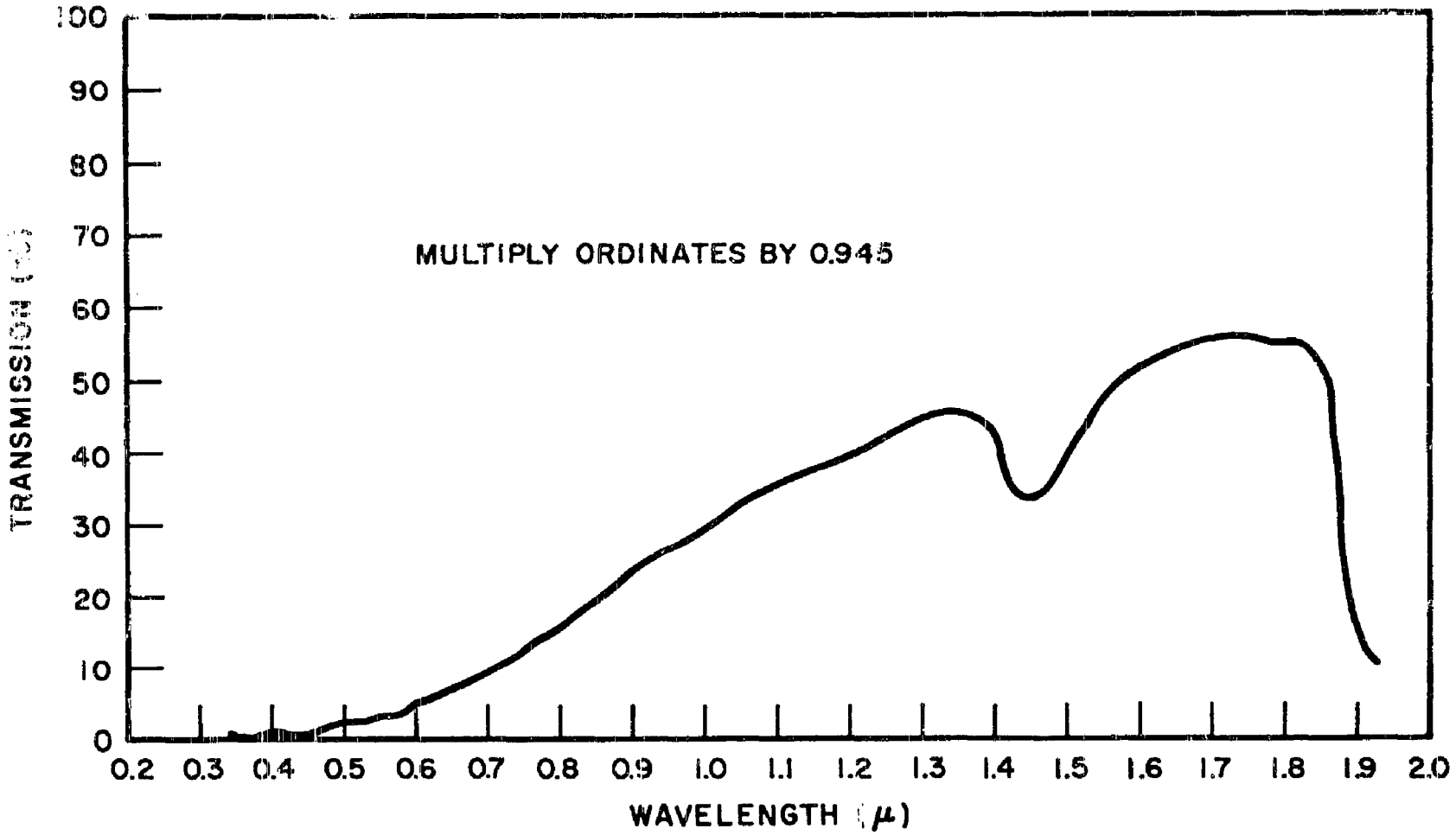

Fig. 2-1 Spectral Transmission of Chorioid: Rabbit 2, Eye 2

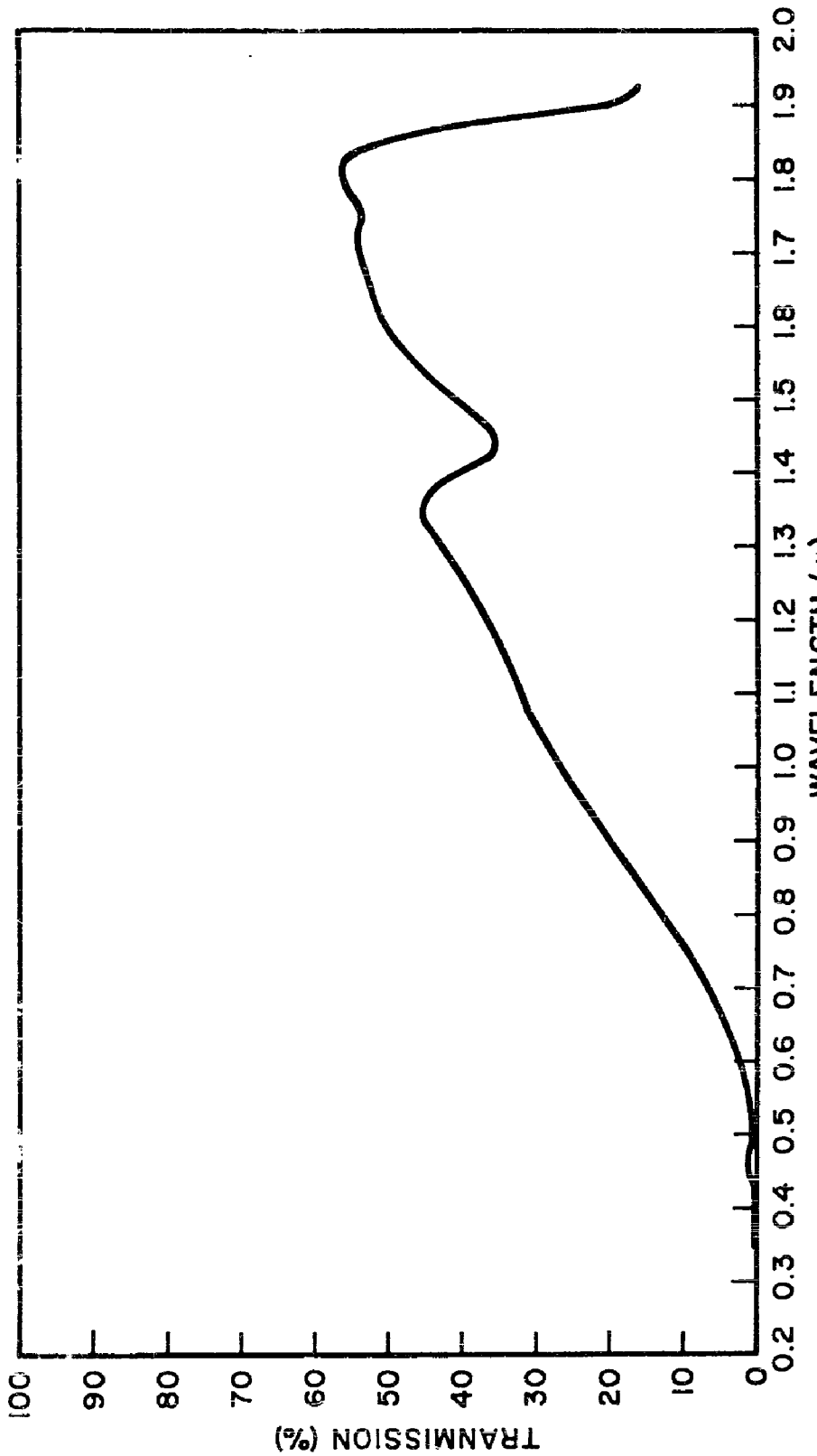

Fig. 2-2 Spectral Transmission of Chorioid: Rabbit 3, Eye 2

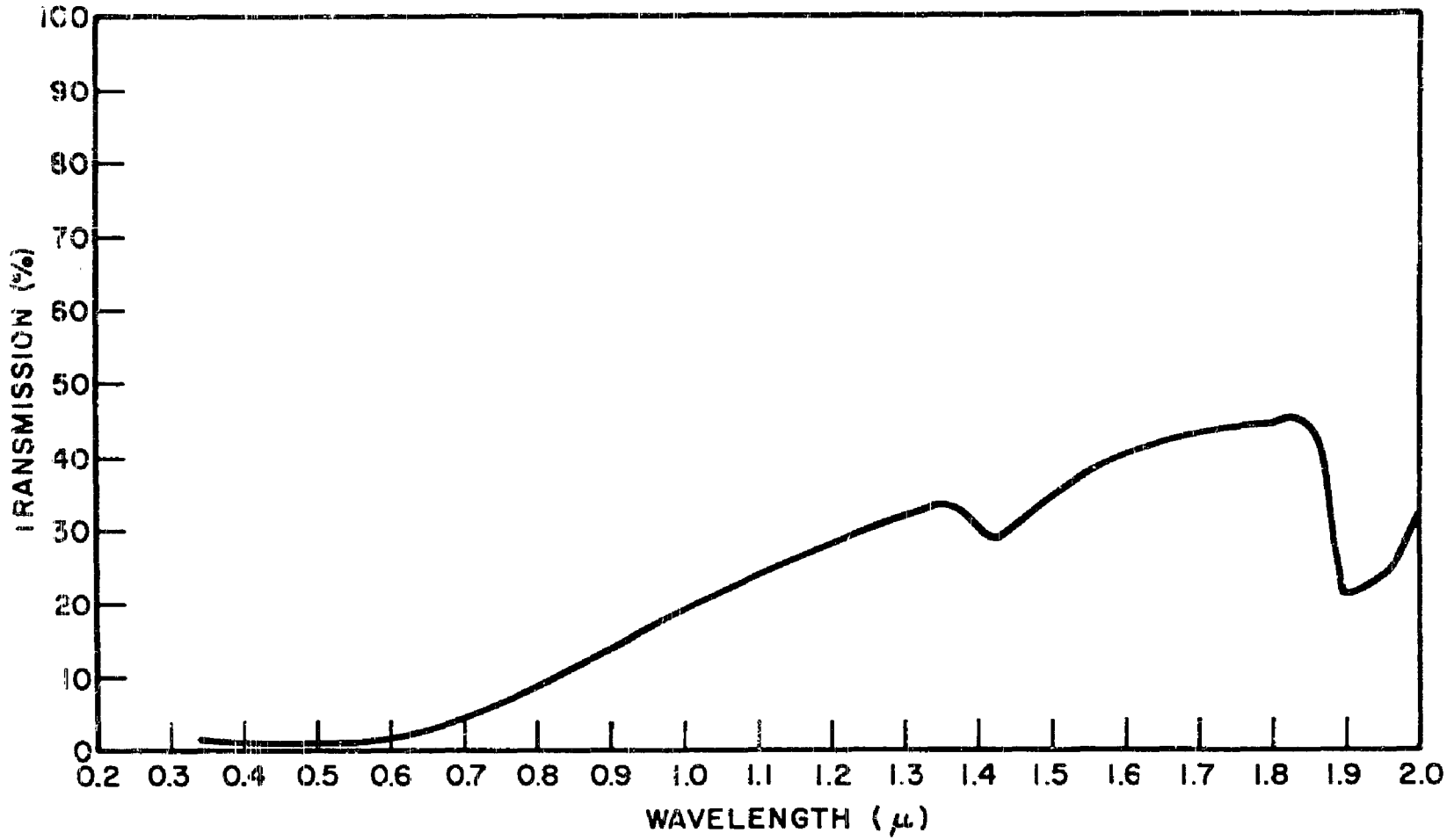

Fig. 2-3 Spectral Transmission of Chorioid: Rabbit 4, Black, Eye 1

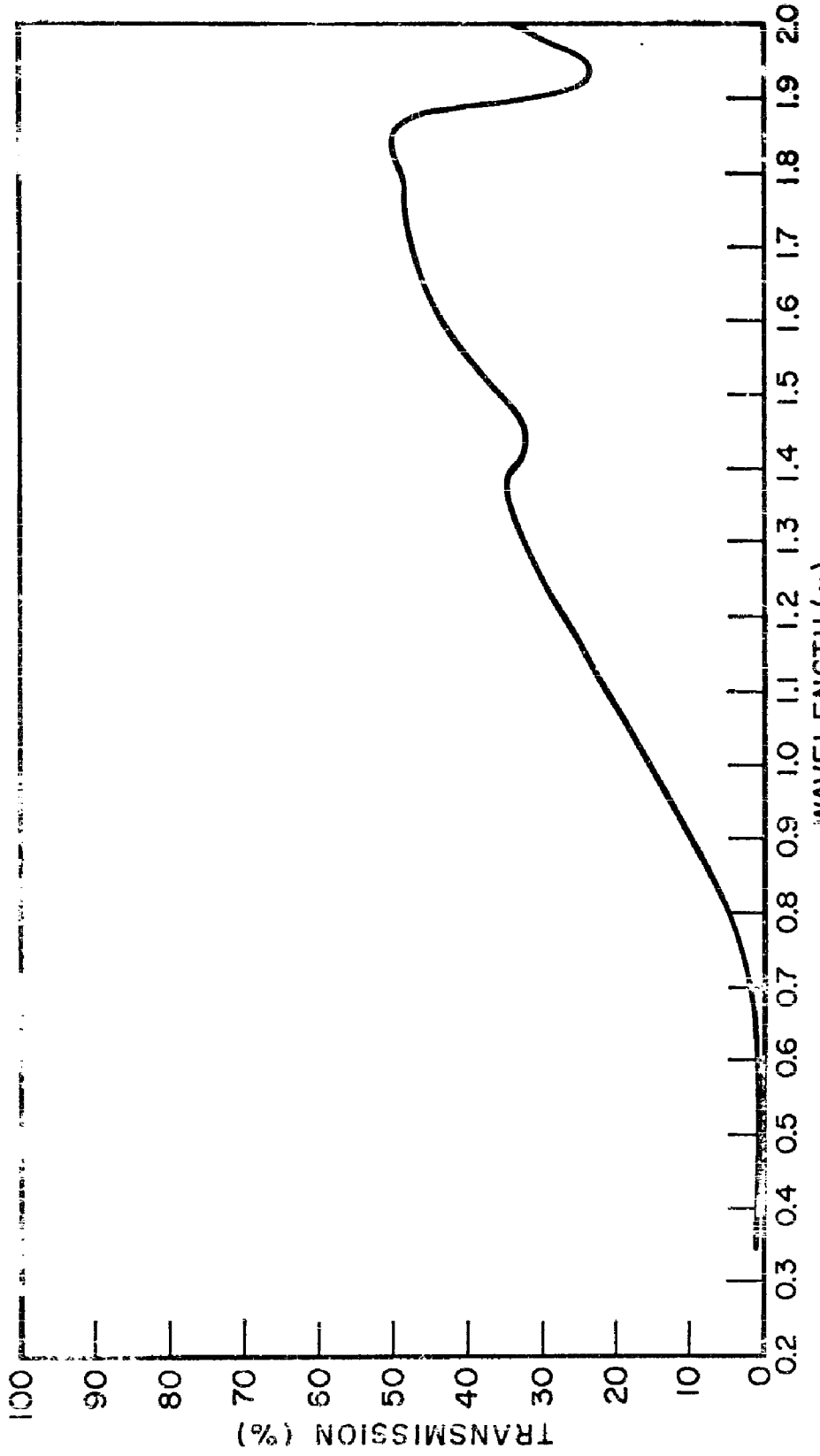

Fig. 2-4 Spectral Transmission of Choroid: Rabbit 4, Black, Eye 2

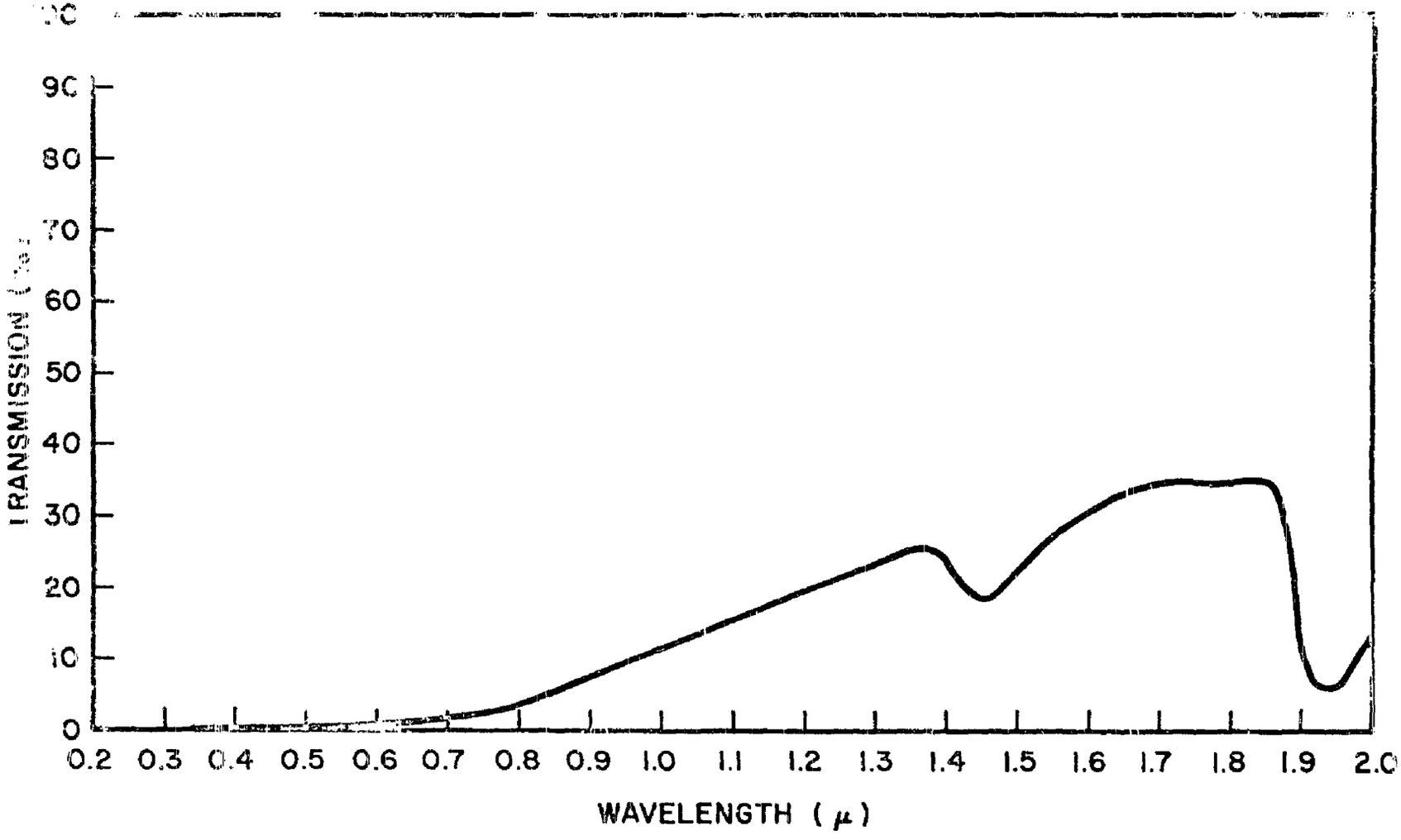

Fig. 2-5 Spectral Transmission of Chorioid: Rabbit 5, White With Black, Eye 1

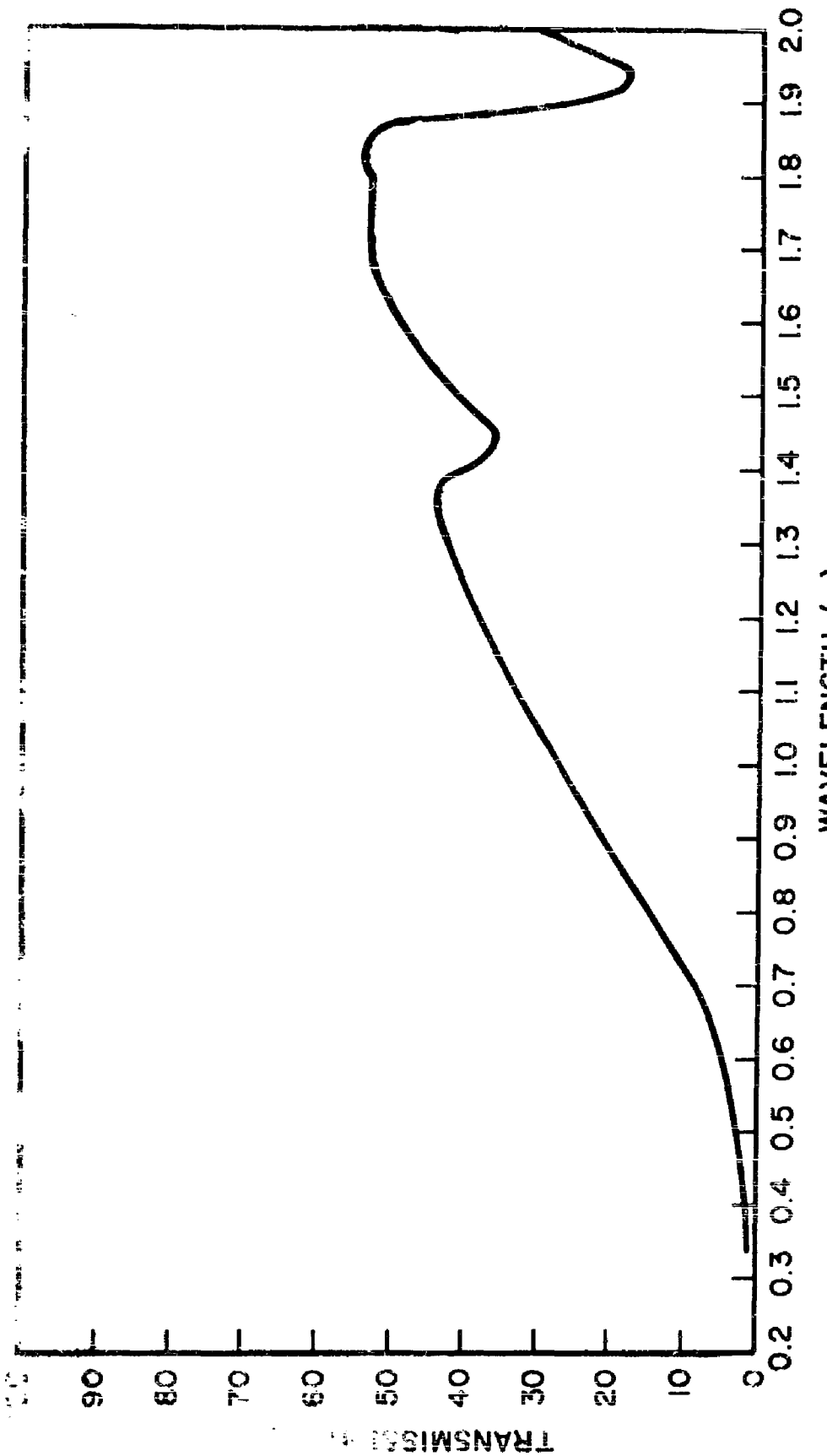

Fig 2-6 Spectral Transmission of Chorioid: Rabbit 5, White With Black, Eye 2

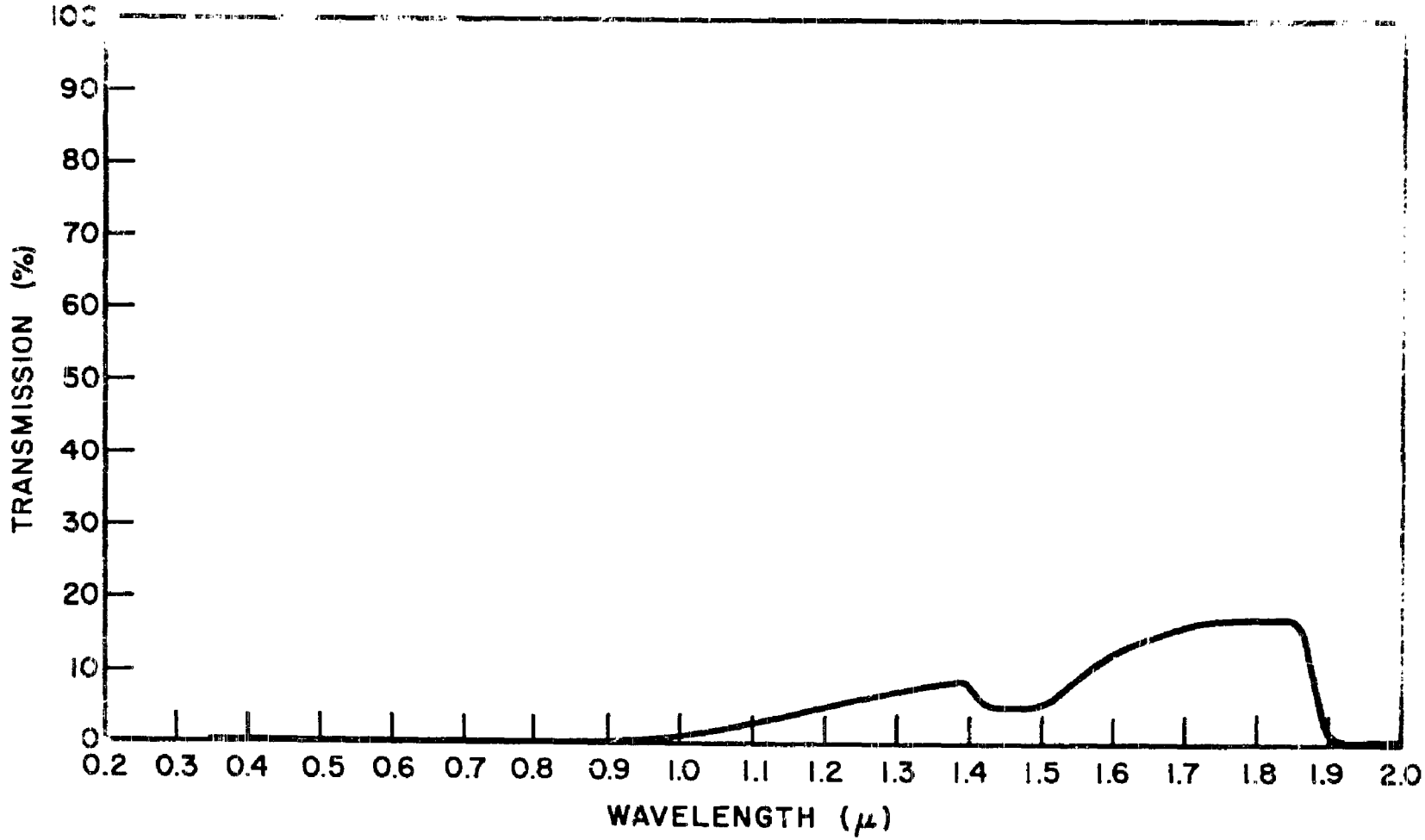

Fig. 2-7 Spectral Transmission of Chorioid: Rabbit 6, Wild Color, Eye 1

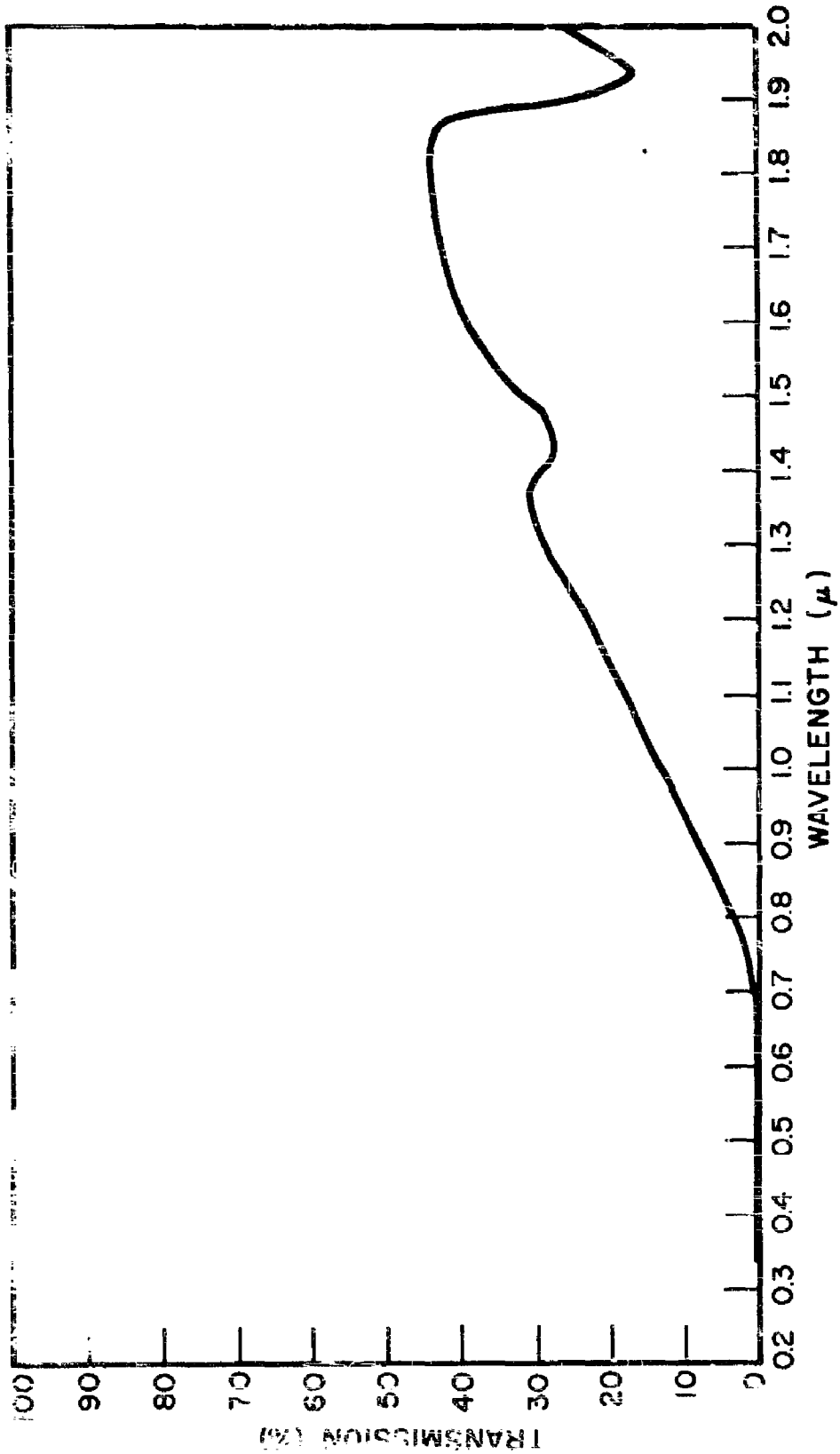

Fig. 2-8 Spectral Transmission of Choriold: Rabbit 6, Wild Color, Eye 2

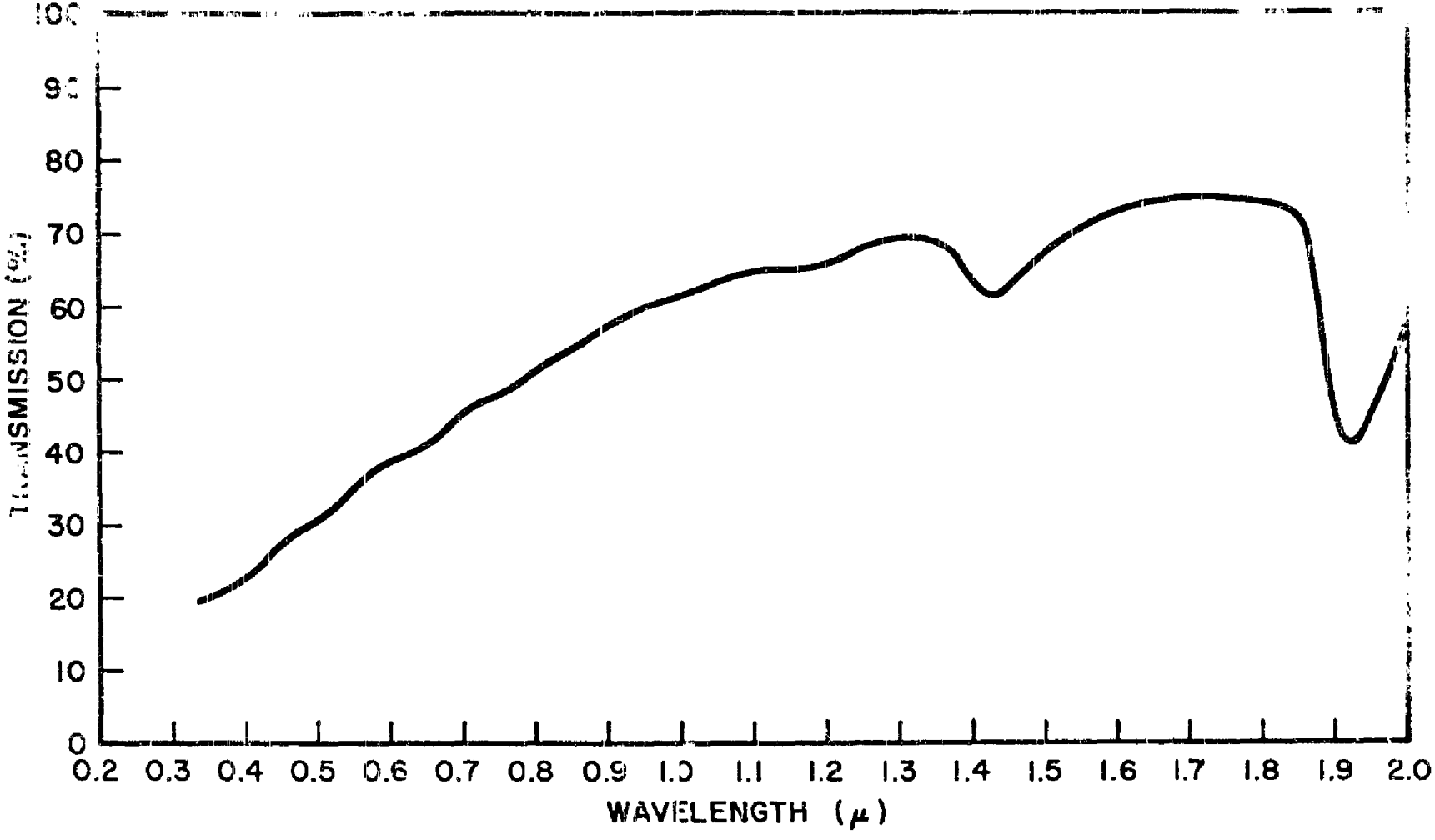

Fig. 2-9 Spectral Transmission of Retinal Pigment Epithelium: Rabbit 6, Wild Color, Eye 2

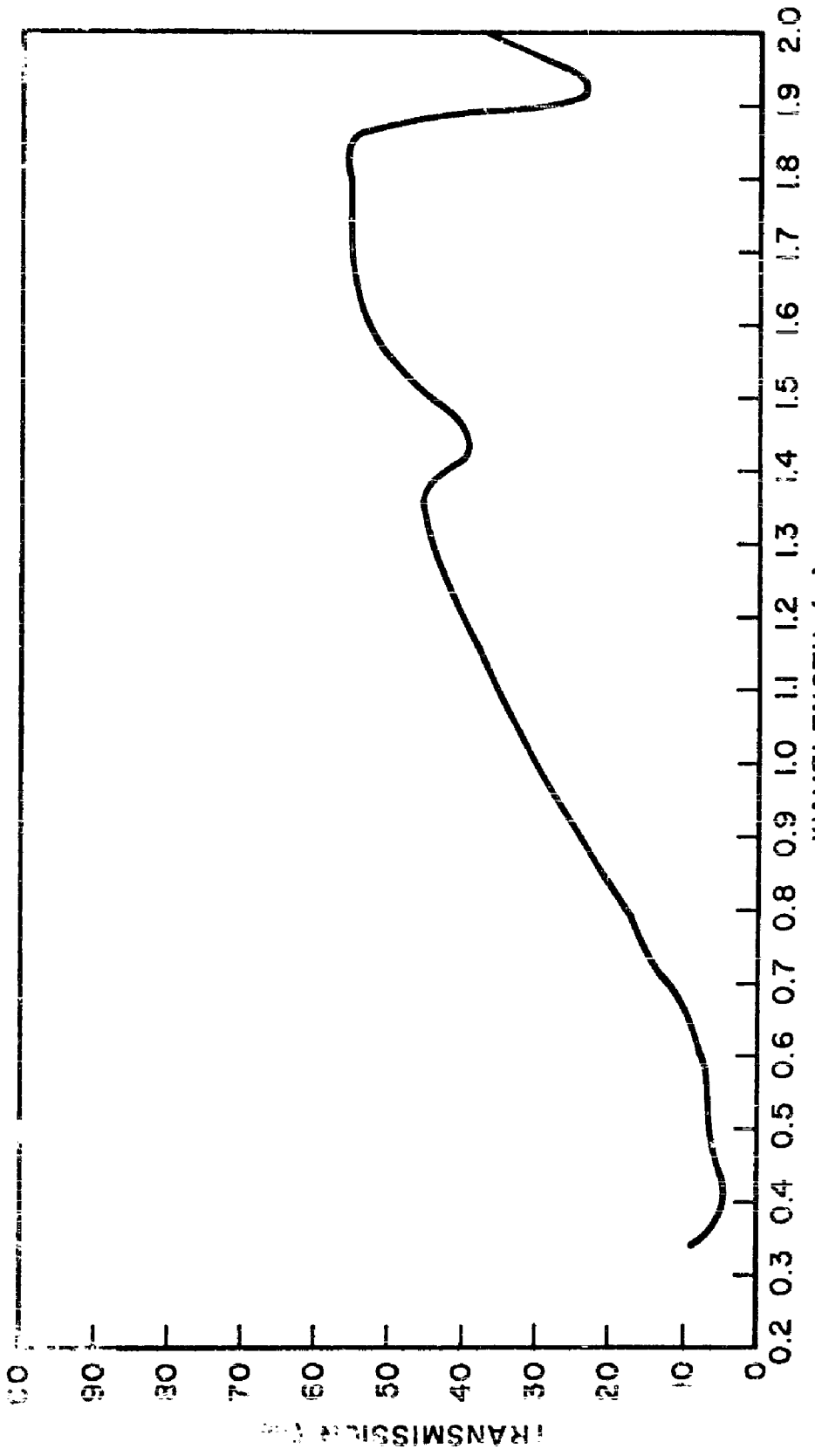

Fig. 2-10 Spectral Transmission of Retinal Pigment Epithelium: Rabbit 7, Eye 1

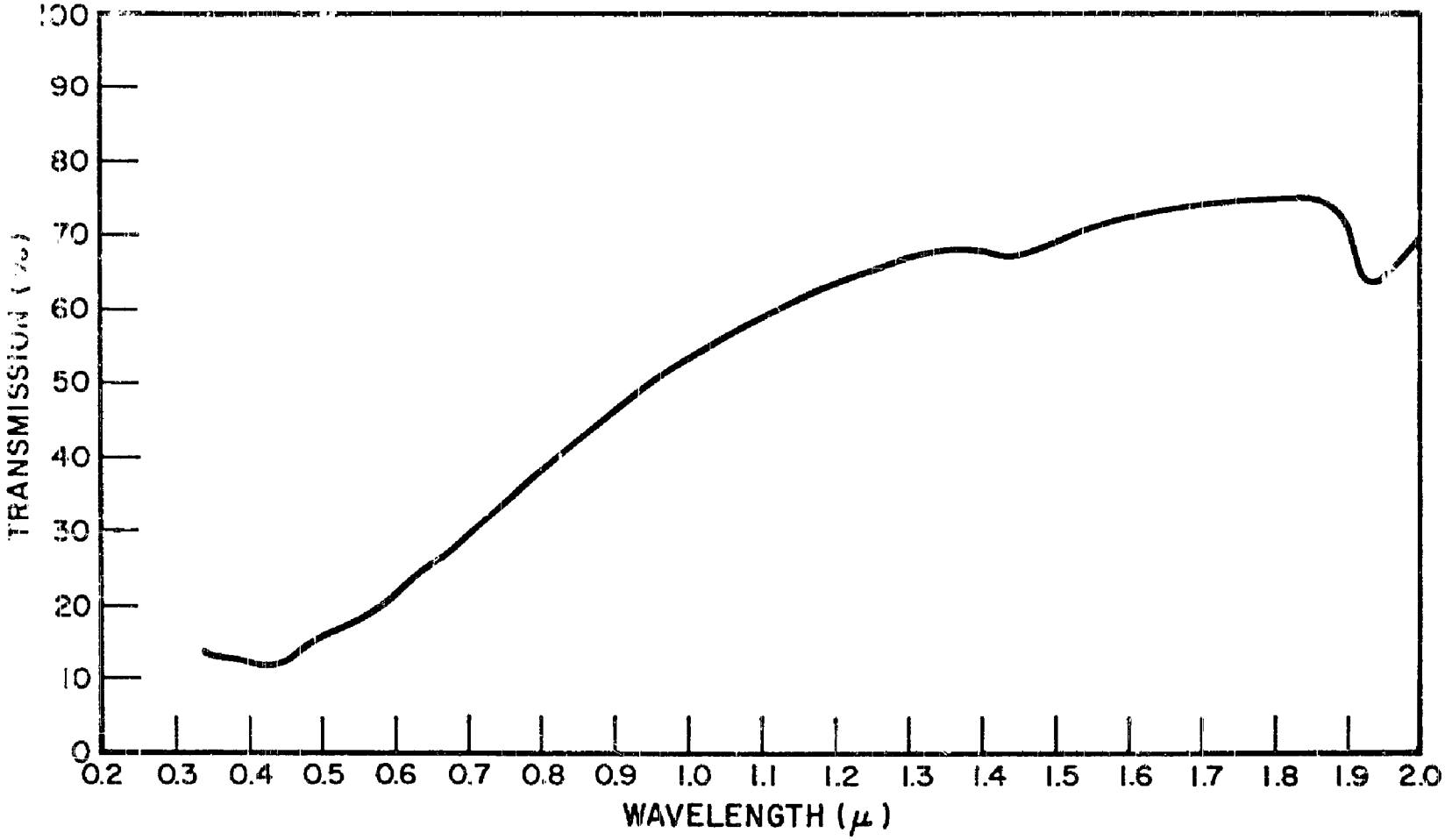

Fig. 2-11 Spectral Transmission of Retinal Pigment Epithelium: Rabbit 7, Eye 1, After 24 Hours

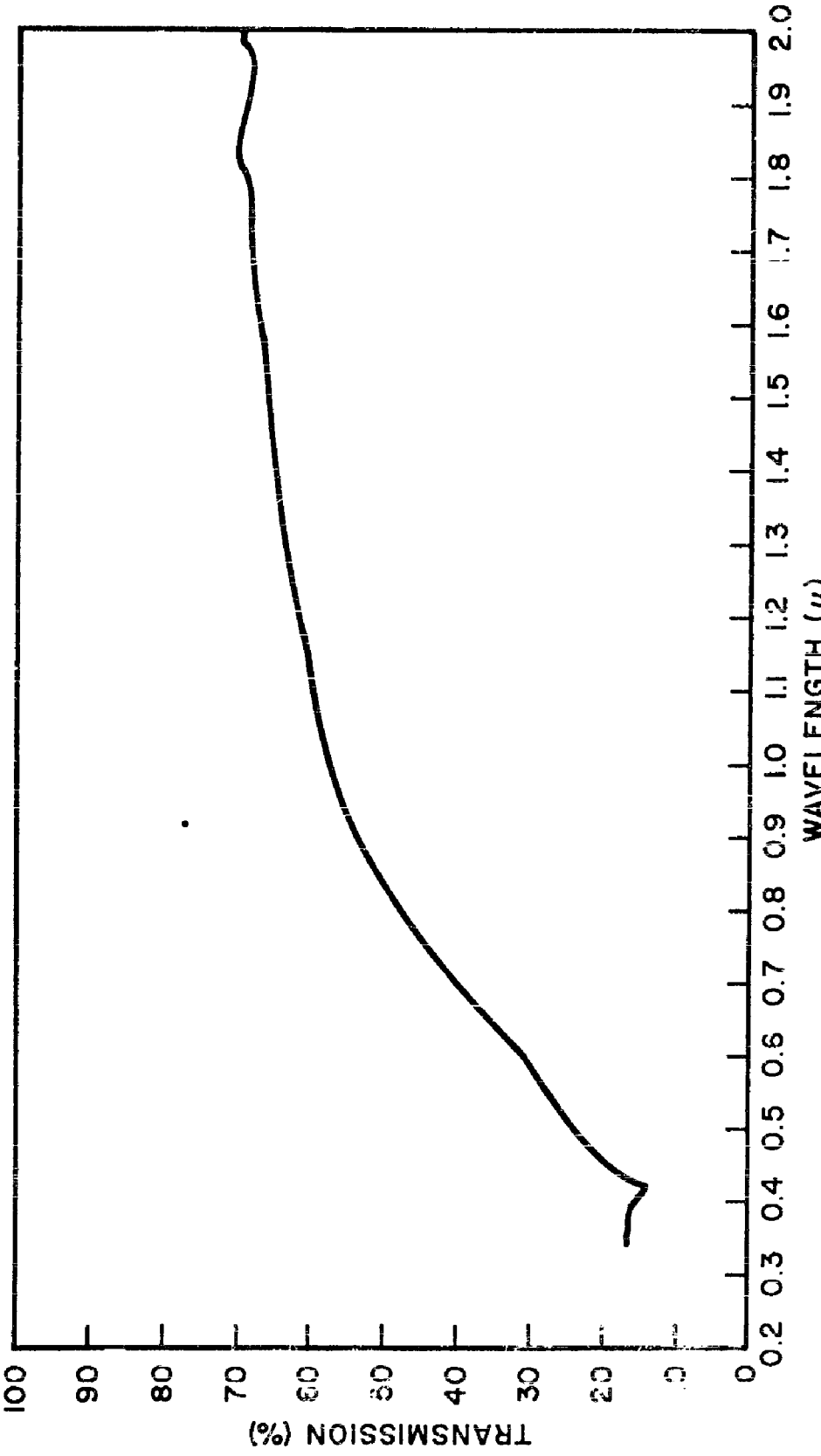

Fig. 2-12 Spectral Transmission of Retinal Pigment Epithelium: Rabbit 7, Eye 1, After 48 Hours

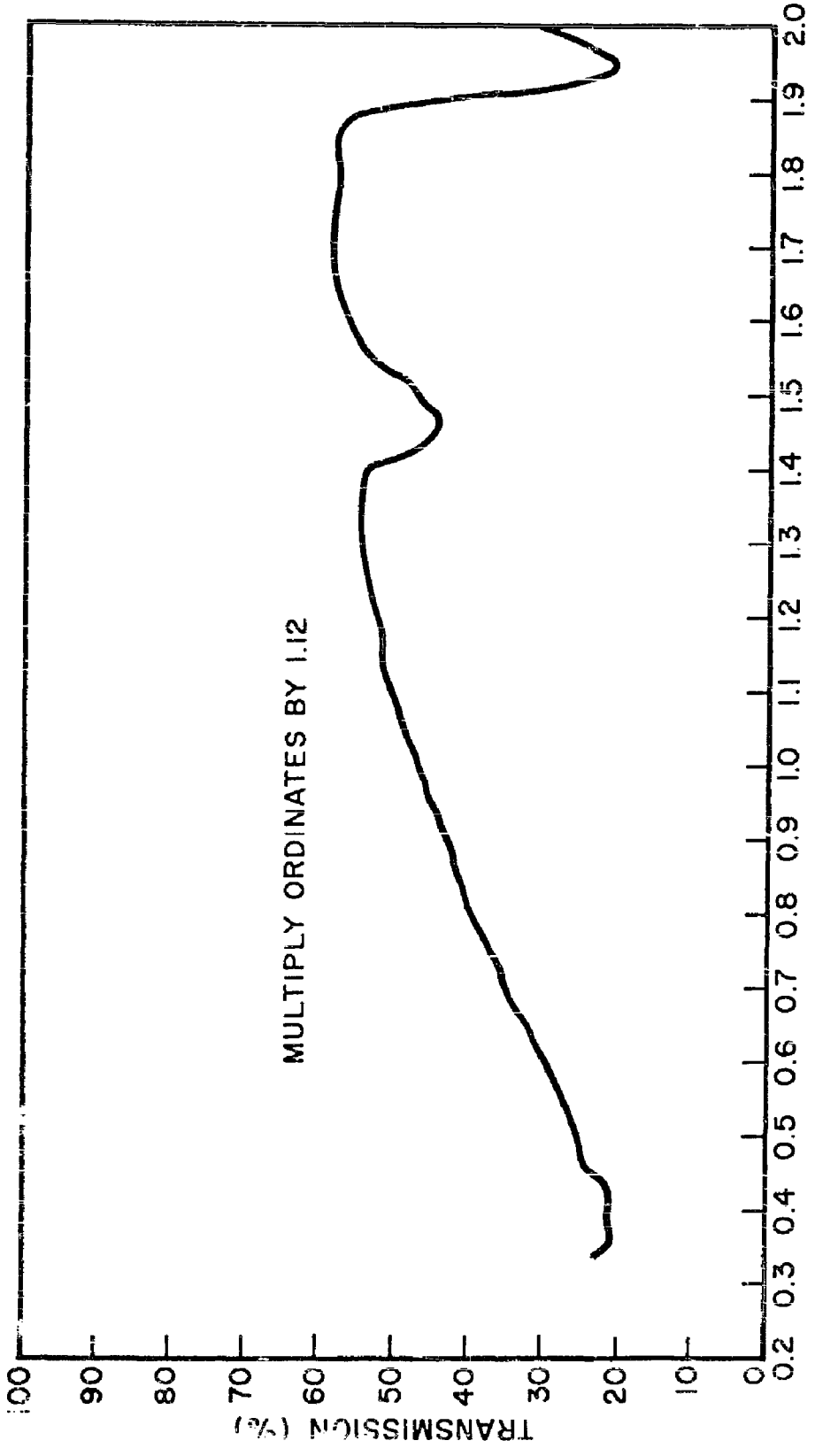

Fig. 2-13 Spectral Transmission of Retinal Pigment Epithelium: Rabbit 8, Right Eye

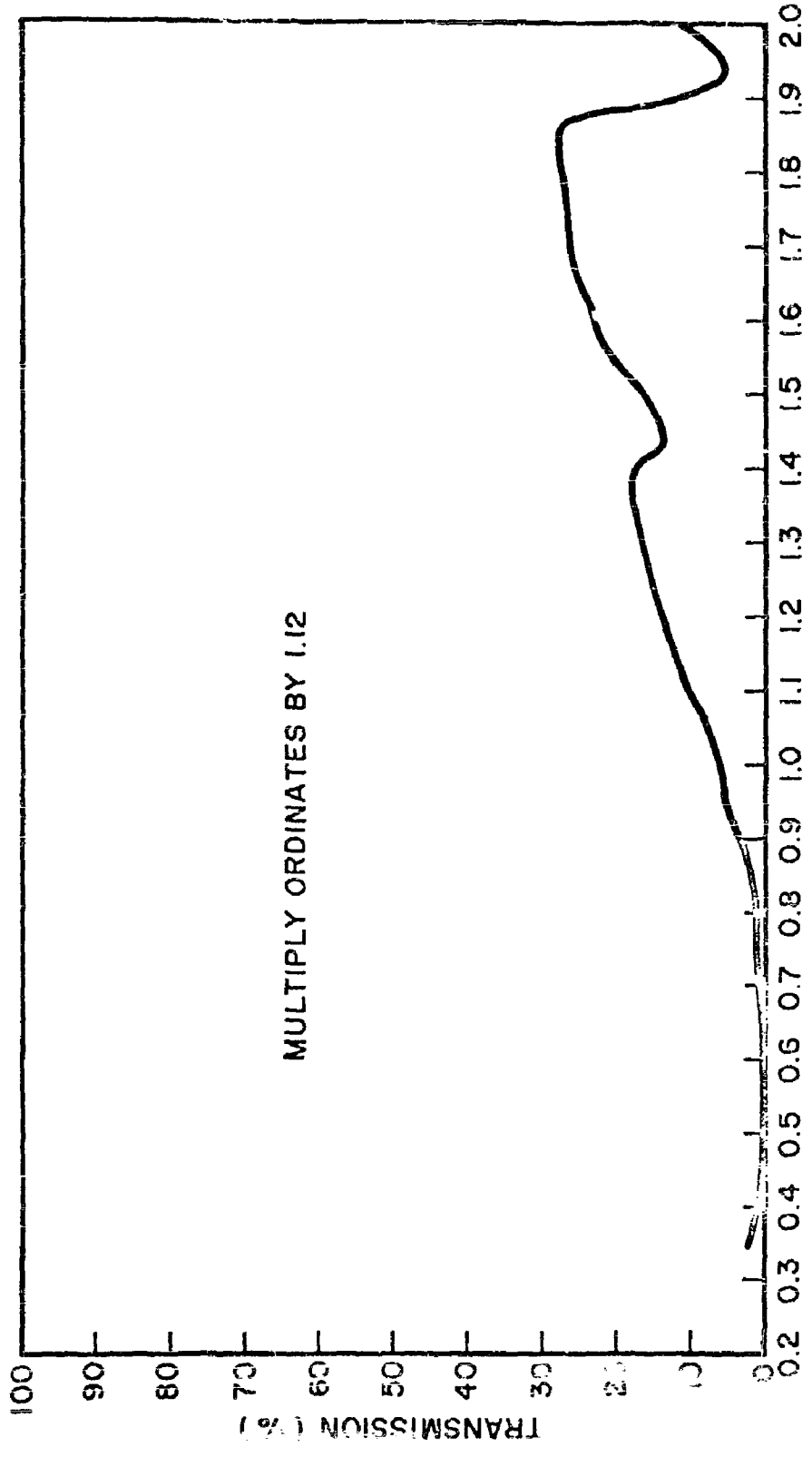

Fig. 2-14 Spectral Transmission of Corneal Rabbit 8, Eye Right Eye

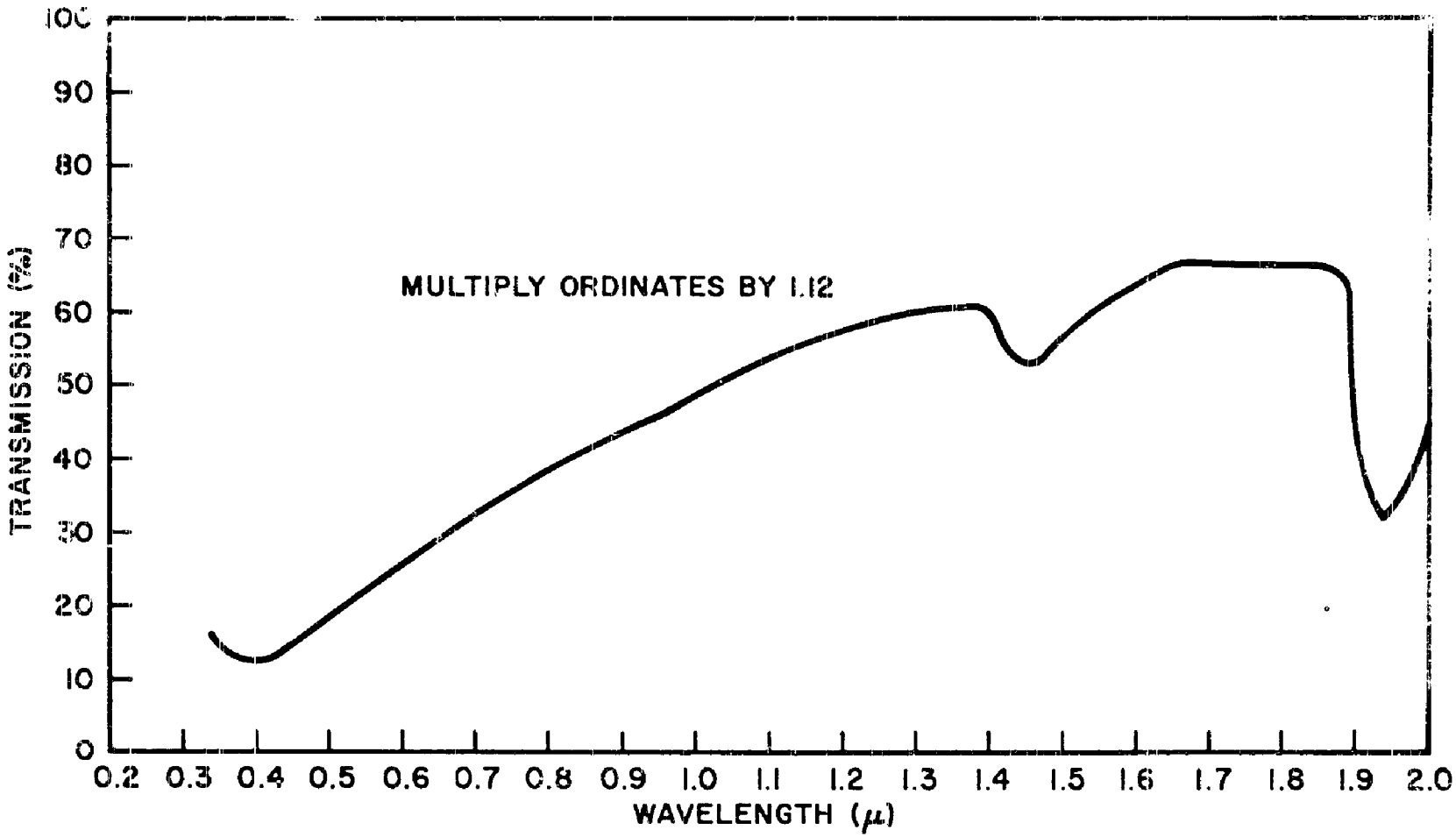

Fig. 2-15 Spectral Transmission of Retinal Pigment Epithelium: Rabbit 8, Black, Left Eye

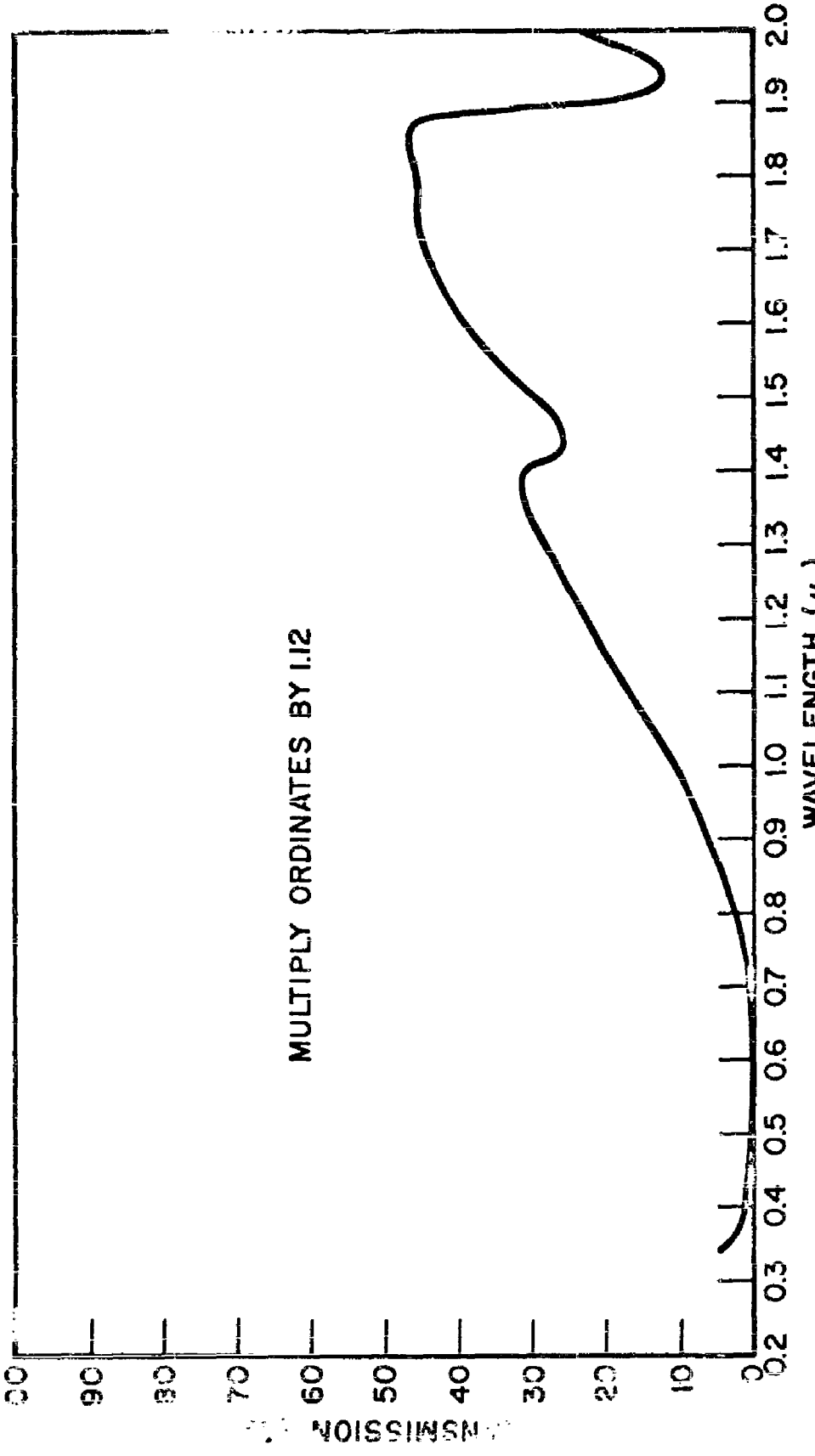

Fig. 2-16 Spectral Transmission of Choriold: Rabbit 8, Black, Left Eye

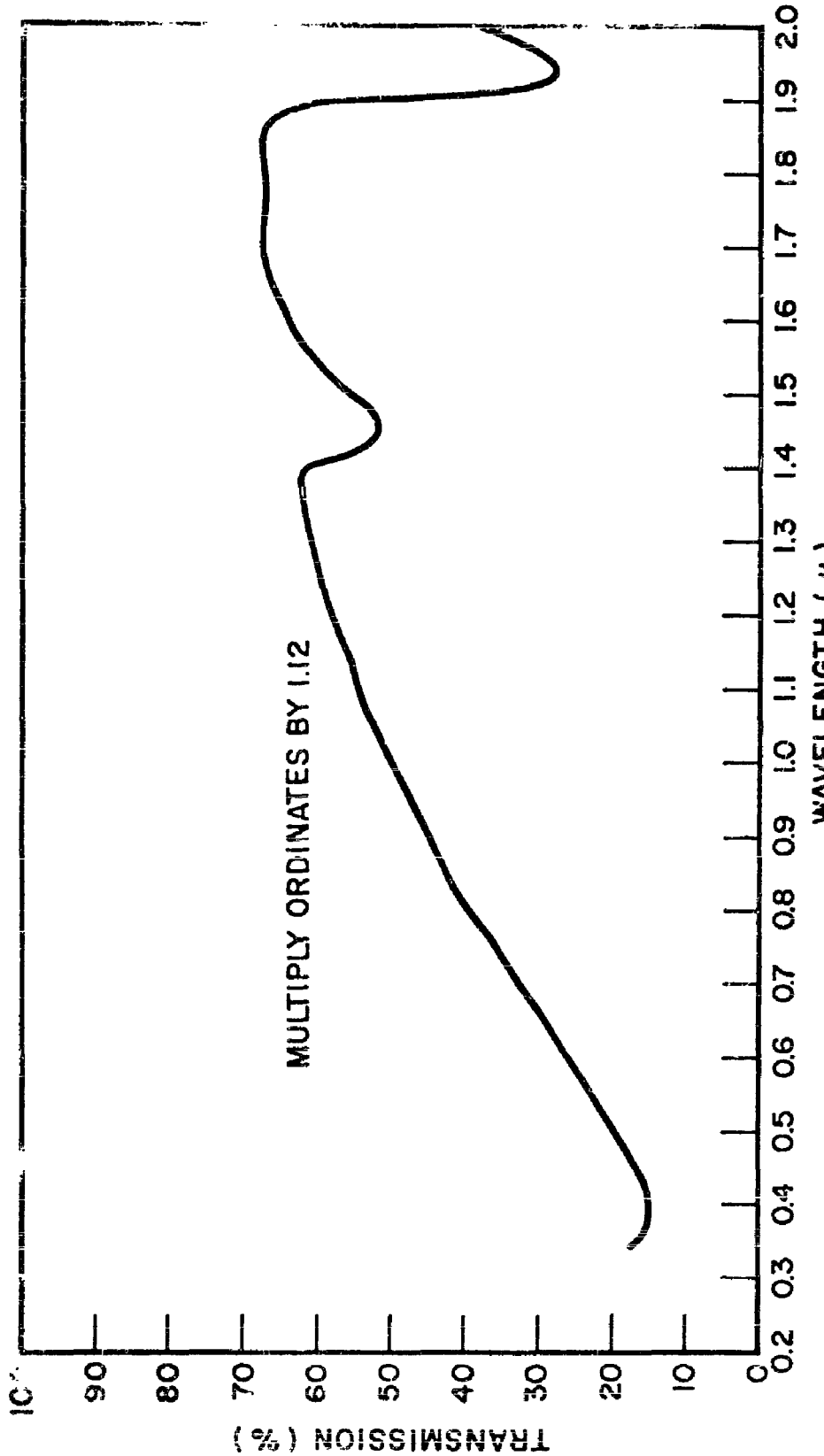

Fig. 2-17 Spectral Transmission of Retinal Pigment Epithelium: Rabbit 9, Wild Color, Right Eye

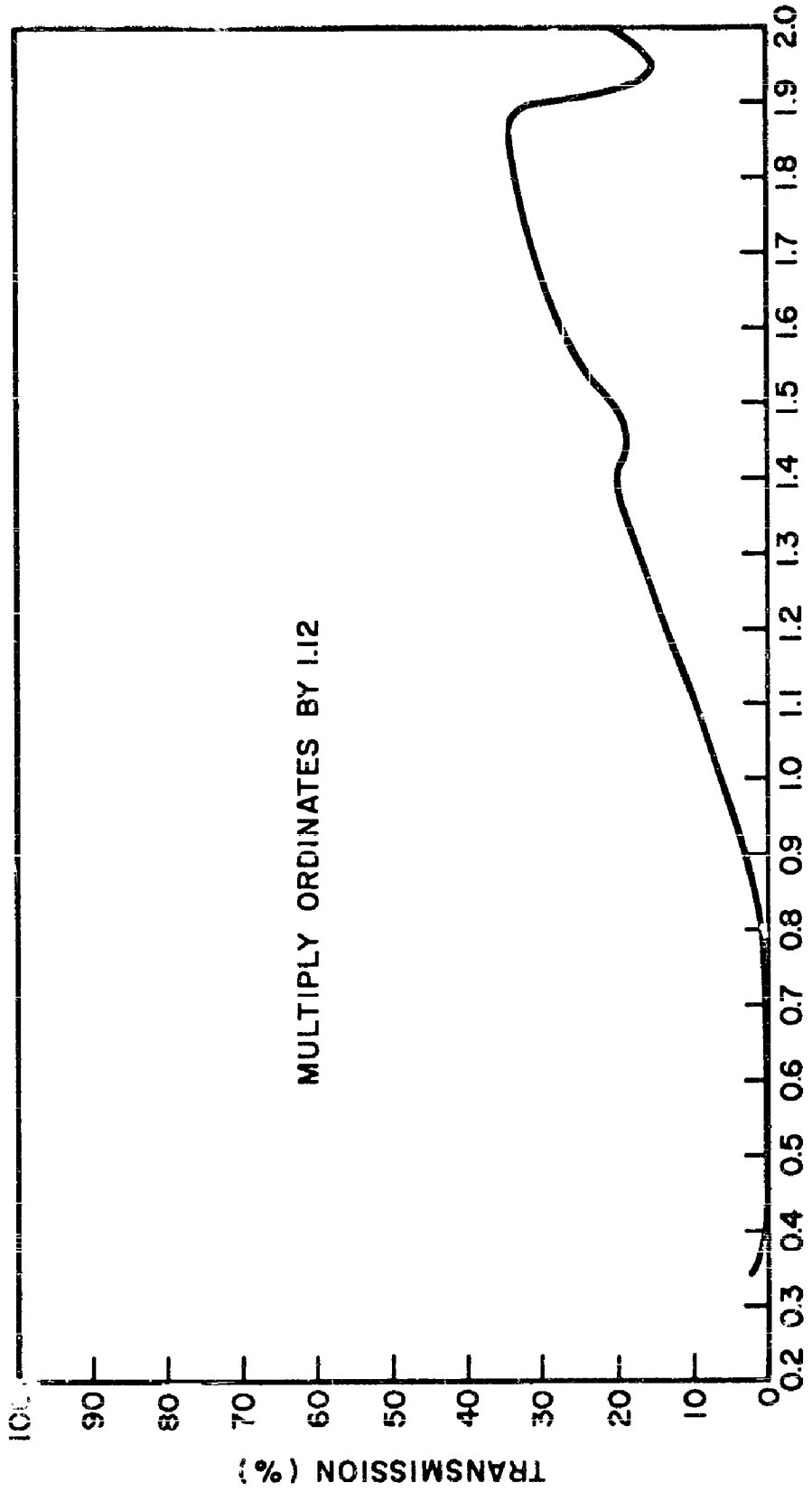

Fig. 2-18 Spectral Transmission of Chorioid: Rabbit 9, Wild Color, Right Eye

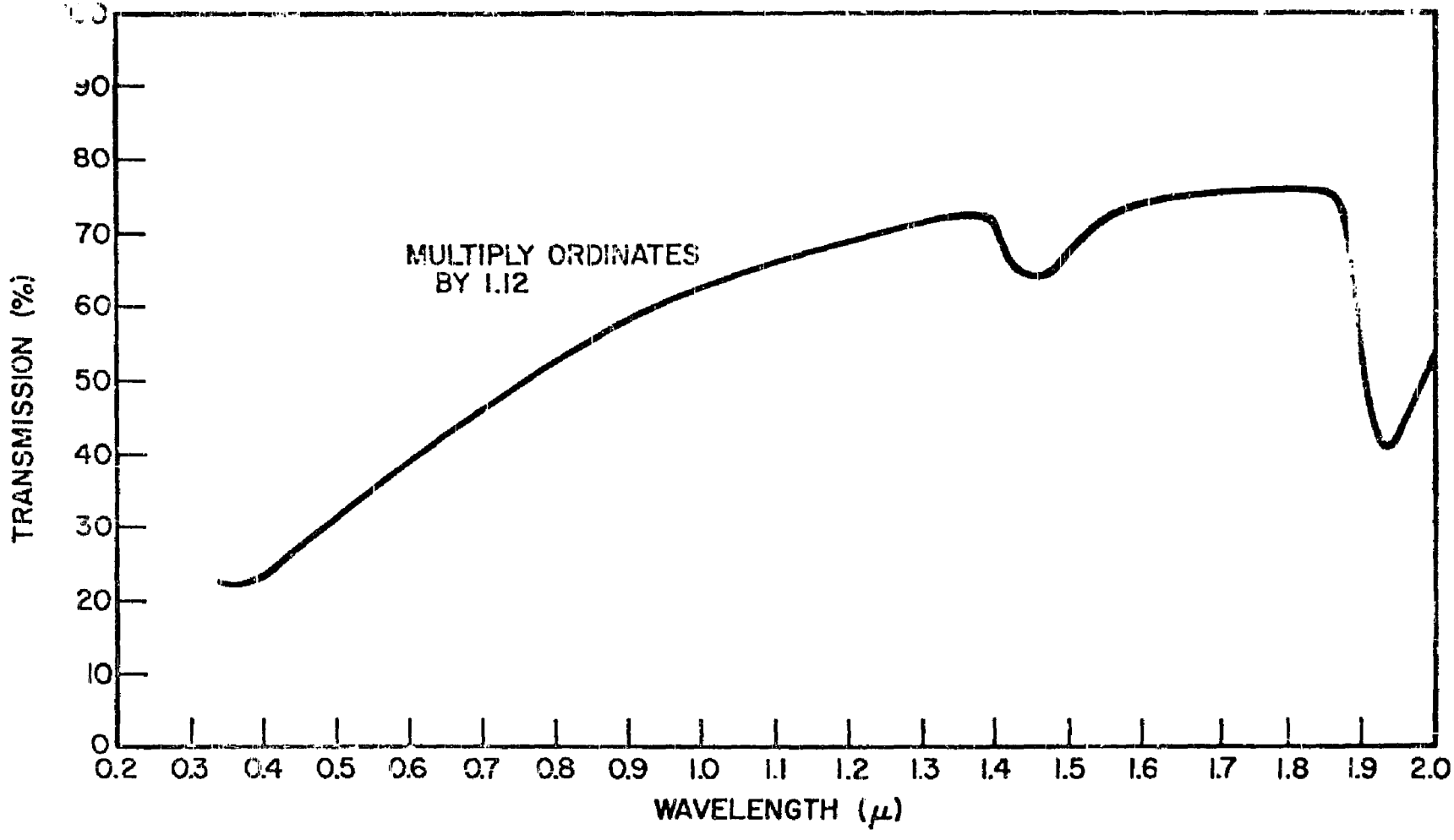

Fig. 2-19 Spectral Transmission of Retinal Pigment Epithelium: Rabbit 9, Wild Color, Left Eye

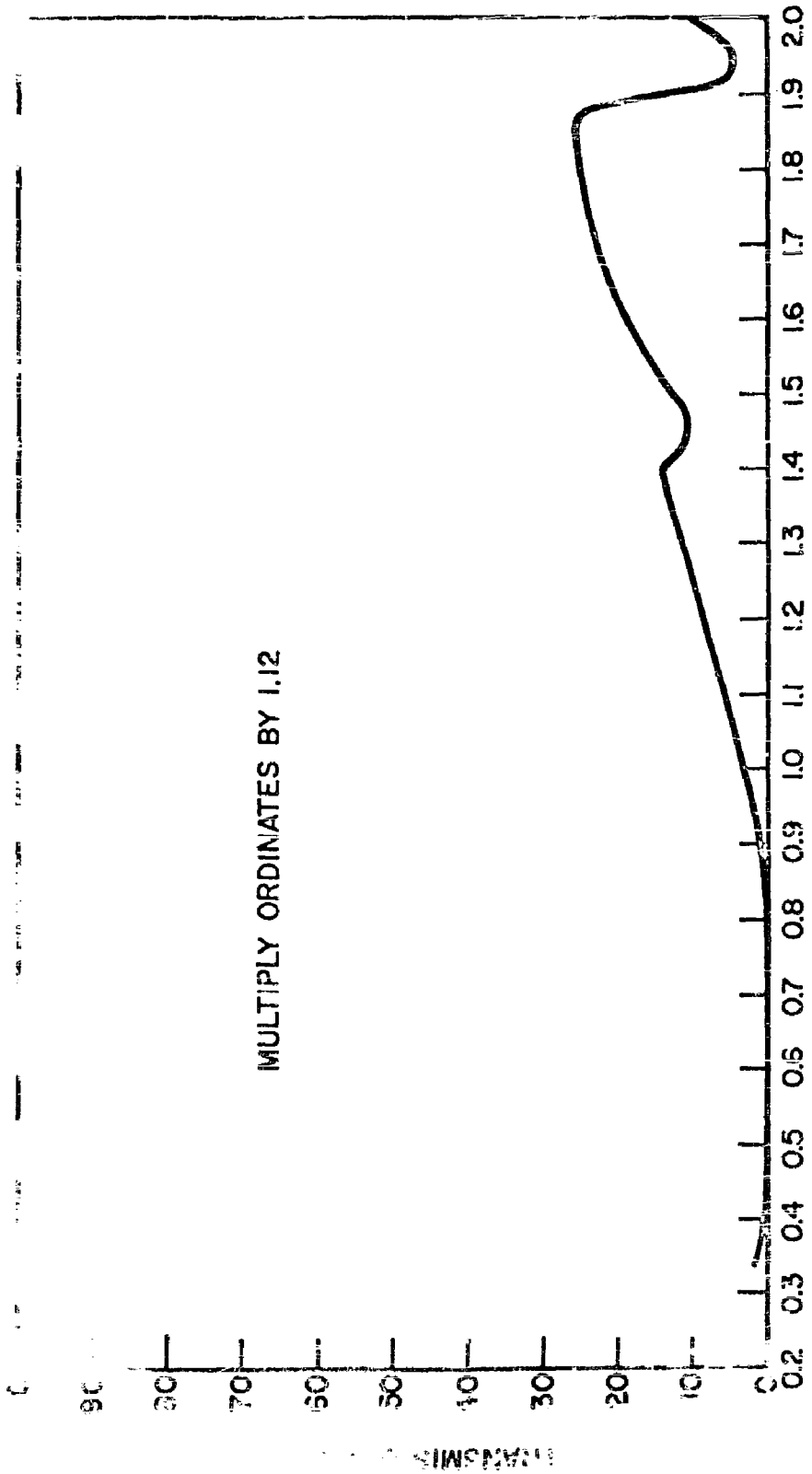

Fig. 2-20 Spectral Transmission of Choriold: Rabbit 9, Wild Color, Left Eye

Section 3
DETERMINATION OF DAMAGE THRESHOLDS

Various high-intensity sources were investigated, the aim being to simulate the first peak of atomic fireballs. Shock tubes, condenser discharge through air at atmospheric pressure, condenser discharge through vacuum, condenser discharge through water, and a laser (optical maser) were tried.

Radiation output from four arcs was measured with a photomultiplier system having response faster than 1 μsec. The total radiated energy in the spectral range above approximately 2000 A was obtained from an NRDL copper-disk calorimeter from which the thermocouple voltage was measured on a Hewlett-Packard 425 H microvolt meter. The time resolved measurements of the heat radiation over the same spectral range were made with a pyroelectric transducer having a side face exposed to radiation so that no heat would be lost and no time delay introduced by passing the heat through the usual electroded surface. The transducer had an electric rise time of 1 μsec. Emissivity for the bare pyroelectric material (Clevite PZT-4) was obtained.

Irradiations of the pyroelectric transducer and the copper disk calorimeter were determined at distances of 8 cm through 300 cm to establish inverse square relationships. Spectrophotometric data were obtained with a Hilger quartz prism spectrograph.

Data on luminescent areas, radiant emissivity and spectral distribution on all of these devices, except the laser, were not encouraging. The highest color temperature of the continuum in the air spark was estimated at 20,000°K. However, in the visible region, most of the emission was in several strong lines in the vicinity of 6,620 A. The maximum emission was reached in 3 μsec with an exponential decrease with a time constant of approximately 15 μsec, then the flux on the retina was not sufficient for the production of burns.

In a number of the condenser discharges, exposure of rabbit eyes showed at best a temporary edema with no permanent lesions being produced. It would, of course, be relatively easy to produce the lesions with a flash that is more extended in time. However, during flashes that are extended in time, heat will be conducted away from the retinal image of the light source during the exposure in appreciable amounts and, thus, only light sources of very short duration will permit good determination of threshold doses.

For the experiments with the laser, a Trion optical laser head, Model 3000, with a Trion-made power supply and trigger system was used (Figs. 3-1 and 3-2). The laser head, which contains a pink ruby of about 6 mm in diameter and about 80 mm in length, silvered at one end, and a spiral xenon tube, is visible in the center of Fig. 3-1. To the right is a container of liquid nitrogen for cooling the ruby rod. Examination of Fig. 3-3 shows that the laser beam first passes through a partially silvered mirror placed at a 45-deg angle. Here, about 1/3 of the energy is diverted 90 deg into a NRDL calorimeter. About 2/3 of the laser beam is transmitted straight through the mirror and, as shown in Fig. 3-1, during calibration is intercepted by a second identical calorimeter. However, since the exact division to be refracted and transmitted depends slightly on the angle of incidence, calibrations of the beam slant were run at least daily or after each rearrangement of components. As shown in Fig. 3-2, during the irradiation of the rabbit, the rabbit's eye was substituted for the second calorimeter. During the irradiation of the rabbit eyes, the location of the laser beam was observed through a Carl Zeiss-Henker combined refractometer ophthalmoscope. The ophthalmoscope was kept in a fixed position relative to the laser beam and the choice of location for the irradiation on the retina was made by moving the rabbit relative to the ophthalmoscope beam. The ophthalmoscope viewed the rabbit's retinal image at 90 deg to the laser beam on the down-beam side of the 45-deg mirror. Consequently, the irradiation from the laser entering the observer's eye was minimized and observation was possible during the irradiation by the laser. The irradiation diverted by the mirror to the calorimeter arranged at 90 deg to the laser beam was measured during each individual irradiation of the rabbit eye.

Fig. 3-1 Laser Experimental Assembly: A, Laser Head; B, 45-deg Mirror; C and D, NRDL Calorimeters; E, Opthalmoscope Refractometer; F, Liquid Nitrogen Container for Cooling Laser

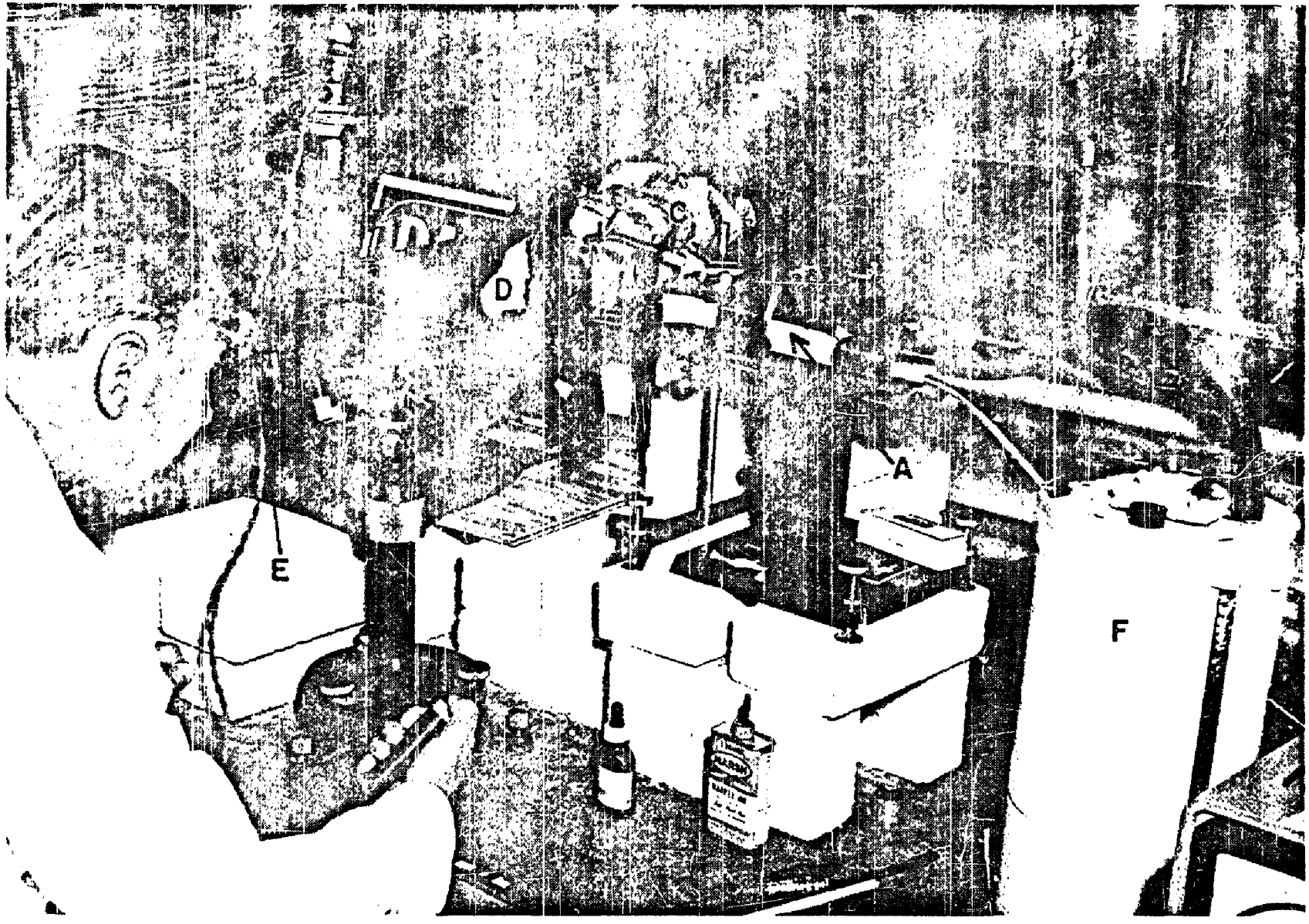

Fig. 3-2 Laser Experimental Assembly Showing Rabbit in Place of Calorimeter D

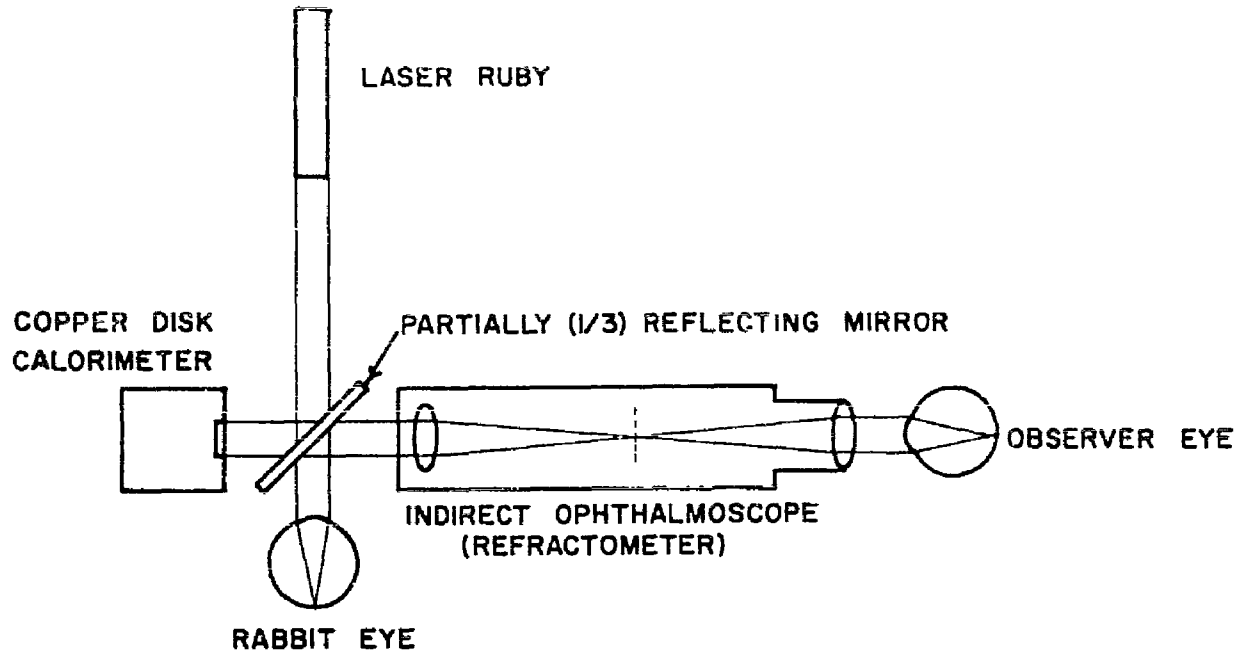

Fig. 3-3 Laser Burn Experimental Apparatus Viewed From Above

The pupils of the rabbits' eyes utilized for this purpose were dilated with homatropine (1 percent) given three times at 10-min intervals. In several cases, the dilatation effect from homatropine was initially sufficient but could not keep the pupil dilated after several irradiations with the laser. In this case, an ointment combining 2 percent homatropine, 2 percent cocaine, 1 percent adrenalin was used for dilatation. The rabbits were preselected for emmetropia after dilatation and all eyes reported subsequently in this section were within ±1.5 diopter from emmetropia. This selection was highly desirable in order to provide the full utlization of the well-collimated beam of the laser and thus permit the formation of the smallest possible image. While without additional shutters, the laser with a pulse length of 200 –400μ sec (Fig. 3-4) does not guarantee the production of burns in the shortest possible time, it has the advantage of the nearly perfect plane wave front and nearly monochromatic light.

The results of the laser irradiation of rabbit retinae are shown in Fig. 3-5. To avoid cluttering the illustration, early experiments with higher doses far

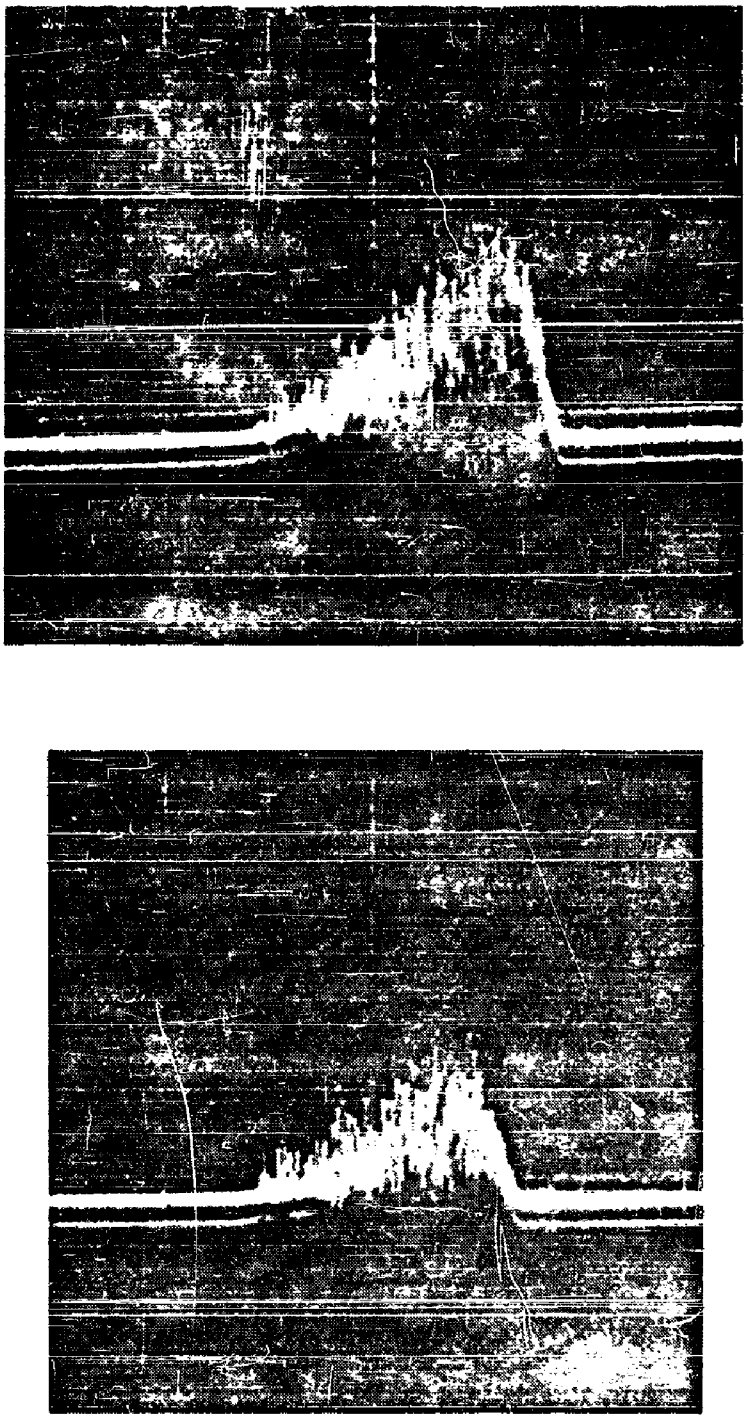

Fig. 3-4 Two Laser Pulses. Large divisions of the abscissa scale are 400 μsec. Pulses are [illegible] with pyroelectric [illegible] described in the [illegible]

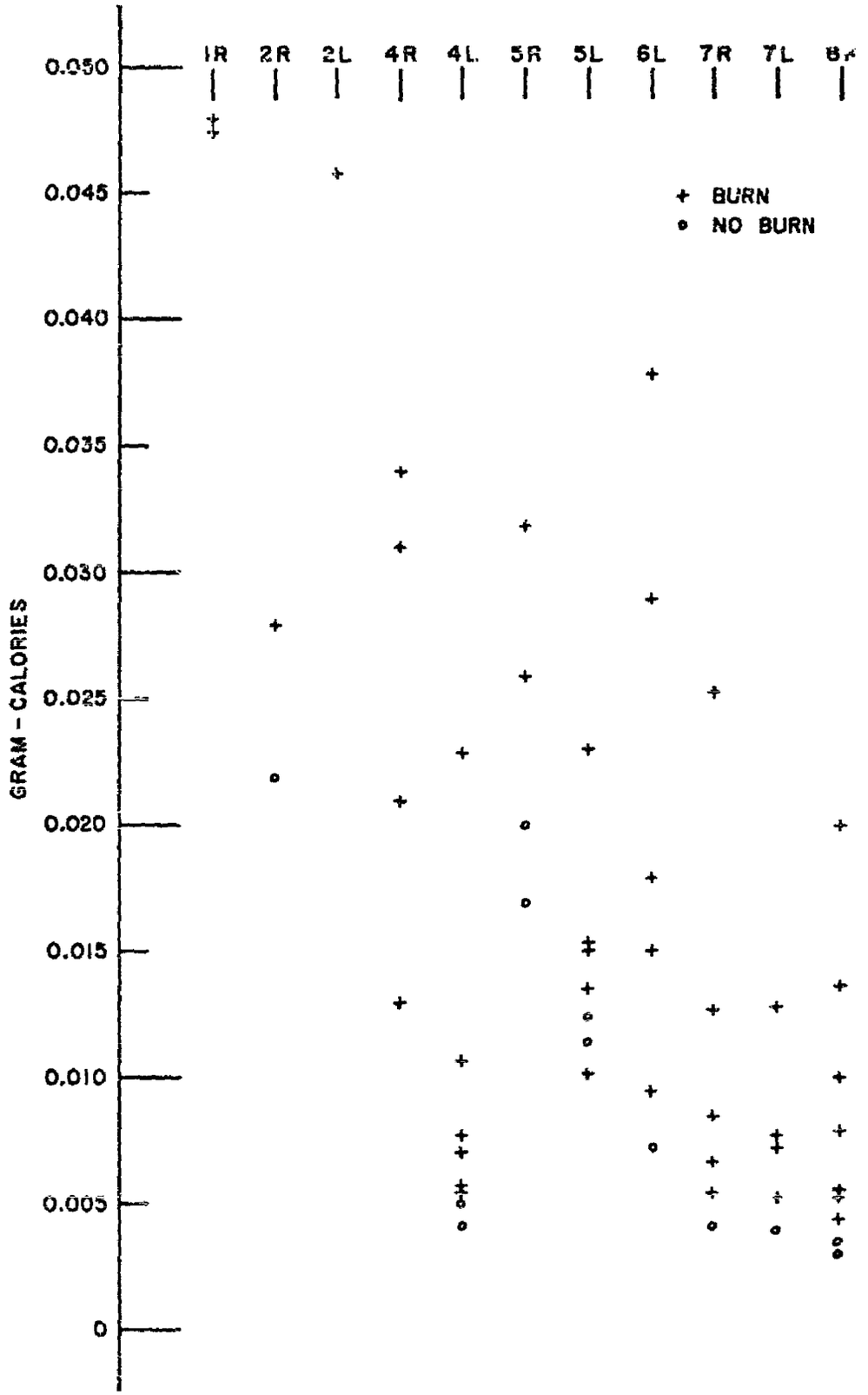

Fig. 3-5 Irradiation to the Cornea for Eleven Rabbit Eyes. Radiation is produced with a ruby laser and pupils dialated to 9mm or more

above threshold were omitted. The ordinate gives the irradiation at the rabbit cornea in gram calories. On each vertical line, all results on one retina are given. There is considerable spread in thresholds of irradiation. This is due to the individual variation in pigmentation. Lightly pigmented eyes like those of rabbit No. 2 gave a threshold dose for a chorioretinal burn of 0.025 g cal incident on the cornea. A medium pigmented eye, e.g., No. 5, gave a threshold dose at the cornea of 0.015 g cal and in the darkly pigmented eyes of rabbits 4, 6, 7 and 8, the thresholds were 0.005 g cal incident on the cornea.

The assumption is made that the clear media of the rabbit eye transmit 93 percent of radiation of wavelength 7000 A. Furthermore, the assumption is made that the effective retinal image in the laser experiments was 0.5 mm in diameter. This is in agreement with the results of the histological examination of lesions. Then, the threshold dose at the cornea of the lightly pigmented rabbit eyes, 0.025 g cal in a 6-mm diameter beam corresponds to a retinal threshold dose of 12.8 g cal x cm^{-2}. The threshold dose at the cornea of the medium pigmented rabbit eyes, 0.015 g cal in a 6-mm beam would correspond to 7.7 g cal x cm^{-2} at the retina. The threshold dose at the cornea of the darkly pigmented rabbit eyes, 0.005 g cal in a 6-mm beam, would correspond to 2.5 g cal x cm^{-2} at the retina. These threshold doses, with 7000 A radiation are higher than thresholds with sunlight because the eye pigments are more transparent for 7000 A radiation than for most of the visible radiation.

Of the wide spread of pigmentations found in human eyes, the medium and dark pigmentations are probably similar to those found in the rabbits used for this experiment. Albinos were available but they are of little interest in the computation of the risk for humans. No rabbits comparable in pigmentation to the lightest non-Albino found in humans were readily available for the experiment.

Section 4
SOURCE DATA

Source data were obtained in the form of irradiation data in a very limited number of spectral bands. Further source data are expected early this fall from computations performed on raw data which were only recently received by Lockheed. (See classified supplement to this report, (U) Spectral Emittance of Atomic Fireballs, LMSC-B006060.)

Section 5
AIR ATTENUATION DATA

5.1 INTRODUCTION

Data on air attenuation were obtained from the literature and five model atmospheres are suggested for use in a computation of the chorioretinal burn risk.

The wavelength interval of interest is defined by two factors – the spectral dependence of the energy from the nuclear fireball, and the spectral transmission of the matter in the human eye through which the radiation must pass to reach the retina. These two factors are roughly similar in spectral dependence. The bomb radiation peaks at about 5000 A; it is small below 3650 A and also drops off rapidly toward long wavelengths, particularly beyond 1 μ. The eye transmission is zero for wavelengths shorter than 3400 A, is maximum at 8000 A, and drops off rapidly to longer wavelengths, becoming essentially zero at 16,500 A. The region of interest for this study was specified as from 3400 A to 16,500 A; because of the fall off in both eye transmission and emitted radiation, the region beyond 10,000 A (1 μ) is relatively unimportant compared to the shorter wavelengths.

Attenuation in the atmosphere arises from scattering and absorption. In most of the wavelength region under consideration, scattering is the dominant mechanism. Absorption obviously produces a loss of energy from the radiation field; in the geometry of the eye damage problem, all scattering does also. Only undeviated radiation contributes to the formation of the image on the retina; radiation scattered into or out of the beam even at very small angles is effectively lost although it may contribute to the diffuse irradiation of other parts of the retina. (Multiply-scattered radiation may be included in the image, but this is of negligible intensity.) We shall be concerned,

therefore, only with total scattering cross-sections and not with their angular dependence.

In this section, the various mechanisms which produce scattering and absorption will be considered individually, followed by a brief discussion of the overall calculation procedure for different atmospheric conditions.

5.2 MOLECULAR (RAYLEIGH) SCATTERING

5.2.1 Attenuation Formulas

Attenuation of radiation by scattering follows the relation (see, e.g. Ref. 1)

$$\frac{dI_\lambda}{d\ell} = -k_\lambda I_\lambda \quad \text{or} \quad I(\lambda) = I_0(\lambda)\exp(-\int k_\lambda d\ell) \tag{5.1}$$

where k_λ is the monochromatic extinction coefficient and ℓ, the path length. In a pure atmosphere containing no particulate matter, the only scattering is that produced by statistical fluctuations in the local density of the gas. This was first treated theoretically by Rayleigh in his discussion of the color of the blue sky. The scattering by such a "molecular" atmosphere is given by

$$k_{m\lambda} = \frac{32\pi^3(n-1)^2}{3N\lambda^4}\ \text{cm}^{-1} \tag{5.2}$$

where

n is the refractive index of air (approximately 1.00029)
N the number of molecules per cubic centimeter
λ, the wavelength in cm

Substituting for n, and using the value of N for standard conditions, we obtain

$$k_{m\lambda} = \frac{1.03 \times 10^{-3}}{\lambda^4} \text{ km}^{-1} \qquad (5.3)$$

where λ is in microns.

The values of $k_{m\lambda}$ for different wavelengths at sea level are as follows:

$\lambda\mu$	λA	k_m in km^{-1}
0.4	4000	0.0402
0.6	6000	0.00792
0.8	8000	0.00251
1.0	10000	0.00103
1.2	12000	0.000495
1.4	14000	0.000268
1.6	16000	0.000157

Molecular scattering is proportional to the air density through the factor N; the scattering coefficient therefore decreases approximately exponentially with height. The total scattering for a vertical path through the entire atmosphere can be obtained simply by multiplying the tabulated value in km^{-1} by the scale height of the atmosphere, 8 km.

5.2.2 Computation Procedure

The scattering calculated using the molecular scattering formulas is the minimum scattering which would be produced by a perfectly clear atmosphere containing no suspended matter. Scattering levels of this level have been observed under special conditions, such as in the Belgian Congo during the rainy season, and at higher altitudes. Dunkelman and Scolnik (Ref. 2), for example, observed attenuation about 15 percent greater than that given by the Rayleigh formula in solar observations from Mt. Lemmon in Arizona at an

altitude of 9180 ft. (As will be seen below, the scale height for the suspended matter in the atmosphere is usually only about one kilometer, so while particulate scattering predominates in the lower levels of the atmosphere, the scattering at higher levels is more purely molecular.)

Calculation of the total molecular scattering in the path between a burst and an observer can be made as follows:

- For a burst at the same altitude as the observer, multiply the value of k in km^{-1} by the distance in km. (The values calculated from Eq. (5.4) below are for sea level; for other altitudes, the values should be corrected by the ratio of the atmospheric pressure to that at sea level.)
- For a burst at altitude h, multiply the values of k calculated from Eq. (5.3) by the factor F.

$$F = \frac{8(p_o - p_h)}{p_o \cos\theta} \tag{5.4}$$

where p_o and p_h are the pressures at sea level and burst altitude respectively, and θ is the angle between the vertical and the line of sight from the observer to the burst point. For a burst at high altitude directly overhead, this factor reduces to the value of 8, characteristic of a vertical path through the entire atmosphere.

5.3 PARTICULATE SCATTERING

5.3.1 Attenuation Formulas

The basic equation for the attenuation coefficient for scattering by spherical particles of radius a is calculated from Mie scattering theory (Ref. 1) to be

$$k_p = N\pi a^2 E(\alpha) \tag{5.5}$$

where

$E(\alpha)$ is an "efficiency factor" which is a function of the quantity

$$\alpha = \frac{2\pi a}{\lambda} \tag{5.6}$$

where a is the radius of the particle.

The function $E(\alpha)$ is plotted in Fig. 5-1 for nonabsorbing spherical particles with refractive index of 1.33 (i.e. water droplets, which are the predominant component of natural aerosols.) The following characteristics of this curve are notable:

- For particles with diameters greater than about four times the wavelength, E is approximately constant and equal to 2. (The total scattering cross section is then twice the geometrical area, resulting from equal contibutions from obscuration and diffraction.) For particles in this size range, i.e. greater than about 4 μ in diameter for the wavelength range of interest here, k_p is independent of wavelength.
- For small values of α, corresponding to small particle sizes or short wavelengths, E approaches zero as α^{-4}. This gives a λ^{-4} dependence as for Rayleigh scattering.
- E goes through a maximum for water droplets for $\alpha = 6$, corresponding to particles with the diameter equal to twice the wavelength.

5.3.2 Effects Due to a Distribution of Particle Sizes

Natural aerosols are characterized by a distribution of particle sizes over a wide range. The pioneering work in this area was done by Junge (Ref. 3), who showed that natural hazes are characterized by a size distribution of the form

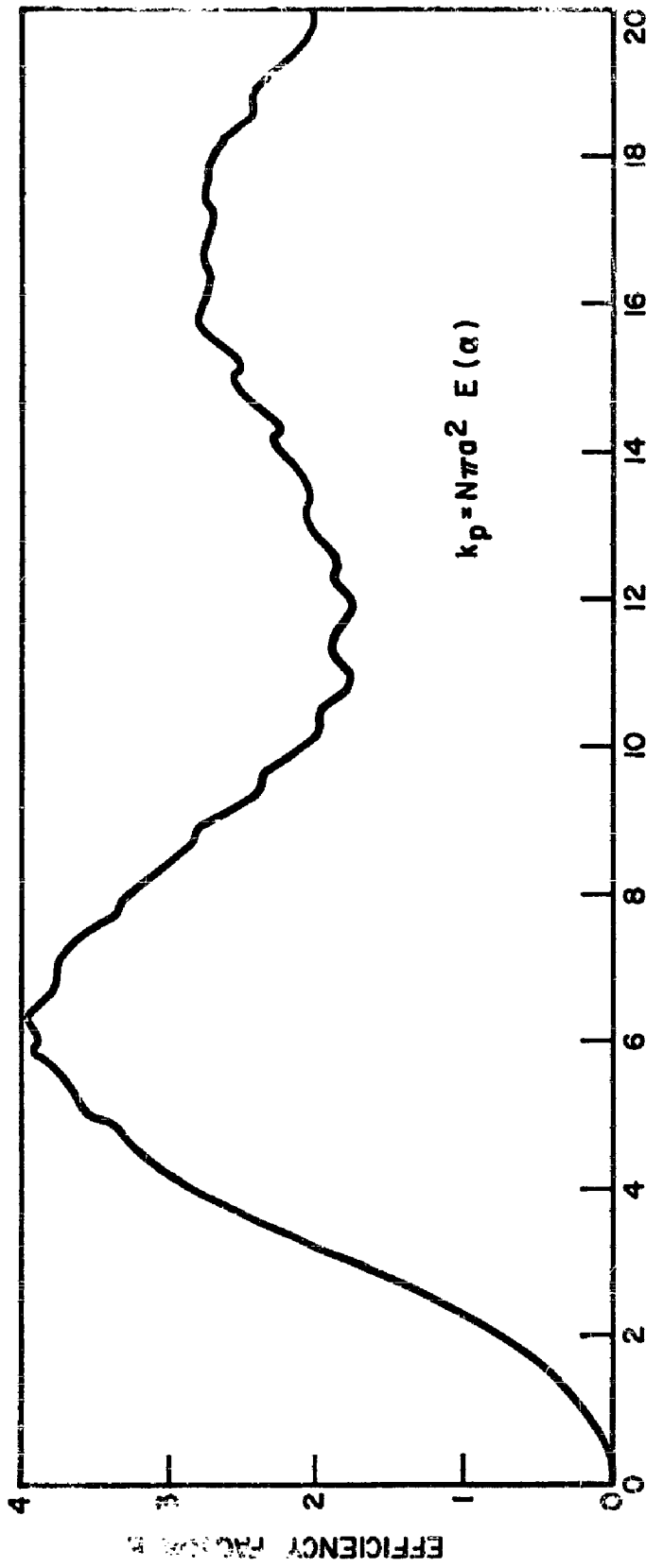

Fig. 5-1 Efficiency Factor E Versus $\alpha = \frac{2\pi a}{\lambda}$ for Spherical Particles

$$dn = c\, a^{-4}\, da \tag{5.7}$$

for ranges of a from 5×10^{-6} cm. to 5×10^{-3} cm. Here, dn is the number of particles in the size range dr, and c is a constant. Substituting Eq. (5.7) in Eq. (5.5) and integrating,

$$k = c \int_{a_1}^{a_2} \pi a^2 \sigma^2 \frac{da}{a^4} = \frac{c'}{\lambda} \int_{\alpha_1}^{\alpha_2} E(\alpha) d\alpha \approx \frac{c''}{\lambda} \tag{5.8}$$

For such a particle size distribution, the attenuation due to scattering will vary as $1/\lambda$. Experimentally, this is found to be approximately true; the transmission of most hazes in continental air masses varies as λ^{-n}, with n between 0.8 and 1.5. Maritime atmospheres are characterized by attenuation which is more nearly independent of wavelength, showing the presence of a greater relative abundance of larger particles.

Measurements have shown that the particle size distribution varies little with altitude, with the total particle density decreasing exponentially with a scale height of 1.0 to 1.4 km. compared with 8 km. for the atmosphere as a whole.

5.3.3 Relation to Visibility

The total particle content of the atmosphere varies widely. Actual particle counts are difficult to make; it is convenient to relate the scattering properties to some quantity more easily measured. Such a quantity is the meterological range, or visibility, determined by the distance at which an object can be just detected against the horizon. It can be shown (Ref. 4) that the contrast C of an object of brightness B viewed against a background of brightness B' varies as

$$C = \frac{B - B'}{B} \exp(-k\ell) \tag{5.9}$$

where k is the scattering coefficient per unit distance, and ℓ is the distance. Experiments show that the limiting contrast discernible is about 0.02 to 0.05, with a median of 0.031 according to Ref. 4. The range corresponding to this condition is known as the visibility range V. Substituting in Eq. (5.8), for C = 0.031, we obtain

$$k = \frac{3.5}{V} \tag{5.10}$$

This is an approximate relation, but serves to give the order of magnitude of the scattering coefficient for different conditions. As it is determined visually, this value of k corresponds to an effective wavelength of about 0.55μ; the values for other wavelengths can be estimated by choosing a wavelength dependence suitable for the type of atmospheric conditions prevailing at the time: $1/\lambda$ for most continental haze conditions, $1/\lambda^2$ to $1/\lambda^3$ for exceptionally clear conditions, and independent of λ for maritime atmospheres.

The visibility range calculated for a pure molecular atmosphere with only Rayleigh scattering, using Eq. (5.3) for λ = 0.55 microns, and Eq. (5.10), is 310 km, or nearly 200 mi. Experimentally observed scattering coefficients in real atmospheres vary typically from 0.05 to 1.0 km^{-1}, corresponding to visual ranges from 3 to 70 km.

5.3.4 Detailed Scattering Calculations

The most detailed treatment of scattering by atmospheres with different aerosol contents has been given by Diermendjian (Ref. 5). His calculations of the transmission of the entire atmosphere for three different particle size distributions are tabulated as follows:

Model A	N = 1352.8	$cm^{-3}\ \mu^{-1}$	$0.03\mu \le a \le 0.10\mu$
	$N(a) = 42.780\ a^{-1.5}$	$cm^{-3}\ \mu^{-1}$	$0.10\mu \le a \le 0.50\mu$
	$N(a) = 15.125\ a^{-3}$	$cm^{-3}\ \mu^{-1}$	$0.50\mu \le a \le \infty$

Model B	N	=	982.2	$cm^{-3}\,\mu^{-1}$	0.03μ	$\leq a \leq$	0.10
	$N(a)$	=	$31.06\,a^{-1.5}$	$cm^{-3}\,\mu^{-1}$	0.10μ	$\leq a \leq$	0.35
	$N(a)$	=	$2.251\,a^{-3}$	$cm^{-3}\,\mu^{-1}$	0.35μ	$\leq a \leq$	∞
Model B'	Same as Model B but with twice the particle count							
Model C	N	=	2.251×10^{4}	$cm^{-3}\,\mu^{-1}$	0.03	$\leq a \leq$	0.10μ
	$N(a)$	=	$2.251\,a^{-4}$	$cm^{-3}\,\mu^{-1}$	0.10	$\leq a \leq$	∞

These models are all based on actual particle counts. None of them include particles of size less than 0.03 μ, as this is well within the Rayleigh size range. Model A, with the largest number of large particles, corresponds to a turbulent marine atmosphere; Model B, with intermediate large particle content, to coastal air; and Model C, with an a^{-4} dependence, to continental air. The altitude dependence for all the models is the same – an exponential decrease with altitude with a scale height of 0.98 km.

Diermendjian gives a series of curves showing the total normal optical thickness of the cloudless atmosphere at sea level, calculated for the various aerosol models listed above, as a function of wavelength. This figure is reproduced in this report as Fig. 5-2. The calculation also includes the effect of molecular scattering; the curve for the pure molecular atmosphere is included in the figure. It is evident that, when the entire atmopshere is traversed, the scattering at wavelengths shorter than about 0.35 μ is predominantly Rayleigh or molecular scattering, while at longer wavelengths it is determined primarily by the particulate content.

In the interpretation of Fig. 5-2, it must be remembered that the scale height for the molecular scattering is 8 km, while for the particulate scattering is only about 1 km. Therefore, in horizontal or near-horizontal paths, i.e. for low altitude bursts, the Rayleigh scattering component will be much less important compared with the particle scattering than is indicated in Fig. 5-2. In Fig. 5-3, the scattering coefficients per kilometer for the different aerosol distribution models are plotted. These were determined by subtraction of the molecular scattering curve from the various model atmosphere curves

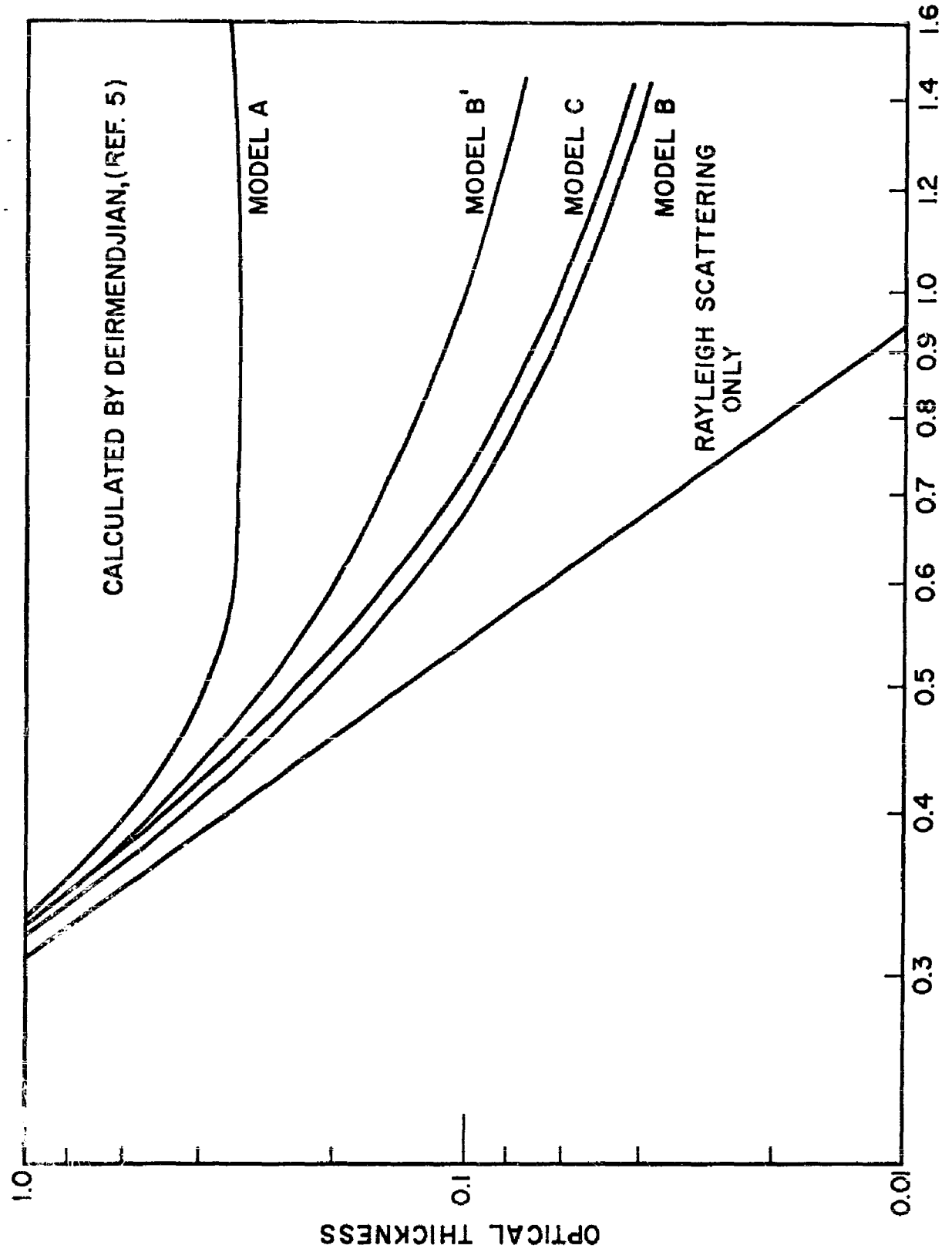

Fig. 5-2 Total Normal Optical Thickness of the Atmosphere for Various Model Aerosols

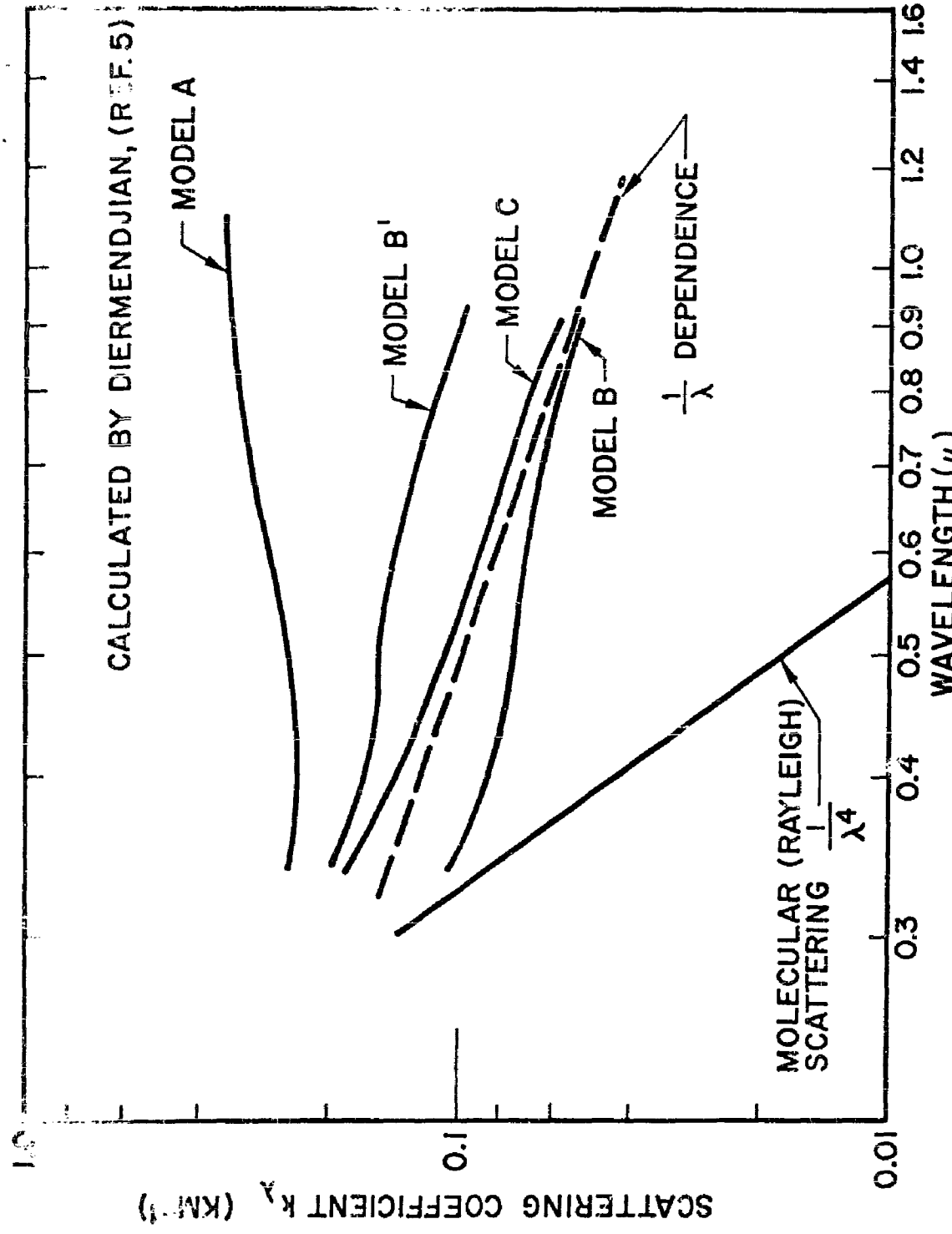

Fig. 5-3 Scattering Coefficient Versus Wavelength for Different Aerosol Models

on Fig. 5-2; the precision of this procedure is not high, but the results show the general character of the scattering from these model aerosols. The scattering from Model C follows a $1/\lambda$ dependence, as it should from its a^{-4} size distribution (see Eq. 5.8 above). Model B falls off less rapidly with wavelength, following approximately $\lambda^{-0.6}$. Model A shows a scattering dependence which actually increases with wavelength; this is a result of the fairly large number of particles with particle sizes larger than 2 μ in diameter. (From Fig. 5-1, particles with diameter 2μ, having $\alpha = 12$ for $\lambda = 0.5\mu$, will show scattering increasing with wavelength in the wavelength range from 0.5 to 1.0μ.)

Curcio (Ref. 6) has also published a series of calculated scattering curves for different size distributions of aerosol particles. He has considered particularly two-component distributions, containing "continental" and "maritime" distributions, which he used in interpreting his experimental scattering curves obtained in the Chesapeake Bay region. These measurements extended into the infrared to 2.3 μ; he was particularly interested in the large particle (maritime) component which is responsible for most of the scattering at long wavelengths.

5.3.5 Experimental Determinations of Particle Size Distributions and Scattering Curves

Before specifying scattering functions appropriate for different model atmospheres, it is useful to examine the experimental data briefly to aid in the selection of a physically reasonable size distribution function or, alternatively scattering function. Some of the pertinent data from the literature are summarized below.

- Extensive studies have been made on continental atmospheres, both in Europe and in the United States (Ref. 1, p. 167 and Ref. 7). These have included some direct particle counts; the majority have been limited to determination of the scattering as a function of wavelength. In the majority of cases, the scattering varies as $\lambda^{-\gamma}$, with γ from 0.7 to 1.8, corresponding to a size distribution approximately as a^{-4} (see

Eq. 5.8). The total number of particles varies widely as is indicated by the range of visibilities encountered; the form of the distribution varies relatively little, and is independent of altitude except in the presence of pronounced layering. It varies little with relative humidity, except at humidities near 100 percent, when larger particles are more frequent. The total number of particles in the scattering size range increases with humidity.

- Maritime atmospheres are characterized by a much larger number of large particles 1 μ in radius and larger (Ref. 3), derived from sea spray. The number of particles is a function of the wind speed. Coastal areas tend to have an intermediate distribution, which can be treated as a continental-type aerosol with admixture of a varying amount of maritime particles.
- Air pollution in large cities results primarily in an increase in the total number of particles with little change in the size distribution which is usually "continental." The total particle count can be increased by as much as a factor of 30 in heavy smog (Ref. 3), with a corresponding reduction in the visibility range.
- Some specific examples of recent measurements are as follows:

  (1) Curcio (Ref. 6) reported a series of eight scattering curves determined in the Chesapeake Bay region with meteorological visibility ranges from 4 to 160 km. The curves show predominantly a $1/\lambda$ dependence in the visible region, with some excess scattering in the infrared showing the presence of an excess of large particles (from the "maritime" component). The observed scattering coefficient at 0.55 μ ranged from 0.95 km^{-1} to 0.03 km^{-1}.

  (2) Yates and Taylor (Ref. 8), measured the transmission between mountain peaks in Hawaii at an elevation of 11,000 ft. The attenuation curve was flatter because of the greater number of large particles; the scattering coefficient varied approximately as $\lambda^{-0.3}$, with an appreciable Rayleigh component below 0.5 μ. The value of the scattering coefficient at 0.55 μ was 0.045 km^{-1}.

(3) Gibbons and his associates have measured the atmospheric transmission in the Yucca Flat region in Nevada (Ref. 9). He determined the total extinction by measurements of the apparent source intensity for different distances from the source, and the scattering independently by integration of the results from a polar nephelometer. The observed attenuation coefficient at 0.5 μ was 0.06 km^{-1}. The spectral dependence of the scattering measured with the nephelometer was about λ^{-2}; the attenuation in the long paths on the other hand increased somewhat with wavelength. He attributes this to water vapor absorption but says that "this does not seem sufficient to explain the rather high values." In addition, he observed a minimum attenuation on a cloudy night which he attributed to excess scattering from the cloud layer above; this minimum was much larger than that attributed to water vapor absorption in the other measurements when the humidity would be expected to be lower. It appears that his long-path measurements were effected by dust in the atmosphere near the ground; a relatively small number of large particles would produce the observed magnitude and wavelength dependence.

5.3.6 Computation Procedure for Particle Scattering

The procedure in this case is much the same as for molecular scattering, except that the magnitude and wavelength dependence vary with the atmosphere considered, and the scale height is one kilometer instead of eight. The magnitude of the scattering coefficient can be taken from one of the experimental or theoretical studies, summarized above, or can be estimated from the visibility range. In most cases, a $1/\lambda$ dependence adequately describes the variation of scattering with wavelength, with a somewhat slower variation for maritime and dusty atmospheres which have a size distribution including a greater number of micron-sized particles.

5.4 ATMOSPHERIC ABSORPTION

5.4.1 Attenuation Mechanism

In the wavelength range of interest here, the only significant absorber is water vapor. Other atmospheric gases, notably ozone, produced measurable

absorption in some wavelength regions, but the total effect is negligible within the accuracy of the attenuation calculations discussed here in view of the much larger variations arising from uncertainties in the attenuation produced by other mechanisms.

Water vapor has weak absorption bands centered at 0.72 μ, 0.81 μ, 0.94 μ, and 1.13 μ, and a stronger band centered at 1.4 μ. (In addition, it shows some minor bands in the visible region which are too weak to be of importance here.) The absorption of these bands does not follow the exponential dependence shown in Eq. (5.1); although any given infinitesimal wavelength range would follow this relation, the variation of absorption coefficient with wavelength in the individual lines of which these bands are composed is so rapid that any measurement interval covers a wide range of absorption. The net absorption by molecular bands of various types has been investigated both theoretically and experimentally, and numerous empirical and theoretical relations are available. Particularly complete studies of the absorption by water vapor have been made by the Ohio State University group under Dr. Williams. Curves given by Howard (Ref. 10) for the transmission in four wavelength ranges covering the interval 0.70 to 1.61 μ are reproduced in Fig. 5-4 of this report. In these curves, the transmission is given as a function of the number of "precipitable centimeters" of water vapor in the path; the absorption also varies somewhat with pressure, but the effect is not large enough to be of importance here.

The water content in precipitable centimeters for a given path can be calculated simply if the absolute humidity along the path is known; it is simply the total mass of water vapor contained in tube 1 cm^2 in cross section along the line of sight.

5.4.2 Computation Procedure

If the total water vapor content of the path is known, the absorption correction can be made by simply multiplying the radiation for a given wavelength by the transmission factor given in Fig. 5-4 for that wavelength. Although

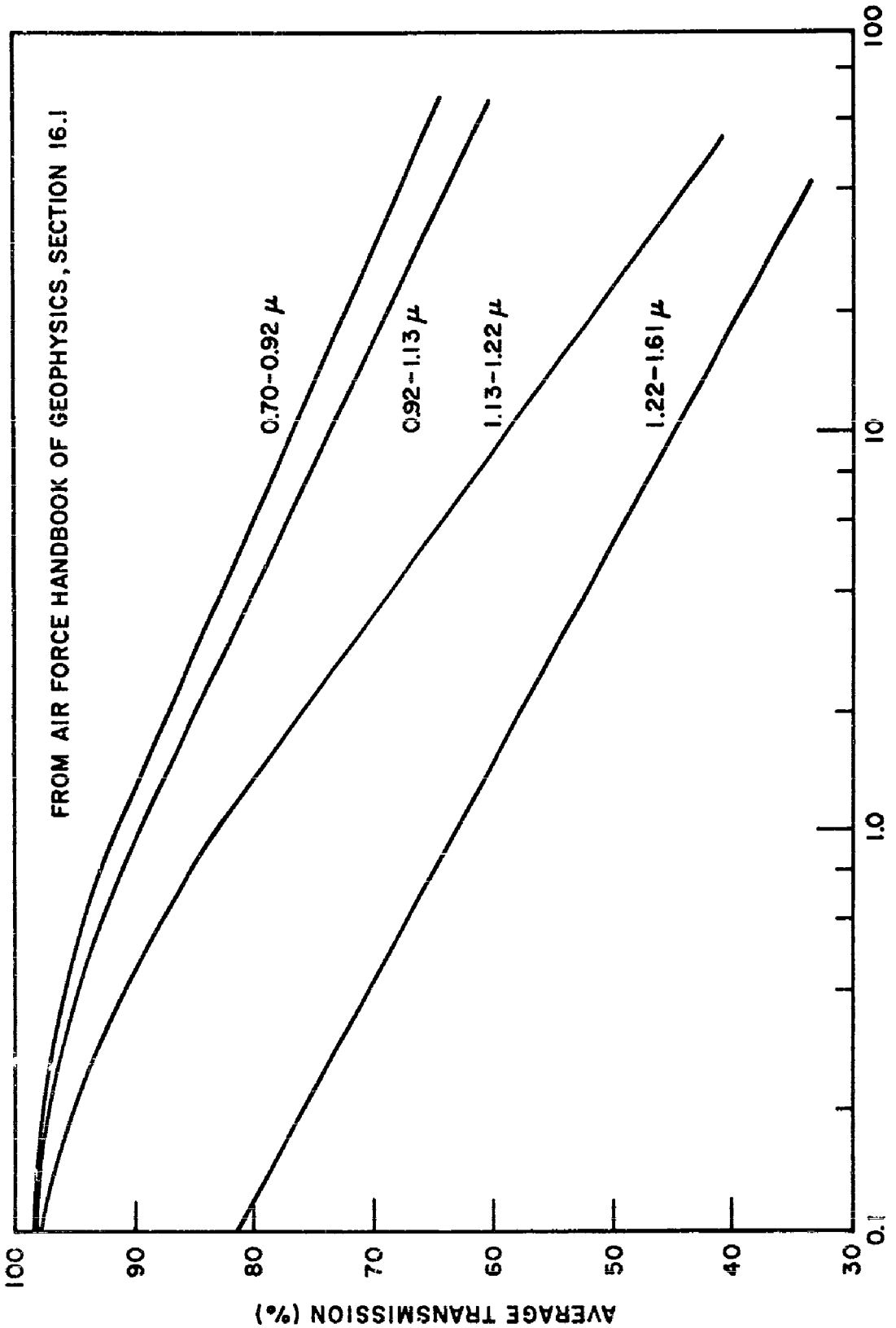

Fig. 5-4 Percent Transmission Versus Water Vapor Content in Path

this is only an approximate treatment, it is believed that it is sufficiently accurate in this case in view of the relatively small amount of radiation in the long wavelength region where the absorption is important.

The computation of the water vapor content is not as simple since the amount of water vapor in the atmosphere is so widely variable. The precipitable water in a one kilometer path at sea level, for example, varies from 0.22 cm for 0°F, 25 percent RH, to 4.4 cm. for 100°F, 100 percent RH—a factor of 2,000. Similarly, the total water vapor content in a vertical path over North America can vary from 1 mm to 10 cm or more.

For estimation of the water vapor content in a given path for different climatic conditions, the following procedure gives reasonably accurate results for average conditions (Ref. 11). The precipitable water per kilometer at ground level can be calculated directly from the temperature and relative humidity. (It is numerically equal to one tenth of the water vapor content in grams per cubic meter.) The total amount of water vapor in a vertical column through the entire atmosphere can be estimated by multiplying that quantity by a "reduced height" of approximately 2.5 km. This value has been shown to be valid over a range of sea-level temperatures from -10°C to +25°C under reasonable meteorological assumptions. In most cases, the bulk of the water vapor is below an altitude of 5 km; for bursts at altitudes greater than this, the total water in the path can be calculated from the total in a vertical path and the angle of sight to the burst point as in the case of scattering. In many cases, of course, the water vapor distribution will be widely different from an "average" case; such special cases would have to be treated individually in detail.

5.5 PROCEDURES FOR CALCULATION OF TOTAL ATTENUATION BY DIFFERENT ATMOSPHERES

5.5.1 Recapitulation of Calculation Techniques

For a burst at the same altitude as the observer, the atmospheric transmission is given by

$$I(\lambda) = I_o(\lambda) \exp -\left\{\left[k_m(\lambda) + k_p(\lambda)\right]\right\} \ell\, T(w\ell) \qquad (5.11)$$

where $k_m(\lambda)$ and $k_p(\lambda)$ are the scattering coefficients per kilometer for molecular and particle scattering respectively, ℓ is the path length in kilometers, T is the transmission function for water vapor, and w is the water vapor content in precipitable centimeters per kilometer of path.

For a high-altitude burst,

$$I(\lambda) = I_o(\lambda) \exp -\left\{\left[k_m(\lambda)\, H_m + k_p(\lambda)\, H_p\right]\right\} T(wH_w) \sec\theta \qquad (5.12)$$

where H_m, H_p, and H_w are the scale heights for the molecular atmosphere (8 km), the particle distribution (1.2 km) and the water vapor (2.5 km), and θ is the angle between the vertical and the line of sight between the observer and the burst point.

For all atmospheres, $k_m(\lambda) = 1.03 \times 10^{-3}/\lambda^4$ km^{-1} (λ in microns) at sea level, decreasing with the atmospheric density as altitude increases.

The particle scattering coefficient $k_p(\lambda)$ depends on the aerosol content of the particular atmosphere. In the absence of detailed information, the value of k_p for $\lambda = 0.55\,\mu$ can be determined from the meteorological visibility through the relation $k_p(0.55\,\mu) = 3.5/V$, and correcting for Rayleigh component; values for other wavelengths obtained by assuming a $1/\lambda^{\gamma}$ dependence

of k, with $\gamma = 1.0$ for continental atmospheres, and 0.5 to 0 for maritime atmospheres.

For altitudes less than about three scale heights for a given attenuation mechanism, a more exact procedure must be used. In most cases this will take the form of a correction to Eq. (5.12) for the amount of scatterer or absorber above the burst altitude. Nonexponential altitude distributions of particles or water vapor will require a detailed integration along the path to determine the amount of scatterer or absorber present.

5.5.2 Model Atmospheres

Different model atmosphers can be constructed by specifying aerosol and water vapor content. The following are considered appropriate for the eye damage calculations:

(1) Pure molecular atmosphere, with no aerosol or water vapor. The only attenuation mechanism is Rayleigh scattering, k_m; $k_p = 0$ and $T(w) = 1$.

(2) Nevada desert. Rayleigh (molecular) scattering is 90 percent of value at sea level because of the altitude; $k_p(\lambda) = 0.010\ \lambda^{-1}\ km^{-1}$ (λ in microns), derived from Gibbons' measurements (Ref. 9); this corresponds to a visual range of 70 mi. Water vapor 0.3 prec. cm./km. (from Gibbon's measurements; this corresponds to 16 percent relative humidity at 70°F).

(3) Continental atmosphere. Rayleigh as above; particle scattering $0.55\ \lambda^{-1}\ km^{-1}$ (Diermendjian's model C, Fig. 5-3). Water vapor 0.9 prec cm/km (70°F., 50 percent RH).

(4) Smoggy atmosphere. Conditions as in (3) except with larger particle scattering. Twenty times the particle content, giving $k_p = 0.55\ \lambda^{-1}\ km^{-1}$, corresponding to about 1-mi visibility.

(5) Tropical maritime atmosphere. k_m as above; k_p = 0.3 km^{-1} indepdendent of wavelength (Diemendjian's model A) corresponding to visibility of 12 km. Water vapor content 2.4 prec. cm./km. (corresponding to 85°F, 80 percent RH).

Section 6
THEORY AND COMPUTATIONAL METHODS

6.1 INTRODUCTION

6.1.1 Purpose

This section presents the formulation of a method for calculating the temperature response of the retina in a human eye to thermal radiation from nuclear explosions. The information is to be used in determining threshold distances for retinal damage as a function of nuclear yield with various combinations of atmosphere, eye pigmentation, and observer altitude.

6.1.2 Scope

A discussion of the physical phenomena involved in the transmission of thermal energy to the retinal image precedes a definitive statement of the problem. The discussion then turns to the method of solution that has been programmed on the IBM 7090 Digital Computer. How the results of the computer program are to be used and a discussion of computer time requirements for completing the task are presented in subsection 6.3.

6.2 PROBLEM DEFINITION

6.2.1 Physical Aspects of the Problem

A nuclear explosion occurring above the surface of the earth is characterized by a roughly circular fireball that grows in size and emits vast amounts of thermal radiation in a very short time interval. A human looking toward the point of detonation has a portion of that energy, in both visible and infrared wavelengths, focused on the image of the fireball that is formed on the

retina before the blink reflex occurs. The irradiance of the image depends on fireball emittance, atmospheric attenuation, the square of the relative opening of the eye (pupil radius divided by focal length) and attenuation in the ocular media in a spectral range from 0.36 to 1.6 μ wavelengths.

Nearly all of the radiation incident at the retinal image is absorbed in the pigment epithelium and chorioid except for albinotic eyes. This very localized energy absorption results in rapid temperature increases. The amount of increase is determined by the thermal capacity of the absorbing material and the rate of heat conduction away from the affected element. Heat transfer by conduction will occur in all directions from the heated material where a temperature gradient exists. It will be retarded, however, in flowing radially from the more central portions of the image owing to the fact that the image is expanding and the outer portions are also receiving thermal energy by radiation.

Both the time history of irradiation and the total image area involved have a decided effect on the temperature response of the initial image, where experience has shown that retinal damage is most severe. The yield of the nuclear device affects both the nature of the emittance and the total image area involved. In addition, the distance of the eye from the fireball affects the size of the image. It should be possible, therefore, to determine threshold range as a function of nuclear yield for a given set of conditions, i.e., detonation altitude, atmosphere, observer altitude, eye pigmentation, and blink reflex time, by examining temperature-time histories of the pigment epithelium and adjacent elements that lie within the retinal image.

This approach is believed to be a more accurate one than has previously been attempted because threshold values for heat damage to living cells are determined by "time at temperature" rather than by total heat absorption.

6.2.2 Definitive Problem Statement

A technique for calculating the transient temperature response of the pigment epithelium and adjacent layers of the retina and chorioid receiving thermal radiation from a nuclear fireball is to be formulated. Specifically the computation technique should provide for the following factors:

- Starting with experimentally obtained irradiation or theoretically calculated fireball emittance, having given spectral distribution, calculate the incident radiation on the retinal image as a function of time.
- Calculate the absorption of thermal energy in various sublayers of the retina and chorioid as a function of time and radiation wavelength.
- Determine the transient conduction of heat away from the affected elements of the retina and chorioid, and their corresponding temperature-time histories.

6.3 PROBLEM SOLUTION

6.3.1 Determining Image Size

In the determination of the image size on the retina, geometrical optics of a reduced eye is used. It is calculated as

$$R_i = \frac{f}{R_e}(R_f) \tag{6.1}$$

where

R_i = image radius

R_f = fireball radius

R_e = range from eye to nuclear explosion

f = distance of nodal point from retina

Although not exact, Eq. (6.1) is a convenient approximation and will be used until the magnitude of the error introduced has been shown to be significant. The radius of the retinal image is calculated as a function of time, by the computer, utilizing values of fireball radius as part of the input.

6.3.2 Calculating Incident Radiation on Retina

The incident thermal radiation on the retina is, for each wavelength and time interval, calculated by an equation of the following general form.

$$H_i = C_1 H_o R_f^{-2} \exp -\left[\left(\alpha_m + \alpha_p\right)\left(R_e - R_f\right)\right] f_w \exp - \left(\alpha_{oc} \ell_{oc}\right) \qquad (6.2)$$

where

H_i = irradiance on retinal image

C_1 = coefficient = $(R_o D_e/2f)^2 f_1 f_2 \ldots f_n$

H_o = irradiance on calorimeter during nuclear testing

R_o = range to calorimeter from air-zero

α_m = atmospheric attenuation due to molecular scattering

α_p = atmospheric attenuation due to particle scattering

f_w = transmission factor of atmospheric water vapor

α_{oc} = attenuation coefficient in ocular media

ℓ_{oc} = path length in ocular media

D_e = Pupillary opening diameter

$f_1 f_2 \ldots f_n$ = transmission factors for lenses and other optical media when considered (correction factors were required)

By the appropriate manipulation of Eq. (6.2), many variables can be accounted for. For example, if desirable, experimental calorimeter irradiance can be replaced with fireball emittance from theoretical calculations by setting both R_o and R_f equal to one. Where either or both the nuclear detonation and the observer are within the sensible atmosphere, the atmospheric attenuation factor can be set equal to one and a correction factor employed to make use of the reduced atmosphere concept that is discussed in another section of this report.

Although mentioned previously it should be stressed that the spectral characteristics of the radiation from the fireball, and its transmission and attenuation will vary with time in this problem. The use of a digital computer allows the rapid calculation of incident radiation as a function of both wavelength and time with high resolution.

6.3.3 Absorbed Radiation in Retina and Chorioid

The transmission of radiation in the retina and chorioid is assumed to follow the exponential law used in the preceding discussion on incident radiation. The absorption of thermal energy in each sublayer ($\not{H}$) is taken as the difference between the irradiance (H) at its boundaries.

The essential part of the thermal model for this problem is a circular disc composed of (1) sensory cells, (2) pigment epithelium, (3) chorioid, and (4) a layer of blood located within the chorioid. The latter subdivision makes it possible to include the effects of blood circulation on heat disposal particularly after the blink reflex has occurred. Forward of the disc are ocular media and in back of it is the covering of the eyeball, or sclera. The absorbed thermal energy in the sensory cells ($\not{H}_{se}$) is:

$$\not{H}_{se} = (H_i - H_{pig})A = H_i A \left[1 - \exp -(\alpha_{se} \ell_{se})\right] \qquad (6.3)$$

with

H_{pig} = irradiance on pigment epithelium

α_{se} = attenuation coefficient in sensory cells

ℓ_{se} = path length in sensory cells

A = projected area irradiated

The absorbed thermal energy in the pigment epithelium ($\not{H}_{pig}$) is

$$\not{H}_{pig} = \left(H_{pig} - H_{ch}\right)A = H_{pig}\, A \left[1 - \exp - \left(\alpha_{pig}\, \ell_{pig}\right)\right] \qquad (6.4)$$

with

H_{ch} = irradiance on chorioid

α_{pig} = attenuation coefficient in pigment epithelium

ℓ_{pig} = path length in pigment epithelium

The absorbed thermal energy in the chorioid ($\not{H}_{ch}$) is

$$\not{H}_{ch} = \left(H_{ch} - H_{sc}\right)A = H_{ch}\, A \left[1 - \exp - \left(\alpha_{ch}\, \ell_{ch}\right)\right] \qquad (6.5)$$

with

H_{sc} = irradiance on sclera

α_{ch} = attenuation coefficient in chorioid

ℓ_{ch} = path length in chorioid

As noted previously, the quantities calculated by Eqs. (6.3), (6.4), and (6.5) are both wavelength and time dependent. Multiplying ΔH by an appropriate

area term and summing for all wavelengths results in a thermal energy input (calories per second) for an element of absorbing material. The thermal response of elements in a thermal model is the desired output from the digital computer and its calculation is the subject of the following section.

6.3.4 Thermal Response of the Retina

The general problem and the procedure adopted to obtain the amounts of absorbed radiation ($\dot{H}$) has been detailed in the previous sections. In this section it is shown how the retinal heat conduction problem is formulated and solved. Specifically, the absorbed radiation is taken as an input in a general set of equations governing heat transfer within the retina.

6.3.4.1 Development of a Heat Transfer Model

Figure 6-1 is a schematic of the eye; in this figure, one observes the following:

- The retinal image is small relative to the size or diameter of the eyeball.
- The eye, for all practical purposes, is symmetrical about its geometrical axis.
- The main heat absorbing layers are of small dimension relative to the radius of curvature of the eye.

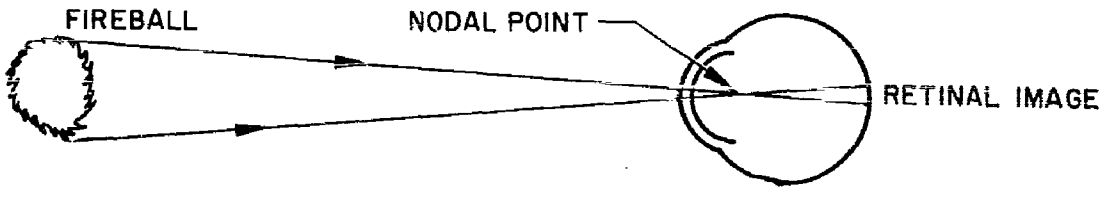

Fig. 6-1 Retinal Image Size

Figure 6-2 shows a central section of the retina and chorioid represented by concentric cylinders. The area within the eye which either receives the incident radiation or responds rapidly to its effects was shown to be small in size relative to the eyeball; consequently, effects of the eyeball curvature are assumed negligible. We need not consider the cornea or lens since these media are quite transparent in the spectral range of interest and are far removed from the major radiation absorbing regions of the eye. As a result of symmetry within the eye, further simplification in geometry is permitted. The sector of the concentric cylinders shown in Fig. 6-2 has an included angle β, which is chosen as one radian. This, then, is the geometric model of the eye used to determine internal heat transfer.

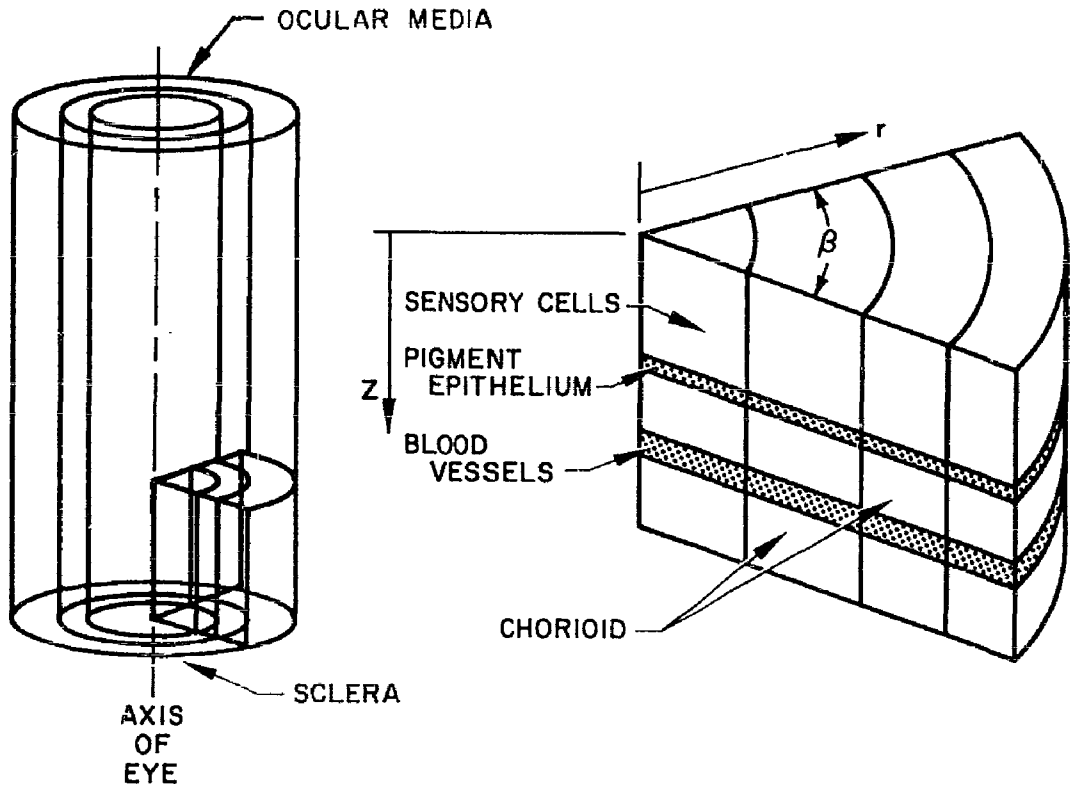

Fig. 6-2 Central Section of Retina and Chorioid

6.3.4.2 The Thermal Network and its Solution

For computational purposes, the cylindrical sector is subdivided into a network of small elements or nodes. Nodal points are centrally located in each element. Heat transfer between elements is equivalent to heat transfer between nodal points since the temperature of an element is represented at its nodal point. The nodal system as utilized herein is shown in Fig. 6-3 for a two-dimensional network consisting of n nodes by m nodes. In the computer program designed to determine the thermal response of this network, it is possible to consider as many as 100 nodes.

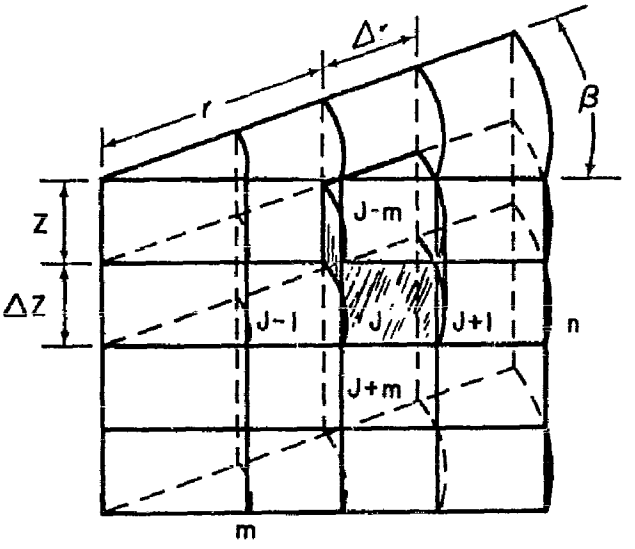

Fig. 6-3 Computational Grid

The instantaneous rate of temperature change of any element within the retina is determined by the net rate of gain or loss of energy per unit volume of that element. The heat balance for an elemental portion of the retina, such as that shown at r and z in Fig. 6-3, is

$$\rho c_p V \frac{\partial t}{\partial \theta} = Q_c + \not{\Phi} \qquad (6.5)$$

where Q_c is the net rate of heat transferred by conduction in the radial and axial directions, and $\not{H}$ is the radiation absorbed from the fireball. It is assumed that the radiation contributing to heating is collimated. In addition, the internal emission and reflection occurring within the eye is, for this problem, of little consequence.

The radiation absorbing layers within the eye are small relative to the dimensions encountered in most heat transfer problems; consequently, considerable difficulty would be encountered where an explicit complete-difference formulation (Ref. 12) of the heat conduction equation is applied to Eq. (6.6). Difficulty would result because the stability criterion imposed upon the difference equations would require exceedingly small computing intervals, $\sim(10^{-6}$ sec), resulting in excessive computing time. In the present program, an implicit complete-difference formulation of the heat conduction equation is applied. The basic development of both types of difference equations is described in Refs. 13 and 14. For the numerical formulation used, stability of the difference equations is guaranteed for essentially any value of the selected computing interval. In addition, the interval may be chosen independent of the size of the elements in the network.

The net rate of heat transferred by conduction at the j^{th} node (see Fig. 6-3) between computing times θ and $\theta + \Delta\theta$ is

$$Q_c = \left(\frac{k}{\ell}\right)A_{j-m,\,j}\left(t_{j-m,\,\theta+\Delta\theta} - t_{j,\,\theta+\Delta\theta}\right) + \left(\frac{k}{\ell}\right)A_{j-1,\,j}\left(t_{j-1,\,\theta+\Delta\theta} - t_{j,\,\theta+\Delta\theta}\right)$$
$$- \left(\frac{k}{\ell}\right)A_{j,\,j+m}\left(t_{j,\,\theta+\Delta\theta} - t_{j+m,\,\theta+\Delta\theta}\right) - \left(\frac{k}{\ell}\right)A_{j,\,j+1}\left(t_{j,\,\theta+\Delta\theta} - t_{j+1,\,\theta+\Delta\theta}\right) \qquad (6.7)$$

Observe in Eq. (6.7) and Fig. 6-3 that the assumed directions of heat flow are from top to bottom and from left to right in the network. Equation (6.6) yields correct results independent of the actual direction of heat flow since the same equation is solved for each node.

In Eq. (6.7) the quantity $\left(\frac{k}{\ell}\right)A$ is defined as the thermal conductance between adjacent nodes. In the digital computer program, the conductance terms are averaged with respect to size and temperature of the node in question and the adjacent node. In the radial direction

$$\left(\frac{k}{\ell}\right)A = \frac{\Delta Z_j \left(\Delta r_{j-1} + \Delta r_j\right)}{\left(\frac{\Delta r_{j-1}}{k_{j-1,\,\theta}} + \frac{\Delta r_j}{k_{j,\,\theta}}\right) \ell n \left(\frac{\sum_{a}^{j} (\Delta r) - 0.5\left(\Delta r_j\right)}{\sum_{a}^{j-1} (\Delta r) - 0.5\left(\Delta r_{j-1}\right)} \right)} \tag{6.8}$$

the log-mean area is taken in the radial direction as the heat conduction area. In the axial direction

$$\left(\frac{k}{\ell}\right)A = \frac{\left[\sum_{a}^{j} (\Delta r)\right]^2 - \left[\sum_{a}^{j-1} (\Delta r)\right]^2}{\frac{\Delta Z_j}{k_{j,\,\theta}} + \frac{\Delta Z_{j+m}}{k_{j+m,\,\theta}}} \tag{6.9}$$

Observe that the summation is evaluated from node a to either nodes j or j-1. The a^{th} node is defined as the first node in the row containing the j^{th} node. The subscript 0 refers to the property evaluated at time θ. The thermal conductivity is provided to the digital computer in the form of tabulated values as a function of temperature. The computer linearly interpolates between tabulated values. Note that

$$\left(\frac{k}{\ell}\right)_{A_{j-1,\,j}} = \left(\frac{k}{\ell}\right)_{A_{j,\,j-1}} \tag{6.10}$$

and

$$\left(\frac{k}{\ell}\right)_{A_{j+1,\,j}} = \left(\frac{k}{\ell}\right)_{A_{j,\,j+1}} \tag{6.11}$$

The network size (number of nodes = N) and the spacing of nodes are not fixed quantities. It is only required that $N_{max} \leq 100$ nodes, and that the nodes in a given column possess identical values of Δr and that nodes in a given row possess identical values of ΔZ.

Since Eq. (6.7) is written for each node, certain terms are not used depending upon placement of the node. The following scheme is therefore employed to determine the placement of a node in the network. In reference to the j^{th} node,

- If $j \leq m$ it is a node on the top surface. The heat conduction terms involving $j - m$ are not used in Eq. (6.7).
- If $j > m \cdot n - m$ it is a node on the bottom surface. The heat conduction terms involving $j + m$ are not used in Eq. (6.7).
- $\frac{j}{m} = q + R$ where q = quotient, R = remainder (6.12)
  - (a) If $R = 1$, the node is on the left boundary; therefore, terms involving $j - 1$ are not used in Eq. (6.7).
  - (b) If $R = 0$, the node is on the right boundary; therefore, terms involving $j + 1$ are not used in Eq. (6.7).
- For all other values of j, the node is internal and all terms in Eq. (6.7) apply.

6.3.4.3 Computation of Thermal Capacitance and Irradiated Area

The thermal capacitance C_j of each node is computed by solving the following expression

$$C_j = \left(\rho c_p\right)_{j,\theta} V_j \tag{6.13}$$

where (ρc_p) is the product of the density and specific heat, and V_j is the volume of the node j. The (ρc_p) product is temperature dependent and, like the thermal conductivity, is an input to the digital computer in tabular

form. The volume of the j^{th} node is determined by solving the following relation.

$$V_j = 0.5\left[\left(\sum_{a}^{j} \Delta r\right)^2 - \left(\sum_{a}^{j-1} \Delta r\right)^2\right]\Delta Z_j \qquad (6.14)$$

Because of the dependency of the thermal capacitance upon temperature, this quantity is computed for each computing interval.

The image diameter is time dependent (increasing with time); while for a given computer run, the thermal network is fixed. Consequently, the entire projected area (axial direction) of certain nodes will not be fully irradiated. As noted previously, the image radius R_i is computed from knowledge of the fireball radius, its distance from the eye, and the focal length of the eye. Thus, the image radius is known as a function of time. These computed values, then, serve as an input for solution of the internal heat-transfer problem. At any time, θ_n, $R_{i,\,\theta}$ is compared with the sum of the column dimensions (Δr). The difference between the sum of the dimensions for those nodes which are completely irradiated and the image radius yields that increment of r (which is related to an area) within certain nodes which are partially irradiated. The following expression is solved for the j^{th} node

$$R_{i,\,\theta} - \sum_{a}^{j} (\Delta r) = R' \qquad (6.15)$$

When R' is a positive quantity, then all nodes in the row (from node a) including the j^{th} are irradiated on the entire projected surface. The surface area irradiated is, then,

$$A = 0.5\left[\left(\sum_{a}^{j} \Delta r\right)^2 - \left(\sum_{a}^{j-1} \Delta r\right)^2\right] \qquad (6.16)$$

When R' is negative for the j^{th} node, then this node is partially irradiated. For this node the irradiated area is

$$A = 0.5\left[\left(R_{i,\theta}\right)^2 - \left(\sum_{a}^{j-1} \Delta r\right)^2\right] \qquad (6.17)$$

6.3.4.4 Method of Mathematical Solution

When all of the thermal parameters are applied in Eq. (6.6) it is seen that there are five unknowns, namely, the temperature of the j^{th} node and that of each of the surrounding nodes. In formulating a matrix to represent the thermal network shown in Fig. 6-3, some of the terms in the equations cancel and the difference formulae are resolved into a system of N equations with N unknowns. A Gaussian elimination technique developed by LMSC is applied to solve the system of equations.

6.4 UTILIZATION OF DIGITAL COMPUTER PROGRAM

The computer program described in this report calculates a transient temperature history for each element in the thermal model. It provides the information needed, for a particular set of parameters, to determine the threshold distance where the eye is not damaged. This is accomplished by solving the thermal network with several values of R_e. The value used in the solution that satisfies the eye damage criteria is one point for a curve of Threshold Distance (T.D.) vs. Nuclear Yield.

Initial computations will be made for low-altitude nuclear explosions where the human observer is looking in the proper direction with his eyes open at the instant of detonation. Further, it will be assumed that the eye is fully adapted for night vision. With these conditions, there are thirty distinct curves of T.D. vs. Nuclear Yield that are of interest. They represent the following parameters:

(1) Three pigmentations (light, medium and dark)
(2) Two observer altitudes (sea level and above 100,000 ft)
(3) Five model atmospheres (Pure molecular, Desert, Continental, Smoggy, and Tropical Maritime)

If it is assumed that five points are required to define one curve and that it requires four computer runs of one-tenth hour duration each to select one point, a total of 60 hr of IBM 7090 computer time would be required. This time could be halved by the use of scaling factors for observer altitude, thus reducing the computer time to approximately 30 hr. With appropriate scaling factors for the model atmospheres, the computer time would be reduced to 6 hr and for the extreme case, to 2 hr, with additional scaling factors for pigmentation. Some computer time may be required, however, in the determination of valid scaling factors.

The foregoing illustration vividly demonstrates the need for a careful analysis of possible scaling factors since the required computer time varied by a factor of 30. At $500 per hour, it would represent a difference of $29,000 for computing time.

An alternate approach to reducing computer time is to print out the results of key computations, such as Eq. (6.2). When scaling factors external to the eye are applied, it is only necessary to match the results from that equation for an identical response within the eye. In a similar fashion, when the pigmentation attenuation is changed, the results from Eq. (6.3) can be used for given sets of external parameters. At this time, however, it is not obvious what scaling can be done and thus further consideration is merited.

Section 7
REFERENCES

1. F. Moller, "Strahlung in der Unteren Atmosphere," Handbuch der Physik, Vol. 48, Springer, 1957, p. 155 ff
2. L. Dunkelman and R. Scolnik, "Solar Spectral Irradiance and Vertical Atmospheric Attenuation in the Visible and Ultraviolet," J. Opt. Soc. Am., Vol. 49, April 1959, pp. 356–367
3. C. E. Junge, "Atmospheric Composition," Handbook of Geophysics, U. S. Air Force Geophysics Research Directorate, Macmillan, 1960, p. 8-11
4. W. E. K. Middleton, Vision Through the Atmosphere, Toronto, 1952; also article by same title in Handbuch der Physik, Vol. 48, p. 254 ff
5. D. Diermendjian, "Theory of the Solar Aureole Part II. Applications to Atmospheric Models," Ann. Geophys., Vol. 15, 1959, p. 218–249
6. J. A. Curcio, "Evaluation of Atmospheric Aerosol Particle Size Distribution from Scattering Measurements in the Visible and Infrared," J. Opt. Soc. Am., Vol. 51, May 1961, pp. 548–551
7. J. A. Curcio and K. A. Durbin, NRL Report 5368, 1959 (quoted in Ref. 6)
8. H. W. Yates and J. H. Taylor, NRL Rept. 5453, June 8, 1960 (analysis given by Curcio in Ref. 6)
9. M. G. Gibbons, J. R. Nichols, F. I. Laughridge, and R. L. Rudkin, "Transmission and Scattering Properties of a Nevada Desert Atmosphere," J. Opt. Soc. Am., Vol. 51, June 1961, pp. 633–640
10. J. N. Howard, "Thermal Radiation," Handbook of Geophysics, U. S. Air Force Geophysics Research Directorate, Macmillan, 1960, p. 16-4

11. Raytheon Manufacturing Company, Extremely High Altitude Reconnaissance Study, First Quarterly Progress Report, Contract AF 33(616)-6668, Santa Barbara, Calif., 31 Dec. 1959

12. P. J. Schneider, Heat Conduction, 1st ed., Addison-Wesley, Boston, 1956

13. R. D. Richtmyer, "Difference Methods for Initial Value Problems," Interscience Tracts in Pure and Applied Mathematics, Interscience, New York, 1957

14. G. Leppert, "A Stable Numerical Solution for Transient Heat Flow," Am. Soc. Mech. Engr., Paper No. 53-F-4, 1953

Appendix A

SPECTRAL TRANSMISSION OF CHORIOID AND RETINAL PIGMENT EPITHELIUM

Spectrophotometric transmission data in three areas of both rabbit and human tissues are presented in tabular form.

Tables A-1 through A-6 are for rabbit tissue. These tables are identified by animal number, color, and eye.

Tables A-7 through A-16 give data for human tissues; these tables are identified by running numbers, H-1, H-2, etc., for each eye.

Table A-1

RABBIT NO. 10, DARK BLACK, RIGHT EYE

Wavelength (μ)	Area					
	Temporal		Central		Nasal	
	Pigment Epithelium	Chorioid	Pigment Epithelium	Chorioid	Pigment Epithelium	Chorioid
0.34	2.7	0.2	10.6	0	0.4	[illegible]
.35	8.8	.2	9.9	0	.4	15.1
.36	7.9	.2	9.2	0	.5	15.5
.38	7.0	.2	9.5	0.2	.5	16.3
.40	7.3	.2	10.2	.2	.5	17.2
.44	8.2	.3	11.8	.5	.4	18.8
.48	9.0	.2	13.9	.3	.5	21.8
.52	10.2	.2	15.7	.2	.4	24.0
.56	11.7	.3	17.5	.4	.4	26.3
.60	13.0	.3	19.7	.4	.4	28.7
.64	14.6	.3	21.0	.5	.4	31.0
.68	15.3	.4	23.0	.2	.4	32.3
.72	18.4	.4	25.2	.6	.4	35.7
.78	22.0	.3	27.5	.7	.6	38.1
.84	26.0	.5	31.0	.8	.6	41.3
.90	29.5	1.0	33.5	.8	.9	44.6
.96	32.6	1.0	36.4	.8	1.1	47.2
1.02	35.7	.9	38.9	.8	1.1	49.2
1.08	39.0	1.0	41.0	.8	1.6	51.7
1.14	41.5	1.2	43.1	1.0	1.9	53.0
1.20	44.0	1.0	45.0	1.0	2.1	55.3
1.26	46.0	1.1	47.0	1.1	2.4	56.9
1.32	48.0	1.1	48.6	1.3	2.5	58.1
1.36	50.0	1.0	49.1	1.3	2.7	58.5
1.38	49.9	1.0	49.4	1.4	2.8	58.1
1.40	48.5	.9	48.1	1.3	2.1	56.1
1.42	41.7	.8	41.8	1.1	2.0	52.2
1.44	40.0	.9	40.0	1.0	1.5	51.7
1.46	40.0	.9	39.6	.9	2.0	51.9
1.48	41.2	1.0	41.0	.8	2.0	52.9
1.50	44.0	.9	43.1	.8	2.6	54.5
1.54	48.7	1.2	48.1	1.0	3.2	58.1
1.58	52.5	1.9	51.6	1.2	3.9	60.7
1.62	54.2	2.1	53.4	1.3	4.1	61.9
1.66	56.0	2.6	55.3	1.6	4.7	63.0
1.70	56.9	3.0	56.1	1.8	5.2	63.8
1.74	57.2	3.0	56.3	1.9	5.2	64.0
1.78	57.1	3.0	56.5	2.0	5.2	63.9
1.82	57.8	3.1	56.7	1.9	5.5	63.8
1.84	57.8	3.2	57.0	2.0	5.1	63.7
1.86	57.0	3.1	56.1	2.0	4.4	63.1
1.88	52.5	2.0	53.0	2.0	3.0	56.0
1.90	34.0	1.0	34.5	2.0	.3	[illegible]
1.92	21.6	.9	20.2	1.0	.2	33.3
1.94	18.7	.5	17.5	.8	.0	32.3
1.96	21.1	.6	19.4	.7	.3	35.2
1.98	25.1	.6	24.1	.8	.7	[illegible]
2.00	30.0	.9	29.0	.9	.8	44.1

Table A-2

RABBIT NO. 10, DARK BLACK, LEFT EYE

Wavelength (μ)	Area					
	Temporal		Central		Nasal	
	Pigment Epithelium	Choricid	Pigment Epithelium	Choricid	Pigment Epithelium	Choricid
0.34	18.0	0	8.7	1.2	12.2	[illegible]
.35	18.0	0	8.2	.9	11.6	[illegible]
.36	19.2	0	7.7	.6	11.0	.5
.38	20.9	0	7.1	.6	10.4	.4
.40	22.7	0	7.1	.6	10.2	[illegible]
.44	27.7	.1	7.9	.8	11.0	[illegible]
.48	31.0	.3	9.2	.5	12.8	[illegible]
.52	35.4	.3	11.1	.5	15.1	.6
.56	39.4	.3	12.8	.6	16.9	.5
.60	42.8	.4	14.9	.4	19.2	.7
.64	46.5	.4	16.8	.4	21.1	.9
.68	48.9	.4	19.8	.5	23.4	.9
.72	52.2	.8	22.0	.5	26.3	1.6
.78	57.0	1.4	26.0	.9	30.5	1.8
.84	61.5	2.1	30.5	1.5	34.5	2.1
.90	64.8	2.8	34.6	2.0	38.5	3.0
.96	67.3	3.2	37.8	2.2	42.6	4.1
1.02	69.8	4.4	41.0	3.5	46.0	5.4
1.08	72.1	5.3	44.2	4.6	49.6	8.5
1.14	73.9	6.7	47.2	5.8	51.9	7.4
1.20	74.4	8.0	49.5	7.0	54.5	8.4
1.26	76.0	8.0	52.3	8.3	57.0	9.9
1.32	78.1	9.8	54.1	9.0	58.8	10.5
1.36	77.5	10.2	55.4	9.5	59.1	10.8
1.38	77.3	9.9	55.4	9.5	58.1	10.3
1.40	75.6	9.4	54.0	9.0	55.0	9.1
1.42	69.8	8.0	48.5	8.0	50.6	8.7
1.44	68.2	8.0	44.5	7.7	49.3	8.2
1.46	67.3	8.0	43.6	7.9	49.2	8.5
1.48	68.2	8.0	44.0	8.3	51.5	8.6
1.50	70.0	9.9	47.1	9.0	54.7	10.0
1.54	75.8	12.0	52.1	11.0	59.0	11.5
1.58	78.8	13.0	56.9	12.8	62.4	13.0
1.62	80.1	13.9	59.1	13.5	64.5	14.0
1.66	81.0	14.7	61.5	15.0	65.9	15.0
1.70	81.4	15.8	62.4	16.0	66.2	15.5
1.74	81.0	15.9	62.6	16.6	66.2	15.9
1.78	79.9	15.9	62.4	16.9	66.3	16.2
1.82	80.3	16.4	62.7	17.3	67.1	17.0
1.84	80.0	16.8	63.0	17.8	67.0	16.5
1.86	79.3	15.9	62.6	17.7	65.7	15.5
1.88	76.2	12.2	60.6	16.4	55.4	10.1
1.90	66.2	5.6	41.0	8.7	37.0	6.5
1.92	45.2	3.0	23.1	4.0	27.0	5.0
1.94	40.9	3.4	19.3	3.9	26.5	5.5
1.96	43.0	4.6	20.7	3.7	30.0	6.6
1.98	47.4	6.2	25.0	6.1	35.2	8.0
2.00	51.7	8.0	30.4	8.1	39.8	8.4

Table A-3

RABBIT NO. 11, BLACK, LEFT EYE

Wavelength (μ)	Area					
	Temporal		Central		Nasal	
	Pigment Epithelium	Chorioid	Pigment Epithelium	Chorioid	Pigment Epithelium	Chorioid
0.34	18.3	1.7	54.6	2.6	16.3	2.4
.35	17.6	1.6	54.6	2.5	16.2	2.2
.36	16.9	1.5	55.0	2.4	16.1	1.8
.38	17.8	.6	57.4	1.6	16.1	1.0
.40	18.7	.2	57.9	1.2	16.3	.8
.44	20.5	0	61.9	1.2	18.3	.9
.48	24.0	0	64.7	1.2	21.8	1.0
.52	27.4	0	67.3	1.3	24.0	1.0
.56	31.0	0	69.9	1.7	27.2	.9
.60	33.9	.2	72.5	1.8	29.5	1.0
.64	36.5	.3	74.0	2.4	31.8	1.0
.68	39.8	1.0	75.4	2.4	34.3	1.1
.72	43.0	1.5	78.0	3.8	37.5	1.9
.78	47.7	3.5	80.5	5.0	41.5	2.8
.84	51.8	5.0	83.0	6.8	45.6	3.9
.90	55.2	7.0	84.0	9.6	49.2	5.0
.96	59.1	9.0	85.6	12.3	52.6	6.9
1.02	61.3	11.9	86.9	14.6	55.1	8.8
1.08	64.0	14.1	88.0	17.7	58.0	10.3
1.14	66.2	16.2	88.5	20.2	60.3	11.4
1.20	68.0	19.1	89.1	23.1	63.0	13.0
1.26	69.6	21.2	90.1	25.9	64.4	15.0
1.32	70.5	23.6	90.0	27.8	65.6	16.5
1.36	70.9	24.5	89.9	29.0	66.0	17.4
1.38	70.6	24.8	89.8	29.2	66.0	17.7
1.40	70.0	24.6	89.2	28.9	65.1	16.5
1.42	66.2	23.5	88.0	27.8	60.3	15.5
1.44	64.1	23.0	86.9	26.8	59.0	14.9
1.46	63.6	23.3	86.6	27.6	57.3	15.8
1.48	64.6	24.0	86.8	28.0	58.4	16.1
1.50	66.3	25.0	88.0	30.2	61.0	18.1
1.54	69.4	28.0	89.1	33.6	64.7	20.4
1.58	72.3	29.8	90.2	36.0	68.4	21.0
1.62	73.8	31.1	91.1	37.5	70.0	23.4
1.66	75.1	33.4	92.0	39.0	71.4	24.9
1.70	75.1	34.6	92.0	41.0	72.1	26.1
1.74	76.0	35.1	91.5	41.8	72.0	26.9
1.78	76.2	36.0	91.8	42.8	72.0	27.5
1.82	76.5	37.6	92.0	43.6	72.0	28.0
1.84	76.5	37.1	91.6	44.4	72.1	27.0
1.86	76.0	37.0	92.0	44.9	72.3	27.9
1.88	70.0	35.4	90.5	44.2	71.0	22.8
1.90	59.2	27.5	86.0	34.7	75.2	13.8
1.92	46.8	20.1	77.8	23.7	39.6	9.4
1.94	43.9	18.3	74.6	22.4	35.6	9.8
1.96	46.0	20.3	75.6	23.1	37.5	11.9
1.98	50.8	23.4	78.2	26.0	43.0	15.0
2.00	56.0	26.6	80.6	30.8	47.0	17.2

Table A-4

RABBIT NO. 12, BLACK & WHITE, LEFT EYE

Wavelength (μ)	Area					
			Central		Nasal	
	Pigment Epithelium	Chorioid	Pigment Epithelium	Chorioid	Pigment Epithelium	Chorioid
0.34	11.7	5.3	40.5	0	40.0	5.3
.35	10.8	4.3	40.5	0	40.0	[illegible]
.36	9.9	3.3	40.6	0	41.8	[illegible]
.38	9.5	2.6	41.5	0	43.7	[illegible]
.40	9.3	2.1	41.5	0	45.0	3.0
.44	10.7	1.2	43.0	0	47.1	2.0
.48	12.9	1.4	45.6	0	50.9	2.9
.52	14.8	1.9	48.0	0	53.8	3.5
.56	17.5	2.8	50.6	0	56.1	4.9
.60	20.0	3.1	53.9	0	58.5	6.1
.64	22.2	4.5	56.2	0	60.2	7.4
.68	25.0	6.0	58.2	0	62.5	11.0
.72	28.0	8.0	61.0	0	65.1	14.2
.78	32.2	11.7	65.1	0	67.3	19.5
.84	36.1	15.2	68.5	0	71.2	24.6
.90	39.9	19.0	72.3	0	73.9	29.6
.96	43.0	22.9	73.9	.1	75.5	34.4
1.02	46.0	26.0	75.7	.2	77.0	37.6
1.08	49.8	29.9	78.1	.7	79.0	41.7
1.14	52.0	32.5	78.8	1.0	79.7	44.3
1.20	54.3	35.2	80.2	1.1	81.2	47.7
1.26	56.3	38.0	89.9	1.3	82.8	50.8
1.32	58.3	40.4	81.5	1.3	83.0	53.0
1.36	58.8	42.0	82.0	1.3	83.1	53.9
1.38	58.4	42.2	82.0	1.4	82.5	54.0
1.40	57.7	42.0	80.6	1.3	82.0	53.7
1.42	53.0	40.6	78.2	1.5	80.2	51.5
1.44	51.1	39.2	77.7	1.5	79.1	49.9
1.46	50.5	39.1	77.7	1.5	78.9	49.6
1.48	51.1	39.7	78.5	1.5	79.3	50.3
1.50	53.4	41.1	79.8	1.3	80.6	52.2
1.54	57.7	44.7	81.3	1.8	82.3	55.7
1.58	61.1	47.8	82.7	2.1	83.7	58.5
1.62	62.9	49.2	83.9	3.0	84.0	60.0
1.66	64.5	50.9	84.2	3.2	84.9	61.5
1.70	65.4	52.3	84.9	3.7	85.1	62.5
1.74	65.2	53.0	85.0	4.0	85.4	63.0
1.78	65.3	53.8	85.0	4.0	85.7	63.5
1.82	65.8	54.5	85.4	4.0	85.8	64.0
1.84	65.4	54.8	84.6	4.0	85.6	[illegible]
1.86	65.0	55.1	84.6	4.1	85.5	[illegible]
1.88	63.0	54.9	79.0	3.2	85.6	64.6
1.90	49.0	47.5	73.0	.6	78.0	50.5
1.92	34.5	36.0	64.9	.1	67.4	[illegible]
1.94	29.8	30.9	63.0	0	66.2	38.1
1.96	31.9	31.9	65.2	0	67.6	38.1
1.98	36.0	35.7	68.4	.4	70.3	[illegible]
2.00	41.0	39.3	71.8	.5	73.8	45.8

Table A-5

RABBIT NO. 13, WILD COLOR, RIGHT EYE

Wavelength (μ)	Area					
	Temporal		Central		Nasal	
	Pigment Epithelium	Chorioid	Pigment Epithelium	Chorioid	Pigment Epithelium	Chorioid
0.34	17.3	3.7	27.0	2.6	28.0	2.0
.35	17.3	2.8	27.0	2.3	28.0	2.0
.36	17.3	1.9	27.4	2.0	28.5	2.0
.38	18.0	1.0	28.4	1.2	29.3	1.1
.40	17.9	.6	29.3	1.0	29.8	.8
.44	19.5	.4	32.3	.6	31.7	.4
.48	22.4	.2	35.7	.8	35.0	.8
.52	25.3	.2	38.8	.5	37.5	.5
.56	29.0	.2	41.9	.3	40.5	.6
.60	31.2	0	44.1	.5	43.0	.9
.64	33.9	0	46.9	.9	45.4	1.0
.68	37.0	.1	49.3	1.1	48.4	1.2
.72	40.2	.6	52.3	1.5	51.1	2.1
.78	45.0	1.2	56.5	2.0	56.1	3.6
.84	50.3	3.1	59.9	3.5	59.6	5.6
.90	53.9	5.4	62.5	4.8	63.1	8.2
.96	58.0	7.7	65.1	6.6	66.0	10.5
1.02	59.5	10.0	67.0	8.5	68.1	12.3
1.08	62.5	13.3	70.1	10.8	69.9	14.8
1.14	65.4	16.0	71.8	12.4	71.8	17.8
1.20	67.0	19.0	72.5	14.6	73.7	19.4
1.26	70.9	22.5	74.5	16.9	75.3	22.1
1.32	71.4	24.9	75.1	18.3	76.8	24.9
1.36	72.0	27.0	75.5	19.2	76.8	26.6
1.38	71.8	27.1	75.4	19.5	76.7	26.2
1.40	70.0	26.9	74.3	20.0	76.1	26.3
1.42	65.0	25.4	70.8	19.7	72.2	25.3
1.44	63.6	25.0	69.0	19.0	70.5	23.8
1.46	63.0	25.4	68.3	18.9	70.1	23.0
1.48	64.2	26.0	68.2	18.9	70.6	24.0
1.50	66.5	27.5	70.0	19.9	72.1	26.0
1.54	69.9	30.6	73.2	22.2	75.7	28.1
1.58	73.0	33.4	75.9	24.6	78.2	31.1
1.62	75.0	34.6	77.5	26.2	79.0	32.8
1.66	76.4	36.7	78.5	28.0	80.1	35.2
1.70	77.0	38.0	79.7	29.1	80.9	36.6
1.74	78.2	39.0	79.0	30.0	81.0	37.1
1.78	77.2	39.5	79.8	30.9	81.0	38.1
1.82	76.8	40.0	79.5	31.6	80.9	38.5
1.84	77.0	41.0	79.2	32.1	81.0	39.4
1.86	77.0	41.0	79.0	32.1	80.8	39.5
1.88	76.8	40.8	78.0	31.8	79.9	38.9
1.90	61.0	34.0	68.0	23.9	69.5	31.5
1.92	44.0	23.0	53.0	15.9	55.9	19.5
1.94	40.2	20.0	48.3	14.2	51.9	18.9
1.96	42.0	20.6	50.0	14.6	53.0	19.1
1.98	46.8	24.3	54.0	16.9	57.1	19.5
2.00	52.9	27.3	58.5	19.4	61.1	21.9

Table A-6

RABBIT NO. 13, WILD COLOR, LEFT EYE

Wavelength (μ)	Area					
	Temporal		Central		Nasal	
	Pigment Epithelium	Chorioid	Pigment Epithelium	Chorioid	Pigment Epithelium	Chorioid
0.34	14.0	3.8	8.7	0.5	22.0	2.9
.35	14.0	3.2	7.9	.5	22.0	2.5
.36	14.0	2.6	7.1	.5	22.0	2.1
.38	15.1	1.7	6.5	.6	23.2	1.7
.40	15.1	.9	6.2	.6	24.4	1.2
.44	15.5	.4	6.5	.6	28.0	1.0
.48	17.6	.4	7.3	.6	31.5	.9
.52	20.0	.6	8.5	.7	34.8	.9
.56	22.4	1.0	10.0	.6	38.0	.9
.60	24.4	1.0	12.1	.2	41.1	1.0
.64	27.0	1.5	13.2	.5	44.0	1.1
.68	29.4	2.7	15.4	.8	46.7	1.5
.72	32.5	4.6	17.3	.8	48.9	2.3
.78	36.9	7.2	20.7	1.0	53.9	4.0
.84	40.9	10.9	24.1	1.2	57.8	6.3
.90	44.9	15.0	27.5	1.1	60.9	9.5
.96	48.6	18.6	31.0	1.2	64.8	11.5
1.02	51.5	22.0	34.7	1.9	67.0	13.9
1.08	54.5	26.1	38.0	2.2	68.9	16.8
1.14	56.8	29.4	40.5	2.4	70.6	18.6
1.20	59.3	33.0	43.5	3.0	72.6	21.2
1.26	61.0	35.8	45.9	3.3	74.0	23.9
1.32	62.8	38.1	48.1	3.7	75.9	26.0
1.36	63.2	39.6	49.0	4.0	76.2	27.5
1.38	62.6	39.4	48.8	4.0	76.0	27.8
1.40	61.0	38.3	46.7	3.9	74.1	27.3
1.42	56.2	36.1	41.8	3.4	70.3	25.2
1.44	55.1	35.9	40.0	3.2	69.3	24.8
1.46	54.6	36.2	39.5	3.3	69.2	24.8
1.48	55.3	37.3	40.3	3.5	70.3	25.3
1.50	58.2	39.4	43.4	4.0	72.2	27.0
1.54	62.1	42.5	47.8	4.6	74.6	30.0
1.58	65.2	45.3	51.9	4.9	77.0	32.7
1.62	66.7	47.1	53.8	5.3	77.7	34.1
1.66	68.1	49.0	55.4	5.9	79.0	35.8
1.70	68.9	50.0	57.0	6.3	79.8	37.0
1.74	69.0	51.0	57.4	6.7	79.9	37.8
1.78	69.3	51.0	57.4	6.7	79.7	38.0
1.82	70.1	52.3	58.0	7.0	79.3	38.9
1.84	70.0	52.4	58.0	6.9	79.4	39.1
1.86	69.3	51.8	58.3	7.1	79.0	39.0
1.88	66.5	45.9	53.0	6.8	73.5	37.5
1.90	48.5	31.2	35.0	3.0	63.9	26.9
1.92	36.1	25.9	21.0	2.0	53.0	17.8
1.94	33.1	25.4	18.0	2.0	50.8	16.2
1.96	35.6	28.9	19.2	1.9	52.4	16.7
1.98	39.8	32.1	24.3	2.0	57.3	20.4
2.00	44.2	36.8	30.3	2.1	61.9	24.2

Table A-7

H-1

Wavelength (μ)	Area					
	Temporal		Central		Nasal	
	Pigment Epithelium	Chorioid	Pigment Epithelium	Chorioid	Pigment Epithelium	Chorioid
0.34	7.1	7.7	7.9	6.1	7.8	5.8
.35	5.9	6.4	6.9	5.0	7.1	4.6
.36	5.1	5.1	6.2	3.9	6.6	[illegible]
.38	4.9	3.7	5.5	2.4	6.7	2.6
.40	4.7	2.8	5.4	1.5	6.2	1.8
.44	5.0	2.5	6.0	1.3	6.6	1.4
.48	6.0	3.5	7.1	1.6	7.2	1.6
.52	7.0	4.1	8.4	2.0	8.0	1.8
.56	7.8	6.1	9.8	2.9	8.8	2.1
.60	8.8	8.0	11.5	3.9	9.8	3.0
.64	9.9	10.5	12.7	4.9	10.5	3.8
.68	11.0	13.0	14.3	7.0	11.9	5.0
.72	12.1	16.0	16.1	9.0	13.4	7.0
.78	14.1	20.2	18.6	12.5	15.5	9.4
.84	16.2	24.1	21.0	5.9	18.0	12.6
.90	18.8	28.6	24.3	19.5	21.0	15.9
.96	21.0	32.1	26.7	22.6	23.4	18.9
1.02	22.5	35.4	29.2	25.8	25.9	21.6
1.08	25.0	39.0	32.1	29.3	28.9	25.0
1.14	27.0	41.7	34.4	32.0	31.1	27.9
1.20	28.9	44.3	36.5	35.0	34.0	31.2
1.26	30.9	47.0	39.2	37.9	36.4	34.3
1.32	32.7	49.0	40.1	39.9	38.4	36.6
1.36	33.1	50.0	40.1	40.2	38.5	37.4
1.38	33.4	49.8	37.5	39.9	37.8	37.5
1.40	31.5	48.5	30.9	38.4	35.5	37.1
1.42	26.7	44.8	26.1	36.3	29.9	34.5
1.44	24.2	43.2	25.0	35.9	29.0	34.3
1.46	23.4	43.0	25.0	35.9	28.9	34.6
1.48	23.9	44.2	27.4	37.3	30.5	36.1
1.50	26.3	47.0	31.5	39.6	33.6	37.8
1.54	31.0	50.3	37.7	43.1	38.4	40.9
1.58	35.9	54.0	42.4	46.0	42.2	44.0
1.62	37.8	56.0	44.8	47.4	44.5	45.6
1.66	39.9	57.6	46.8	48.9	46.4	47.4
1.70	41.3	58.8	47.6	50.3	47.6	48.7
1.74	41.6	58.9	47.3	50.9	47.9	49.4
1.78	41.5	58.9	46.9	51.3	47.9	50.1
1.82	41.3	59.3	46.5	51.5	48.1	50.8
1.84	42.0	59.4	46.1	51.4	47.9	50.9
1.86	41.6	59.1	44.1	51.0	46.9	50.4
1.88	40.1	58.0	32.5	47.0	37.3	47.0
1.90	26.0	43.5	9.7	30.5	21.0	35.9
1.92	11.0	29.2	5.0	23.2	11.0	25.9
1.94	7.0	25.0	4.4	21.8	9.5	24.0
1.96	7.1	27.1	6.0	24.3	11.2	26.4
1.98	9.3	31.2	9.1	29.0	15.4	30.4
2.00	12.9	36.1	12.8	33.0	20.0	34.4

Table A-8

H-2

Wavelength (μ)	Area					
	Temporal		Central		Nasal	
	Pigment Epithelium	Choricid	Pigment Epithelium	Choricid	Pigment Epithelium	Choricid
0.34	64.6	7.3	29.7	4.8	5.0	7.9
.35	63.6	1.1	29.1	3.9	3.9	[illegible]
.36	62.9	.9	28.7	3.0	3.2	[illegible]
.38	62.0	.4	27.0	1.8	2.4	[illegible]
.40	60.9	.4	27.3	1.4	2.0	2.9
.44	59.5	.3	27.0	.6	1.9	2.6
.48	59.8	.3	27.9	.7	3.0	3.8
.52	60.5	.2	28.2	.7	3.4	4.8
.56	61.6	.0	29.4	.9	3.9	6.5
.60	62.4	.1	30.7	1.8	4.8	9.0
.64	63.2	.3	32.3	2.5	5.7	11.0
.68	64.0	.6	33.9	3.7	6.6	14.0
.72	64.9	.9	35.1	5.1	7.6	16.9
.78	66.2	1.4	37.9	8.0	9.3	21.2
.84	67.5	2.3	39.9	11.0	11.7	25.6
.90	69.3	3.1	42.7	14.7	13.3	15.0
.96	70.6	4.1	45.4	18.1	15.5	33.8
1.02	71.7	5.2	47.4	21.0	17.6	36.9
1.08	72.5	6.6	49.5	25.1	20.3	40.5
1.14	73.5	7.7	51.0	28.0	22.1	43.0
1.20	74.2	9.2	53.0	31.2	24.3	46.1
1.26	74.5	10.6	54.6	34.0	26.5	48.3
1.32	75.0	11.8	55.9	36.4	28.4	50.2
1.36	75.1	12.1	56.1	37.6	28.9	51.1
1.38	75.3	12.1	56.2	37.8	28.4	51.1
1.40	75.4	11.1	56.3	37.4	27.0	50.9
1.42	75.5	9.1	56.3	34.0	21.1	47.0
1.44	75.2	8.9	56.4	32.2	19.2	45.9
1.46	75.1	8.8	56.6	31.9	19.0	45.6
1.48	75.0	9.0	57.0	32.5	20.1	46.5
1.50	75.2	10.1	58.0	35.2	22.6	48.4
1.54	75.5	12.8	59.0	39.0	27.1	52.0
1.58	75.7	14.8	60.4	42.6	31.2	54.9
1.62	75.5	16.0	60.8	44.1	33.6	56.8
1.66	75.6	16.9	61.5	46.6	35.0	58.0
1.70	75.6	17.8	62.6	47.9	36.2	59.0
1.74	76.0	18.0	62.8	48.1	36.6	59.7
1.78	76.0	17.9	63.1	48.6	36.1	59.6
1.82	75.7	18.0	63.9	49.1	36.8	60.0
1.84	75.9	18.1	64.0	49.5	36.6	60.0
1.86	76.0	18.0	63.9	49.4	36.0	59.9
1.88	76.0	16.0	63.4	49.0	32.0	59.3
1.90	75.4	12.8	62.3	38.0	17.0	48.0
1.92	74.4	3.4	58.7	[illegible]	6.6	[illegible]
1.94	73.9	2.2	56.6	17.1	4.1	29.8
1.96	75.0	2.5	57.1	17.1	4.8	31.1
1.98	76.1	3.7	58.9	[illegible]	7.3	[illegible]
2.00	77.1	5.3	60.2	26.0	10.4	40.0

Table A-9

H-3

Wavelength (μ)	Area					
	Temporal		Central		Nasal	
	Pigment Epithelium	Choriod	Pigment Epithelium	Choriod	Pigment Epithelium	Choriod
0.34	65.9	3.3	53.4	1.6	51.9	5.4
.35	63.0	2.7	53.4	1.3	50.7	4.5
.36	61.1	2.1	53.7	1.0	49.9	3.6
.38	60.0	1.3	52.2	.4	48.5	2.2
.40	59.5	1.0	50.8	.2	48.0	2.0
.44	61.8	.5	51.5	.1	48.1	1.3
.48	62.9	.4	52.4	.2	48.6	2.2
.52	63.9	.5	53.8	.2	50.1	2.7
.56	65.6	.6	54.6	.2	50.8	3.1
.60	68.0	.9	55.2	.3	52.0	4.7
.64	69.3	1.6	55.7	.8	53.1	6.0
.68	50.9	2.1	57.8	1.0	54.1	7.5
.72	73.0	3.3	59.3	1.6	55.9	9.2
.78	75.4	5.2	61.9	2.6	57.9	12.0
.84	77.7	7.0	64.3	3.5	59.8	14.4
.90	80.2	9.1	67.1	4.8	62.1	17.3
.96	82.2	11.5	69.4	6.0	64.5	20.5
1.02	84.0	13.1	71.0	7.0	65.9	22.5
1.08	84.8	15.7	72.7	8.8	68.2	25.5
1.14	85.7	17.5	74.4	9.8	69.9	27.6
1.20	86.6	19.7	76.5	11.0	71.4	30.0
1.26	87.0	21.8	77.5	12.1	72.5	32.3
1.32	87.3	23.8	78.9	13.3	73.9	34.0
1.36	87.6	24.8	79.6	14.0	74.1	35.0
1.38	87.7	24.9	79.3	13.8	74.4	35.0
1.40	87.9	24.1	79.0	12.6	74.3	34.1
1.42	87.5	21.6	77.2	10.3	74.3	30.4
1.44	87.4	21.0	77.0	9.6	74.6	29.4
1.46	87.4	21.6	77.4	9.8	74.7	29.3
1.48	87.1	22.7	77.9	10.4	75.3	30.2
1.50	87.6	24.6	78.6	11.8	75.4	32.4
1.54	89.0	27.2	80.0	14.0	76.2	35.9
1.58	89.8	29.7	81.2	16.0	77.1	38.9
1.62	89.6	30.9	81.6	17.1	77.4	40.1
1.66	90.0	32.2	82.0	18.2	78.0	41.6
1.70	89.9	33.4	82.7	18.9	78.4	42.7
1.74	91.0	34.0	82.9	19.2	78.9	43.1
1.78	92.0	34.4	82.8	19.1	79.0	43.3
1.82	92.9	35.0	83.1	19.6	79.4	43.9
1.84	92.8	35.0	83.1	19.5	79.5	44.2
1.86	92.0	34.8	83.0	19.3	79.3	44.0
1.88	90.5	32.0	81.2	16.5	79.0	42.5
1.90	88.7	21.0	78.7	8.4	78.1	29.7
1.92	87.0	13.1	70.6	3.8	76.0	18.6
1.94	86.1	12.1	68.0	2.9	75.7	16.1
1.96	87.1	14.0	71.0	3.7	76.5	17.4
1.98	88.1	17.2	74.0	5.2	77.6	21.2
2.00	89.4	20.1	76.0	7.0	78.1	25.0

Table A-10

H-4

Wavelength (μ)	Area					
	Temporal		Central		Nasal	
	Pigment Epithelium	Chorioid	Pigment Epithelium	Chorioid	Pigment Epithelium	Chorioid
0.34	63.3	3.7	73.8	2.5	63.6	3.7
.35	62.2	3.3	72.6	2.2	61.5	3.2
.36	62.1	2.9	71.8	1.9	60.1	2.7
.38	61.7	2.2	70.5	1.2	59.5	1.9
.40	60.6	1.8	69.9	1.0	60.2	1.6
.44	62.0	1.8	71.6	.5	62.0	1.[illegible]
.48	64.0	2.6	73.2	1.1	64.6	2.2
.52	65.1	3.1	74.8	1.4	65.8	2.6
.56	66.8	3.7	75.7	1.5	67.3	3.3
.60	68.3	5.0	76.8	2.3	69.0	4.5
.64	89.7	6.0	78.0	2.8	70.5	5.6
.68	70.6	7.2	79.1	3.7	72.2	6.9
.72	72.0	8.5	80.2	4.3	73.8	8.1
.78	74.0	11.0	82.6	6.1	76.1	10.6
.84	76.1	13.0	84.6	8.0	78.3	12.7
.90	78.0	15.1	86.1	9.5	79.8	14.8
.96	79.8	17.6	87.9	11.4	81.3	17.0
1.02	81.4	19.3	89.1	13.0	82.7	18.7
1.08	82.3	21.0	90.5	15.0	83.9	20.7
1.14	82.8	23.0	90.8	16.5	84.2	22.2
1.20	83.9	24.9	91.6	18.2	85.0	24.0
1.26	84.2	26.3	92.1	20.0	85.8	26.1
1.32	85.4	27.7	92.2	21.1	86.3	27.4
1.36	85.8	28.5	92.3	21.6	86.8	28.3
1.38	85.5	28.5	92.5	21.5	86.7	28.0
1.40	85.0	28.0	92.7	21.3	86.4	27.2
1.42	83.8	25.4	92.6	19.1	86.3	24.6
1.44	83.5	24.7	92.5	18.3	86.0	24.1
1.46	83.6	24.4	92.6	18.7	85.9	24.3
1.48	84.1	24.9	92.3	19.2	86.2	25.3
1.50	84.4	26.3	92.8	20.4	86.5	27.0
1.54	85.4	29.1	92.8	22.9	87.1	29.6
1.58	86.8	31.0	92.8	24.7	87.9	31.5
1.62	87.1	32.2	93.5	25.6	88.2	32.2
1.66	87.6	33.1	94.0	26.7	88.1	33.3
1.70	88.0	33.9	94.6	27.3	88.6	34.0
1.74	88.0	34.0	94.7	27.6	88.8	34.2
1.78	87.8	34.0	94.7	27.9	89.1	34.4
1.82	88.7	34.3	94.8	28.3	89.8	35.1
1.84	88.4	34.3	94.4	28.3	89.6	35.1
1.86	87.9	34.2	94.0	28.0	89.3	34.7
1.88	86.6	33.5	93.3	27.6	88.5	30.7
1.90	84.0	24.8	92.0	19.0	86.2	20.2
1.92	79.9	17.0	91.1	11.0	84.1	14.6
1.94	77.3	14.3	90.5	9.4	84.0	14.2
1.96	78.1	15.3	91.2	10.4	85.0	16.0
1.98	80.2	17.9	92.3	12.3	86.3	19.1
2.00	82.4	20.2	93.1	15.2	87.7	22.6

Table A-11

H-5

Wavelength (μ)	Area					
	Temporal		Central		Nasal	
	Pigment Epithelium	Chorioid	Pigment Epithelium	Chorioid	Pigment Epithelium	Chorioid
0.34	48.7	2.8	60.6	4.8	54.7	2.4
.35	48.7	2.4	60.6	4.1	53.2	1.9
.36	48.6	2.0	60.9	3.4	52.1	1.4
.38	48.8	1.3	61.5	2.3	51.8	.5
.40	48.1	1.0	61.4	2.0	52.0	.5
.44	49.5	.6	61.5	2.0	53.4	.4
.48	51.2	1.0	63.4	2.7	56.0	.5
.52	53.9	1.0	64.9	3.3	58.6	.6
.56	54.5	1.1	67.3	4.0	61.1	.8
.60	56.4	1.4	68.8	5.0	64.0	1.1
.64	58.3	2.0	70.0	6.1	66.4	1.7
.68	60.0	2.9	71.1	7.5	68.4	2.5
.72	61.9	3.8	72.3	8.9	70.8	3.1
.78	64.5	5.2	72.9	11.2	73.8	4.0
.84	67.3	6.8	75.1	13.3	76.6	5.3
.90	68.8	8.4	76.9	16.0	79.8	7.0
.96	70.4	10.0	78.0	18.0	80.4	8.4
1.02	72.6	11.8	78.8	20.3	81.4	10.0
1.08	73.9	13.7	80.1	22.3	82.5	11.3
1.14	75.0	15.1	81.0	24.3	83.6	12.9
1.20	76.1	16.7	81.8	26.1	84.2	14.4
1.26	77.5	18.1	82.9	28.1	85.0	16.0
1.32	78.0	18.2	83.2	29.5	85.0	16.9
1.36	78.5	19.8	83.6	30.5	85.2	17.6
1.38	78.7	20.1	83.4	30.5	85.2	17.5
1.40	78.4	19.5	83.0	29.8	84.3	17.0
1.42	77.9	17.7	82.0	27.4	84.0	15.8
1.44	77.0	17.0	81.1	27.0	83.9	15.3
1.46	77.1	16.9	81.1	26.9	83.8	15.5
1.48	77.8	17.4	81.8	27.7	84.0	16.0
1.50	78.1	18.6	82.8	29.4	84.8	17.1
1.54	79.5	21.1	84.3	31.7	85.8	19.2
1.58	80.7	23.1	85.2	33.9	87.0	20.5
1.62	81.1	24.2	85.7	34.9	87.0	21.8
1.66	81.8	25.2	86.1	36.2	88.0	22.8
1.70	82.1	26.2	86.2	37.0	88.8	23.8
1.74	82.5	27.7	86.4	37.3	89.0	24.0
1.78	82.7	26.9	86.6	37.6	89.2	24.4
1.82	83.4	27.5	87.1	38.0	90.0	25.0
1.84	83.4	27.7	87.0	38.0	90.0	25.0
1.86	83.1	27.4	86.4	37.9	89.2	24.7
1.88	82.1	27.0	84.5	37.1	87.9	22.0
1.90	79.9	19.0	81.0	27.0	84.8	14.5
1.92	74.7	15.8	75.2	18.7	81.9	10.1
1.94	71.4	8.6	72.8	16.8	80.1	19.4
1.96	72.9	9.0	73.9	17.9	81.0	10.9
1.98	75.1	11.4	76.3	21.0	82.8	13.0
2.00	77.0	14.4	78.4	24.1	84.2	15.6

Table A-12

H-6

Wavelength (μ)	Area					
	Temporal		Central		Nasal	
	Pigment Epithelium	Chorioid	Pigment Epithelium	Chorioid	Pigment Epithelium	Chorioid
0.34						
.35	26.1	2.2	23.0	3.4	13.8	4.0
.36	25.3	1.6	21.0	2.8	13.1	3.1
.38	24.2	1.1	19.3	1.8	12.4	2.2
.40	23.9	.9	18.0	1.2	11.3	1.9
.44	24.4	.5	16.0	1.2	10.1	1.6
.48	26.1	.6	16.3	1.1	10.0	1.9
.52	27.6	.5	16.8	1.5	9.9	2.0
.56	29.2	.3	18.0	2.0	10.2	2.2
.60	31.3	.6	18.9	2.2	10.9	2.8
.64	32.9	.8	20.0	2.9	11.8	3.4
.68	35.0	1.2	21.6	3.9	12.9	4.2
.72	36.9	2.0	23.1	5.1	14.4	5.2
.78	39.4	2.8	26.0	7.0	16.9	7.1
.84	42.7	4.0	28.8	9.2	19.9	8.9
.90	45.1	5.6	31.8	11.9	22.9	11.1
.96	47.1	7.1	34.9	14.0	26.0	13.2
1.02	49.2	8.7	37.9	16.9	29.6	15.4
1.08	51.6	10.1	40.5	19.0	33.1	17.8
1.14	54.0	12.0	43.0	21.1	36.0	19.8
1.20	56.1	13.9	46.1	23.7	39.7	22.1
1.26	57.9	15.2	48.4	25.9	42.5	24.0
1.32	59.5	17.0	50.9	27.7	45.1	26.0
1.36	60.2	17.9	52.2	28.9	46.9	27.0
1.38	60.2	17.7	52.8	28.9	47.3	27.2
1.40	60.0	17.0	53.0	28.7	47.7	26.5
1.42	59.4	16.1	53.0	28.9	47.6	25.1
1.44	59.1	15.9	52.9	26.0	48.0	25.1
1.46	59.2	16.0	53.4	25.7	49.0	25.5
1.48	59.7	16.8	53.8	26.2	50.0	26.8
1.50	60.6	18.1	54.9	28.2	51.0	28.0
1.54	62.0	20.3	56.9	31.0	53.1	30.8
1.58	63.9	22.3	58.8	33.9	55.3	33.0
1.62	64.8	23.5	60.0	35.2	56.8	34.2
1.66	65.5	24.6	61.3	36.9	58.0	35.9
1.70	66.4	25.8	62.8	37.8	59.6	36.9
1.74	67.0	26.2	63.6	38.5	60.6	37.7
1.78	67.5	26.8	64.4	39.0	61.5	38.1
1.82	68.1	28.0	65.8	40.0	62.5	39.0
1.84	68.1	28.0	66.0	40.2	62.7	39.1
1.86	68.0	27.6	66.0	40.1	62.4	38.8
1.88	66.9	25.0	65.4	39.5	62.6	35.2
1.90	64.5	18.0	63.1	32.1	60.2	27.0
1.92	61.0	11.8	59.6	21.4	56.1	20.8
1.94	56.9	11.0	56.7	17.1	55.2	20.0
1.96	57.3	12.3	57.0	17.6	56.9	22.1
1.98	60.0	15.1	59.1	21.0	59.0	25.4
2.00	11.7	17.6	61.2	24.0	60.8	28.5

Table A-13

H-7

Wavelength (μ)	Area					
	Temporal		Central		Nasal	
	Pigment Epithelium	Chorioid	Pigment Epithelium	Chorioid	Pigment Epithelium	Chorioid
0.34	17.3	4.3	30.4	4.2	12.0	6.9
.35	15.3	3.1	28.9	3.2	10.5	5.3
.36	14.5	2.2	27.1	2.5	9.9	4.0
.38	13.8	1.7	25.0	1.9	9.0	3.0
.40	13.5	1.0	23.7	1.2	8.4	2.4
.44	13.1	.9	22.5	.9	7.7	2.0
.48	14.4	1.2	23.2	1.4	8.1	2.3
.52	16.0	1.4	24.0	1.3	8.5	2.8
.56	18.0	1.5	25.5	1.9	9.0	3.4
.60	20.4	2.2	26.8	2.3	9.8	4.4
.64	23.0	3.0	28.2	3.2	10.5	5.8
.68	26.0	3.9	30.1	4.1	11.7	7.3
.72	29.3	4.8	32.1	5.6	12.8	9.0
.78	34.4	6.8	35.3	7.5	14.8	12.1
.84	39.4	8.8	38.4	9.7	17.2	15.5
.90	44.7	11.1	41.5	12.1	20.1	19.1
.96	49.0	13.4	45.0	14.5	22.8	22.7
1.02	53.1	15.6	47.8	16.9	25.3	26.0
1.08	57.2	18.0	50.9	19.0	29.0	29.5
1.14	60.5	19.9	53.3	21.1	31.9	32.6
1.20	64.0	22.0	56.1	23.8	35.4	35.9
1.26	66.0	23.9	58.4	25.9	38.7	38.7
1.32	69.0	25.6	60.4	27.9	40.9	40.7
1.36	70.1	26.9	61.9	29.2	43.1	42.1
1.38	70.2	27.0	62.1	29.5	43.4	42.0
1.40	70.1	26.2	62.2	29.4	43.5	41.3
1.42	70.5	25.0	62.0	28.4	43.7	40.0
1.44	71.2	24.0	62.1	27.7	44.0	39.7
1.46	72.0	24.0	62.5	27.9	45.0	40.1
1.48	72.2	25.0	63.4	28.4	45.9	41.0
1.50	73.2	26.6	64.1	30.0	46.9	43.0
1.54	74.3	29.0	65.9	32.5	49.1	45.8
1.58	76.2	31.2	67.4	34.7	51.0	48.0
1.62	76.5	32.7	68.4	35.9	52.6	49.3
1.66	77.1	34.1	69.7	37.5	54.0	51.0
1.70	78.3	35.2	70.2	38.8	55.5	52.2
1.74	78.9	36.0	71.2	39.4	56.9	53.2
1.78	80.0	36.4	71.9	40.0	57.9	53.8
1.82	81.2	37.9	72.9	41.0	59.4	54.9
1.84	81.3	38.0	73.0	41.1	59.9	54.9
1.86	80.4	38.0	72.6	41.0	59.9	54.7
1.88	79.2	37.2	71.6	40.6	59.1	54.0
1.90	78.0	28.5	70.0	34.5	57.9	46.0
1.92	77.0	18.9	67.0	25.9	53.9	35.9
1.94	77.0	16.7	64.4	22.6	57.9	33.4
1.96	78.1	18.0	65.3	23.4	53.1	35.1
1.98	79.8	21.4	67.4	26.8	55.4	39.1
2.00	81.0	24.3	69.1	30.0	57.5	42.6

Table A-14

H-8

Wavelength (μ)	Area					
	Temporal		Central		Nasal	
	Pigment Epithelium	Chorioid	Pigment Epithelium	Chorioid	Pigment Epithelium	Chorioid
0.34						
.35	20.2	1.9	25.8	1.6	15.0	1.5
.36	19.8	1.3	24.5	1.2	14.3	1.1
.38	19.9	1.0	23.1	.8	13.9	.8
.40	19.3	.8	22.2	.6	13.8	.4
.44	19.4	.7	22.2	.7	13.7	.4
.48	21.1	.7	25.3	.8	14.2	.5
.52	22.1	.4	27.5	.5	14.8	.3
.56	24.2	.3	30.2	.3	15.8	0
.60	26.9	.1	33.6	.6	17.0	0
.64	29.2	.2	36.7	.7	18.1	0
.68	32.1	.6	40.2	1.0	20.3	0
.72	35.4	.8	43.8	1.3	22.8	.1
.78	40.0	1.6	49.2	2.2	26.9	.4
.84	44.4	2.4	54.3	3.0	31.2	1.0
.90	49.3	3.4	58.3	4.0	36.2	1.3
.96	53.4	4.8	62.6	5.7	40.1	2.2
1.02	56.5	5.8	65.9	7.0	44.5	3.2
1.08	60.0	7.7	68.9	8.5	48.0	4.5
1.14	62.2	9.3	71.0	10.0	51.9	6.0
1.20	65.2	11.1	73.9	11.6	55.4	7.9
1.26	67.4	13.0	75.7	13.4	58.2	9.4
1.32	69.7	14.2	77.4	14.8	60.6	10.7
1.36	70.0	15.3	78.4	15.6	62.5	11.9
1.38	70.0	15.5	78.5	15.6	62.8	12.0
1.40	70.2	15.4	78.4	15.0	62.9	11.9
1.42	70.4	15.0	78.5	14.5	63.2	11.6
1.44	70.7	15.1	78.8	14.2	64.0	11.7
1.46	71.0	15.2	79.5	14.6	65.0	12.0
1.48	71.9	16.0	80.0	15.2	65.9	12.8
1.50	73.0	16.9	80.9	16.2	66.6	13.9
1.54	73.9	18.6	81.7	18.0	67.8	15.7
1.58	74.8	20.1	82.8	19.5	68.9	17.3
1.62	75.9	21.0	83.1	20.4	69.9	18.8
1.66	76.5	22.2	83.9	21.7	71.7	19.9
1.70	77.4	23.5	84.8	22.5	72.0	21.0
1.74	78.1	24.1	85.1	22.9	72.5	21.9
1.78	78.6	24.8	85.6	23.6	73.7	23.0
1.82	79.0	25.8	86.8	24.7	74.6	24.3
1.84	78.7	26.0	86.8	24.9	74.4	24.5
1.86	77.9	26.0	86.2	24.9	74.0	24.6
1.88	77.0	24.9	85.3	23.3	73.1	24.0
1.90	75.9	20.0	83.9	17.6	71.5	18.0
1.92	74.0	15.2	82.0	11.1	70.5	13.6
1.94	74.4	14.1	81.7	11.3	70.0	12.4
1.96	75.8	15.8	82.4	12.1	71.1	13.5
1.98	77.0	17.6	84.0	14.7	72.7	16.0
2.00	78.0	19.8	84.9	18.0	73.6	18.0

NOTE: Pigment Epithelium Temp., Central and Nasal are 1/2 thickness

Table A-15

H-9

Wavelength (μ)	Area					
	Temporal		Central		Nasal	
	Pigment Epithelium	Choroid	Pigment Epithelium	Choroid	Pigment Epithelium	Choroid
0.34	59.3	2.1	36.1	3.3	64.6	2.7
.35	57.2	1.3	33.9	2.3	64.1	1.5
.36	56.0	1.0	31.8	1.9	64.1	1.1
.38	55.0	.7	29.0	1.1	63.0	.6
.40	54.1	.5	28.1	.8	61.6	.7
.44	54.3	.2	28.1	.4	61.0	.5
.48	56.2	.2	29.4	.8	62.0	.7
.52	57.9	.2	30.5	.7	63.3	.7
.56	60.4	.0	32.0	.7	65.4	.7
.60	62.8	.0	33.8	1.1	67.4	1.2
.64	64.1	.2	35.2	1.4	69.2	1.3
.68	66.0	.5	37.0	2.1	71.1	2.1
.72	68.4	.8	39.0	2.9	72.9	3.0
.78	70.8	1.8	41.8	3.9	75.2	4.0
.84	73.0	3.0	44.0	5.5	78.0	5.3
.90	75.8	4.2	46.9	7.0	80.0	6.8
.96	78.9	5.5	49.2	8.9	82.0	8.0
1.02	79.1	6.8	51.5	10.4	83.1	9.2
1.08	80.5	8.0	53.7	12.4	84.1	10.7
1.14	81.4	9.6	55.7	9.0	85.8	11.9
1.20	82.4	11.1	57.7	16.1	86.1	13.0
1.26	83.6	12.9	59.1	17.9	87.0	14.5
1.32	83.8	14.1	60.4	19.6	87.9	15.4
1.36	83.8	15.1	61.1	20.5	88.0	15.6
1.38	83.5	15.0	61.1	20.3	88.0	15.0
1.40	82.7	14.3	60.8	19.5	87.0	13.4
1.42	80.1	13.0	59.4	18.0	85.7	12.6
1.44	79.5	12.7	59.3	17.6	85.6	12.6
1.46	79.5	13.0	59.7	18.0	86.4	13.1
1.48	80.4	13.6	60.3	19.4	86.5	14.0
1.50	81.3	15.0	61.6	20.7	87.0	15.2
1.54	83.2	17.1	63.3	23.2	88.2	17.1
1.58	84.7	19.0	65.1	25.7	88.8	19.0
1.62	85.4	20.3	65.8	26.9	89.0	19.6
1.66	85.5	21.2	66.8	28.4	81.1	20.4
1.70	86.2	22.4	67.4	29.5	89.5	21.2
1.74	86.5	23.1	67.9	30.1	89.3	21.3
1.78	86.3	23.6	68.1	30.4	89.9	21.5
1.82	86.9	24.4	69.0	31.7	90.0	22.1
1.84	86.7	24.5	69.0	31.8	89.4	22.0
1.86	86.0	24.3	68.4	31.4	88.3	21.1
1.88	82.6	21.7	66.2	27.0	86.1	16.4
1.90	78.3	13.0	63.1	17.5	83.0	8.6
1.92	67.8	8.0	56.6	11.3	79.2	5.8
1.94	66.3	8.4	54.8	11.1	78.4	5.9
1.96	68.3	9.0	56.7	13.2	80.5	7.2
1.98	71.9	11.4	59.5	16.1	82.2	9.6
2.00	75.0	13.4	62.0	19.1	84.0	12.0

Table A-16

H-10

Wavelength (μ)	Area					
	Temporal		Central		Nasal	
	Pigment Epithelium	Chorioid	Pigment Epithelium	Chorioid	Pigment Epithelium	Chorioid
0.34	21.2	3.1	13.6	2.9	13.7	6.1
.35	20.0	2.4	11.8	1.9	12.2	4.4
.36	19.0	1.8	11.1	1.4	11.2	3.7
.38	18.0	1.1	10.6	.8	10.1	2.4
.40	8.0	.8	10.3	.7	9.6	1.7
.44	19.4	.5	10.9	.4	10.0	1.2
.48	21.6	.4	12.0	.2	11.2	1.4
.52	24.1	.2	13.2	.2	12.0	1.5
.56	27.0	.6	15.4	.3	13.3	2.0
.60	29.6	.9	17.1	.2	14.6	2.8
.64	32.2	1.1	18.7	.3	16.4	4.1
.68	35.1	2.1	20.8	.7	18.1	6.1
.72	38.0	2.9	23.0	1.5	20.3	7.8
.78	42.0	4.4	26.9	2.6	23.6	11.5
.84	45.8	6.5	30.4	4.0	27.0	15.3
.90	49.9	8.6	34.2	5.5	30.7	19.1
.96	53.9	10.9	38.0	7.4	34.5	23.0
1.02	56.5	12.7	40.6	9.0	37.3	26.3
1.08	60.0	15.0	43.8	11.1	40.8	30.0
1.14	62.1	17.2	46.0	13.1	43.5	33.1
1.20	64.2	19.8	49.1	15.2	46.3	37.5
1.26	66.4	21.7	51.8	17.3	49.2	39.1
1.32	68.0	23.7	54.0	19.0	51.4	41.6
1.36	68.6	25.0	55.6	20.0	52.6	42.4
1.38	68.5	24.8	55.5	20.0	53.1	42.2
1.40	67.4	24.0	55.2	19.1	52.8	40.1
1.42	66.3	22.0	54.2	17.1	52.6	38.7
1.44	66.4	21.1	54.1	16.7	53.2	38.3
1.46	67.0	21.1	54.8	16.9	54.9	39.0
1.48	68.0	22.0	55.8	17.6	55.1	40.1
1.50	69.1	24.0	57.2	19.4	56.8	42.7
1.54	70.9	27.1	59.3	22.3	58.5	45.8
1.58	72.8	29.8	61.1	24.8	60.3	48.2
1.62	73.6	31.3	62.4	26.3	61.0	49.4
1.66	74.9	32.9	63.8	28.0	62.0	51.0
1.70	76.0	34.1	65.1	29.2	63.6	52.1
1.74	76.0	34.6	65.8	29.9	64.3	52.6
1.78	76.2	35.1	66.4	30.2	65.1	52.9
1.82	76.7	36.0	67.4	31.0	66.2	53.9
1.84	76.7	36.1	67.8	31.1	66.0	53.9
1.86	76.1	35.9	67.6	31.0	65.0	53.1
1.88	73.1	34.5	65.5	30.1	63.4	51.1
1.90	65.9	23.2	62.0	18.4	54.9	34.1
1.92	60.0	14.2	54.7	10.8	57.3	27.0
1.94	60.0	12.5	53.0	8.9	57.8	27.6
1.96	62.9	14.0	54.9	10.0	60.3	30.2
1.98	66.0	17.2	57.9	12.8	62.0	34.9
2.00	68.8	20.8	60.4	16.0	63.8	39.2

NOTE: Area 5 (retinal pigment epithelium) is 1/2 thickness

DASA RETINAL BURN DISTRIBUTION LIST -- - 1962

	No. of Copies
New York Eye and Ear Infirmary 218 Second Avenue ATTN: Dr. Jerry H. Jacobson New York 3, New York.....	1 copy
Ohio State University, Research Foundation 1314 Uinnear Road ATTN: Dr. H. G. Bredemeyer..... Columbus 8, Ohio	1 copy
Commanding Officer Naval Medical Research Institute National Naval Medical Center ATTN: CAPT Henry Wagner, USN Bethesda 14, Maryland.....	1 copy
Commanding General Walter Reed Army Medical Center ATTN: Colonel Austin Lowry, MC, USA Washington 25, D. C.....	1 copy
USAFSAM Ophthamology Branch ATTN: Maj. James F. Culver, MC, USAF Brooks Air Force Base, Texas	
Medical College of Virginia Department of Biophysics & Biometry Box 877 Attn: Dr. W. T. Ham Richmond 19, Virginia.....	1 copy
Aerospace Medical Laboratories Air Force Systems Command Attn: ASBLPV Wright Patterson AFB, Ohio.....	1 copy
U. S. Navy Special Weapons Facility Attn: LCDR P. E. Beck, USN Kirtland AFB, New Mexico.....	1 copy

No. of Copies

Commander
U.S. Naval Material Laboratory
New York Naval Shipyard
Attn: Mr. W. Derksen
Brooklyn 1, New York..... 1 copy

Dr. Harry Hill
Aviation Medical Acceleration Laboratory
U.S. Navy Air Development Center
Johnsville, Pennsylvania..... 1 copy

Mr. David Feldman
U.S. Army Quartermaster Research and Engineering Center
Natick, Massachusetts..... 1 copy

Mr. Andrew Brittan
U.S. Army Frankford Arsenal
Philadelphia, Pennsylvania..... 1 copy

U.S. Army Ordnance Tank Automative Command
ORDMC-RRD-3
Detroit Arsenal
Centerline, Michigan..... 1 copy

Mr. Robert Jenkins
U.S. Naval Radiological Defense Laboratory
San Francisco 24, California..... 1 copy

Chief, Bureau of Naval Weapons
Navy Department
Attn: CAPT W. L. Jones, MC, USN, RAAE-13
Washington 25, D. C. ..... 1 copy

HQ USAF (AFRDT)
Human Factors Division
Attn: Major A. G. Wise, Jr. USAF
Washington 25, D. C. ..... 1 copy

Chief
Defense Atomic Support Agency
Attn: Document Library
Washington 25, D. C. ..... 3 copies

DASA RETINAL BURN DISTRIBUTION LIST - - 1962 (continuted)

Commander, Field Command
Defense Atomic Support Agency
Sandia Base, Albuquerque, New Mexico..... 1 copy

Chief, Defense Atomic Support Agency
Pentagon
Attn: DASAMD
Washington 25, D. C. ..... 1 copy

Armed Services Technical Information Agency
Arlington Hall Station
Washington 25, D. C. ..... 10 copies

RETINAL BURN AND FLASHBLINDNESS

TECHNICAL DISTRIBUTION LIST

DISTRIBUTION LIST:	COPIES
Commanding General Quartermaster Research and Engineering Command ATTN: Mr. David Feldman Natick, Massachusetts	1
Commanding Officer U. S. Naval Air Development Center Aviation Medical Acceleration Laboratory ATTN: J. H. Hill Johnsville, Pennsylvania	1
Dr. J. Jacobson, M.D. New York Eye & Ear Hospital New York, New York	1
Chief, Bureau of Naval Weapons Department of the Navy ATTN: CAPT W. L. Jones, MC, USN Washington 25, D. C.	1
Wright Air Development Center Wright-Patterson AFB Aerospace Medical Laboratory (ASBLPV) ATTN: Captain L. R. Loper, USAF Dayton, Ohio	1
U. S. Army Ordnance Tank Command. ATTN: ORDMC RRD-3 Centerline, Michigan	1
U. S. Air Force School of Aviation Medicine, SAM Box 2268 Aerospace Medical Center ATTN: Captain A. V. Alder, USAF Brooks AFB, Texas	1

DISTRIBUTION LIST (Continued): COPIES

Dr. William T. Ham, Jr. 1
Department of Biophysics
Medical College of Virginia
P. O. Box 877
Richmond, Virginia

U. S. Naval Material Laboratory 1
New York Naval Shipyard
ATTN: Mr. Willard Derksen
Brooklyn 1, New York

Commanding Officer 1
U. S. Naval Weapons Evaluation Facility
Kirtland Air Force Base
ATTN: LCDR P. E. Beck, USN
Albuquerque, New Mexico

U. S. Army Ordnance Arsenal 1
Frankford, ORD BA-5215
ATTN: P. R. Yoder
Philadelphia 37, Pennsylvania

Armed Services Technical Information Agency 5
Arlington Hall Station
Arlington 12, Virginia

Commander, Field Command. 1
Defense Atomic Support Agency
Sandia Base, Albuquerque, New Mexico

Chief, Defense Atomic Support Agency 2
ATTN: Chief, Document Library Branch
Washington 2

UNCLASSIFIED

Defense Threat Reduction Agency
45045 Aviation Drive
Dulles, VA 20166-7517

CPWC/TRC May 6, 1999

MEMORANDUM FOR DEFENSE TECHNICAL INFORMATION CENTER
ATTN: OCQ/MR WILLIAM BUSH

SUBJECT: DOCUMENT REVIEW

The Defense Threat Reduction Agency's Security Office has reviewed and declassified or assigned a new distribution statement:

- AFSWP-1069, **AD-341090**, STATEMENT A — RD waiting for reply
- DASA-1151, AD-227900, STATEMENT A
- DASA-1355-1, **AD-336443**, STATEMENT A
- DASA-1298, AD-285252, STATEMENT A
- DASA-1290, AD-444208, STATEMENT A
- DASA-1271, AD-276892, STATEMENT A
- DASA-1279, AD-281597, STATEMENT A
- DASA-1237, AD-272653, STATEMENT A
- DASA-1246, AD-279670, STATEMENT A
- DASA-1245, AD-419911, STATEMENT A
- DASA-1242, AD-279671, STATEMENT A
- DASA-1256, AD-280809, STATEMENT A
- DASA-1221, AD-243886, STATEMENT A
- DASA-1390, **AD-340311**, STATEMENT A — FRD
- ~~DASA-1283, AD-717097, STATEMENT A~~ OK
- DASA-1285-5, AD-443589, STATEMENT A
- DASA-1714, AD-473132, STATEMENT A
- DASA-2214, AD-854912, STATEMENT A
- DASA-2627, AD-514934, STATEMENT A
- DASA-2651, AD-514615, STATEMENT A
- ~~DASA-2536, AD-876697, STATEMENT A~~
- DASA-2722T-V3, AD-518506, STATEMENT A
- DNA-3042F, AD-525631, STATEMENT A
- DNA-2821Z-1, AD-522555, STATEMENT A

If you have any questions, please call me at 703-325-1034.

Ardith Jarrett

ARDITH JARRETT
Chief, Technical Resource Center